Hydrophobic Modifications of Cellulose Nanocrystals for Anticorrosion and Polymer Coating Applications

by

Malin Ly

A thesis

presented to the University of Waterloo

in fulfilment of the

thesis requirement for the degree of

Master of Applied Science

in

Chemical Engineering

Waterloo, Ontario, Canada, 2020

Author's Declaration

This thesis consists of materials all of which I authored or co-authored: see Statement of Contributions included in the thesis. This is a true copy of the thesis, including any required final revisions, as accepted by my examiners.

I understand that my thesis may be made electronically available to the public.

Statement of Contributions

Chapter 2 of this thesis is adopted and modified from a literature review that is expected to be submitted for a publication. I co-authored this manuscript with Dr. Ogunsona and Prof. Mekonnen. Dr. Ogunsona and I wrote the majority of the work with Prof. Mekonnen's guidance and supervision. All authors conceived and contributed to this work.

Chapter 3 is a published journal article that I co-authored with Prof. Mekonnen. I developed the experimental procedures, performed the experiment and wrote the manuscript draft. Prof. Mekonnen provided guidance, reviewed, and finalized the paper for publication.

Chapter 4 consist of a paper that is recently submitted for publication. I co-authored this manuscript with Dr. Tesfaalem Haile and Prof. Mekonnen. I performed the synthesis, analytical testing and wrote the draft manuscript. Dr. Haile provided guidance on electrochemical impedance (EIS) and performed the electrochemical test. Dr. Mekonnen provided an overall supervision for the research and reviewed the final version of the manuscript for publication.

Abstract

Cellulose nanocrystal (CNC) is a robust, renewable and green nanorods, which has a potential as an excellent reinforcing and multifunctional filler for polymers used in coating and other applications. CNC contains abundant surface hydroxyl (-OH) groups, making it highly polar and hydrophilic nanomaterial. As a result, its interfacial interaction and dispersibility in several non-polar polymers, such as epoxy and polyurethane, is limited. These limitations severely constrain it from transferring its intrinsic properties (e.g. loading bearing capabilities) to polymeric materials. The main goal of this thesis was to investigate the surface chemical modifications of CNCs with hydrophobic molecules to enhance its compatibility with epoxy and polyurethane matrices for coating applications.

In the first part of the study, ammonium cationic surfactant modified CNC was produced. First, the -OH group of CNC was oxidized to carboxylic CNC using 2,2,6,6-Tetramethyl-1-piperidinyloxy (TEMPO) as a catalyst. Then, three differentiated cationic ammonium surfactants: cetyltetramethylammoniumbromide (CTAB, C16 single chain), dimethyldidodecylammonium bromide (DDAB, C12 double chains), and dimethyldihexadecylammonium (DHAB, C16 double chains) were used to modify the surface of carboxylate CNCs. The modifications were confirmed using Fourier-Transform Infrared Spectroscopy (FTIR) and elemental analysis. X-ray diffraction (XRD) and thermogravimetric analysis (TGA) of the samples revealed that the crystallinities and the thermal stabilities of the modified CNCs were preserved. Corrosion protection studies of epoxy nanocomposite coatings containing the native and surfactant modified CNCs were conducted using model steel specimens via salt spray and electrochemical test methods. The results indicated that the use of surfactant modified CNCs resulted in an enhanced dispersibility in the epoxy matrices as compared to native CNCs. The improved dispersion assisted in retardation of the penetration of

electrolyte that caused a remarkable improvement in the metal corrosion protection performance, as compared to unfilled or native CNC filled epoxy coatings.

The second investigation focused on the modifications of CNCs for polyurethane polymer coating. It involves surface grafting of varying levels of epoxy functionalized silane (ES) on surface of CNCs. The effect of reaction time and concentration of ES on the level of grafting were also investigated. The level of modifications was evaluated using Fourier Transform Infrared Spectroscopy (FTIR), Elemental analysis (EA), X-ray photoelectron spectroscopy (XPS), water contact angle measurement (WCA) and dispersibility test. It was found that prolonged reaction time and high mole ratio of ES to CNC improved the thermal properties and material wettability of the modified CNC. The highest modified sample has WCA of 72.5º as compared to 25.6º for CNCs. The incorporation of modified CNC in polyurethane not only improved mechanical properties but also reduced the water absorption properties of the PU composites, which could be attributed to the improvement in the dispersion and enhanced interfacial adhesion between the nanoparticle and the PU matrix. Salt spray and electrochemical impendence spectroscopy (EIS) study that were carried out on mild steel coated with PU/ES-CNC nanocomposite exhibited excellent corrosion protection against salt solution compared to pure polyurethane.

As a result of these two studies, knowledge of modification of CNC through cationic surfactant and epoxide functionalized silane agent have been advanced. The tailoring of CNC surfaces via a facile and green process that maintained their desired crystallinity and nanostructure while enhancing their compatibility with hydrophobic polymer matrices could further expand their application in several advanced multifunctional material platforms.

Acknowledgements

I would like to express my special thanks to my supervisor, Prof. Tizazu Mekonnen, for his guidance, support and encouragement during my master's program. Thank you for guiding me in doing research and assisting me in finding my career path.

My sincere gratitude also goes to Dr. Emmanuel Ogunsona for all the valuable discussions and encouragement to carry out my research project throughout my master's degree. Thank you for being a good mentor in conducting my experiments and making good diagrams, and more importantly for the full support over the course of this program.

I would also like to thank Ewomazino Ojogbo, Prachiben Panchal, Joanna Jardin and every member of Mekonnen's lab for the friendship and support over the past two years of my master's degree.

I want to deeply thank my close friends: Ronny Dwiputra, Shuxian Lin and Jonathan Wong, for the friendship, love and support. Thank you for reassuring my abilities and making me confident in myself. More importantly, thank you for the memories we created together all these past years.

Finally, my deepest appreciation to my family from Cambodia. Without their emotional support and motivations, I would not be able to complete this challenging journey. I thank my parents for always being there for me and teaching me to be a grateful and moral person I am today.

Table of Contents

List of Figures

List of Tables

List of Abbreviations

CNC	Cellulose nanocrystals
CTAB-oCNC	CTAB modified on oxidized cellulose nanocrystals
DDAB-oCNC	DDAB modified on oxidized cellulose nanocrystals
DHAB-oCNC	DHAB modified on oxidized cellulose nanocrystals
DMA	Dynamic mechanical analysis
DSC	Differential scanning calorimetry
EA	Elemental Analysis
EIS	Electrochemical Impedance
ES	Epoxide functionalized silane
ES-CNC	Epoxide functionalized silane treated cellulose nanocrystals
FTIR	Fourier transform infrared spectroscopy
KBr	Potassium bromide
NMR	Nuclear magnetic resonance
o-CNC	Oxidized CNC
PU	Polyurethane
SEM	Scanning electron microscopy

T_g	Glass transition temperature
TGA	Thermogravimetric analysis
THF	Tetrahydrofuran
TEM	Transmission electron microscopy
WCA	Water contact angle
XRD	X-ray diffraction
XPS	X-ray photoelectron spectroscopy

Chapter 1. Introduction

1.1 Overview

Corrosion of metals has been the past, present and future interest to many industries and researchers. Many industries such as transportation and infrastructures sectors have been suffering from unseen failures associated with metal corrosions. It was estimated that about € 1.3 to 1.4 trillion annually was consumed around the world associated directly with metal corrosion including materials, repairing, maintenance and replacement cost [1]. About 20 to 25% of this cost can be saved by implementing corrosion control technologies [1]. This has led to many attempts to design and develop various technologies to enhance anticorrosion properties of metals. Organic coatings are conventional paint coatings, widely applied to metals to form a physical barrier and protect metal substrates against moisture, harsh environments and corrosive medium. Typical organic coating including epoxy and polyurethane are extensively used in automotive, marine and construction applications. However, the long-term durability of these coatings has been a primary concern due to their susceptibility to scratch and dent, leading to surface defects and hence metal corrosion.

The incorporation of nanomaterials into organic coating have shown promising results in improving both mechanical and barrier properties of epoxy and polyurethane based organic coatings. Nanomaterials such as clay, silicon oxide, carbon nanotubes and zinc oxide nanoparticles are widely used. However, current interest has deviated toward renewable bio-materials due to sustainability, renewable resource utilization, light-weighting benefits, and reduction in environmental impacts.

Nanocellulose are sustainable and renewable nanomaterials isolated through mechanical and chemical processes from wood, cotton linen, tunicates, etc. [2]. These nanomaterials consist of repeating chain unit of β (1→4) D glucopyranose. Nanocellulose have many advantages over other nanoparticles for polymer nanocomposite applications, due to their unique mechanical strength, high crystallinity, low density, high aspect ratio, sustainability and renewability. Two type of nanocellulose draw gained substantial interest: Cellulose Nanocrystals (CNCs) and Cellulose Nanofibrils (CNF). CNCs are needle like nanoparticles and depending on the biomass sources of cellulose, the width and length of nanoparticle can range from 3-5 nm and 50-100 nm, respectively [2,3]. On the other hand, CNFs morphology is network like structures, and they can be obtained from similar biomass sources as CNC [2,4].

CNC has been shown to be more preferential compared to CNF for the fabrication nanocomposite coating due to the homogeneity of nanomaterials, less entanglement and higher crystallinity, which are observed to significantly reduce the diffusion of water and ion to pass through nanocomposite coatings [5].

The direct addition of CNC into non-polar polymer still present a major challenge due to the formation of aggregation associated with the interaction of CNCs hydroxyl -OH groups with each other and the poor interface with non-polar polymers. In order obtain their full benefit, these nanoparticles need to be chemically modified. The two common chemical modifications of CNCs are through adsorption of surfactant and chemical bonding of hydrophobic molecules onto the surface of CNCs. This research mainly focused on the hydrophobic chemical modification of CNC and the incorporation of those modified CNC into two different polymers, epoxy and polyurethane, for coating applications with a goal of improve the corrosion protection and multifunctional properties of the polymer coatings.

1.2 Objectives and motivation

The objective of this investigation is to develop epoxy and polyurethane nanocomposites coatings containing hydrophobic cellulose nanocrystals for anticorrosion and advanced functional applications. Two distinguished chemical modification pathways for CNC was carried out specifically for epoxy and polyurethane nanocomposite coatings. These two different pathways in this thesis are listed as following.

(i) Cationic surfactant modification of cellulose nanocrystals for corrosion protective epoxy nanocomposite surface coatings.

- The first step was to modify CNC using three different cationic ammonium surfactants. This was done by oxidizing CNC to form carboxylic CNC followed by deprotonation to produce negatively charged carboxylate CNCs, which can interact with the cationic ammonium group of surfactants to form hydrophobic CNC. The level and impact of the modifications were evaluated using various analytical techniques.
- The next step was to incorporate the cationic surfactant modified CNCs into epoxy polymer to form nanocomposite coating. The morphological behavior such as the dispersibility of the modified CNC in epoxy matrices was evaluated.
- Finally, the epoxy nanocomposites containing surfactant modified CNC was evaluated for their anticorrosion properties using salt spray test and electrochemistry.

(ii) Hydrophobic functionalization of cellulose nanocrystals for enhanced corrosion resistance of polyurethane nanocomposite coatings.

- The first step was to synthesize hydrophobic CNC through sol gel reaction (silanization) of epoxide functionalized silane with CNC. It was important to determine optimal ratio of silane to CNC to form the highest hydrophobic CNC. The properties of modified samples were evaluated using various analytical characterizing techniques.
- The next step was incorporating the highest hydrophobic modified CNCs from the previous step into polyurethane formulation to form nanocomposite coatings. Various nanocomposites containing different weight percentage of modified CNC were examined for their morphology, thermo-mechanical and water absorption properties.
- Finally, the PU/modified CNC nanocomposites were applied on to steel metal and the corrosion protection was evaluated using salt spray and electrochemical impedance (EIS) tests.

A summarized pathway of the investigation is illustrated in **Figure 1.1**

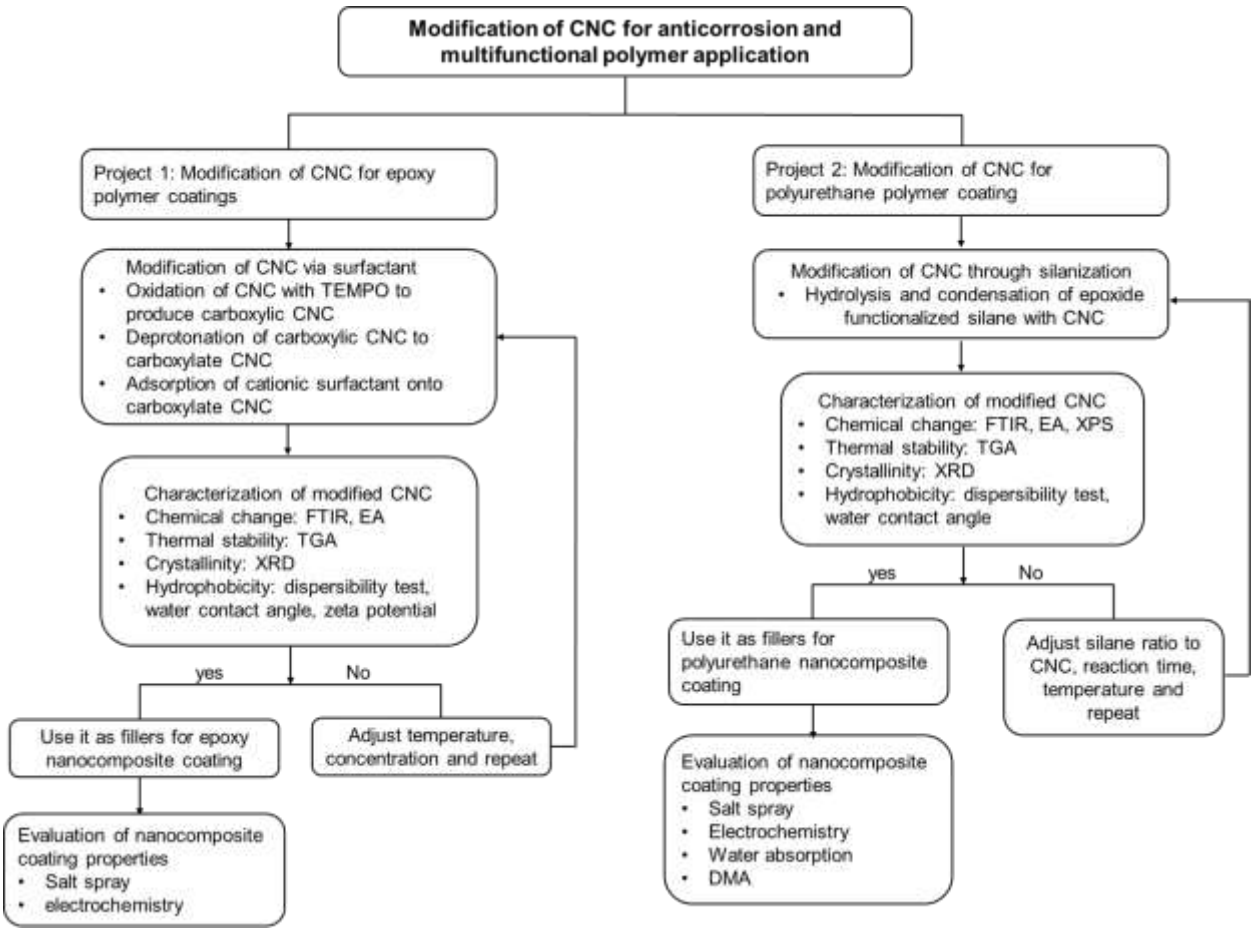

Figure 1.1. Research pathway of CNC modification for polymer nanocomposite coatings.

1.3 Thesis outline

This thesis is composed of 5 chapters. The scope of these chapters is listed as follows:

- Chapter 1 briefly introduces the significance of CNC as a filler and functional additive of nanocomposites for anticorrosion and functionalized applications. It also defines the research objective and the overall study pathway.
- Chapter 2 provides literature review of superhydrophobic/hydrophobic coatings. It narrows down to the motivation behind the objective of this research, utilizing bio-based nanomaterials such as CNC, to enhance the barrier properties of polymer coatings.

- Chapter 3 presents the surface modification of CNC via cationic surfactants and the effect of the modified CNCs in epoxy coatings against corrosion in metallic surfaces.
- Chapter 4 reports the modification of CNC with epoxide functionalized silane and its incorporation in polyurethane polymer coating formulations.
- Chapter 5 provides the overall summary, conclusion and recommendations for any future work.

Chapter 2. Literature review

2.1 Introduction

Many industrial applications in today's world are based on hydrophobic surface technologies with superhydrophobic materials becoming of increasing interest. One notable observation of superhydrophobic surfaces is that water droplets easily roll off as soon as they come in contact with these surfaces. These water droplets typically carry along any contaminant from the material surface. This characteristic is described as "self-cleaning" property of superhydrophobic materials[6]. Aside from this, superhydrophobic materials also exhibit additional properties such as anti-fouling, anti-fogging, anti-icing and anti-corrosion[7,8]. Many industrial applications and products are based on these superhydrophobic properties, with a few examples such as stain-resistant and waterproof textiles, self-cleaning windshields and windows and anti-corrosive paints[6,9,10]. In addition to these, superhydrophobicity is also commonly used in preventing metal surface corrosion when exposed to corrosive environments[11].

The development of superhydrophobic surfaces is bioinspired from water repellency which has been observed in nature. Lotus plant (Nelumbo nucifera Gaertn) is able to maintain a clean leaf surface despite growing in swamps and shallow waters where dust and other micro-sized debris can easily settle on its leaves[12]. The nano-sized hierarchical structures covering the micro-scale papillae are responsible for the water repellent and high water contact angle (WCA) of greater than 150^{o}[13]. The phenomenon, specific to the lotus leaf is generally termed the "lotus effect" and is now used to describe superhydrophobic surfaces that are water repellent and self-cleaning[13].

Material wettability is commonly characterized using water contact angle (WCA), which is a measure of the angle between a water droplet in contact with a solid surface[6,14]. To be considered a superhydrophobic material, the WCA of a surface should exceed 150^o[14]. Lotus leaves are one of the well-known water repellent surfaces with a WCA of $161^o \pm 2.7^o$. Another biological non-wetting surface is that of water strider legs, which allow them to slide effortlessly on water. The typical WCA of a water strider's leg was found to be $167.6^o \pm 4.4^o$[15].

The discovery of the mechanisms behind the "lotus effect" inspired many engineers and scientists to mimic the superhydrophobicity found in nature and engineer superhydrophobic synthetic surfaces. The surface roughness and chemistry significantly affect the superhydrophobic state of materials[11]. A variety of techniques have been developed and used to impart surface roughness onto materials including etching, lithography, electrodeposition, sol-gel solution, electrospinning, self-assembly and layer by layer methods[11,16]. Synthetic polymers such as PDMS (polydimethylsiloxane), polytetrafluoroethylene (PTFE, a.k.a. Teflon), LDPE (low-density polyethylene) are commonly used to prepare superhydrophobic surfaces with high WCA[16].

For the past couple of decades, extensive research into and use of non-renewable materials including minerals such as zinc oxide (ZnO), titanium oxide (TiO_2), silicon oxide (SiO_2) as well as synthetic polymers (PTFE, LDPE, etc) to prepare superhydrophobic materials have been mostly focused on[11]. As of late, however, some of these materials have been deemed environmentally unfriendly with concerns stemming from their non-sustainability, physical property such as high density and negative effects to the immediate environment. Likewise, regulations requiring the use of more sustainable and bioderived materials with little to no negative impact on the environment have driven the research and development of alternative designs with the utilization of more environmentally-friendly and bio-based materials such as nanocellulose, lignin and

heteropolysaccharides for superhydrophobic surfaces[11]. The advantages and interest in using these materials are that they are biodegradable, sustainable, low-cost, low-density, abundant in nature, have good surface chemistry reactivity and easily amenable to modifications, and high thermal and mechanical properties[11,17,18].

An introduction to the fundamental concepts of wettability and the bioinspired superhydrophobicity from nature is briefly discussed to as a steppingstone to the advances in the development of synthetically engineered superhydrophobic surfaces. Further, the engineering strategies employed to create superhydrophobic surface coatings including methods for surface roughness as well as the low surface energy materials are discussed. Importantly, a focus on the progress in superhydrophobic surfaces in the last decade with respect to simplistic, low-cost and efficient techniques are discussed. Finally, the application of biobased, sustainable and environmentally friendly materials such as nanocellulose-based materials and their applications toward superhydrophobic surfaces are reviewed. Though, there have been some review publications on superhydrophobic surfaces, this review sheds light on the recent advances employed to mitigate the demerits of fabrication techniques and materials used in the development of superhydrophobic surfaces such as high-cost, multi-step processes and nonenvironmentally friendly materials.

2.2 Fundamentals of materials wettability

2.2.1 Young's equation

The wettability of surface materials is basically determined based on water contact angle (WCA), which is the measured angle of a liquid droplet on a sample solid surface[6,14,19]. The measurement of the WCA is primarily based on Young's equation, which was developed in 1805 by Thomas Young [19] and can be determined using Equation 1

$$cos\,\emptyset_o = \frac{\Upsilon_{SV} - \Upsilon_{SL}}{\Upsilon_{LV}} \qquad (1)$$

where $\emptyset_o$ is the Young contact angle and γ_{SV}, γ_{SL}, γ_{LV} are the interfacial surface tension of solid-vapour, solid-liquid, and liquid-vapour interface at equilibrium, respectively[10,19].

Through Young's equation, the highest WCA is obtained when the value of γ_{SV} is the lowest, which corresponds to any material with the lowest measured surface energy[11]. The nature of the elemental composition of the chemicals formed on the material surfaces as well as their distribution affect the material's wettability. In general, close packing molecules have low surface energy and the tendency for lower surface energy which can be determined based on the following hydrophobic molecule order: -CH_2- > -CH_3- > -CF_2- > -CF_2H- > -CF_3-[20]. Application of these molecules has been successfully executed by Nishino et al., where surfaces with a low energy of around 6.7 mJm^{-2} from the hexagonal pack of -CF_3[21].

2.2.2 Wenzel and Cassie-Baxter models

The evaluation of wettability using Young's equation is ideal for specific surface parameters such as topology, homogeneity and chemically inertness with the probing liquid[20]. Realistically, the majority of material surfaces are neither smooth, flat, nor made up of chemically homogeneous elements[11]. The determination of WCA via Young's equation is oversimplified and no longer accurate in many conditions and, given this, more comprehensive models for WCA have to be considered for rough and non-heterogeneity surfaces[20]. Two different models, Wenzel and Cassie-Baxter models were adapted from Young's equation to characterize the WCA of rough solid surfaces.

Wenzel model for wettability was developed by Wenzel in 1936[22]. In this model, assumptions in the uniformity of droplet penetration into the grooves of rough solid surfaces, as

shown in **Figure 2.1a,** and the wetting regions are made[23]. Therefore, the WCA can be measured using Equation 2

$$cos\,\emptyset_w = R_f\,cos\,\emptyset_o \qquad (2)$$

where $\emptyset_W$, $\emptyset_o$, R_f are Wenzel's WCA of rough solid surfaces, the WCA of Young's equation and roughness factor of the surfaces, respectively[22,24]. Wenzel model is suitable for determining the WCA when the surface can be filled by the probing liquid[20]. However, this is not always the case for all surface roughness.

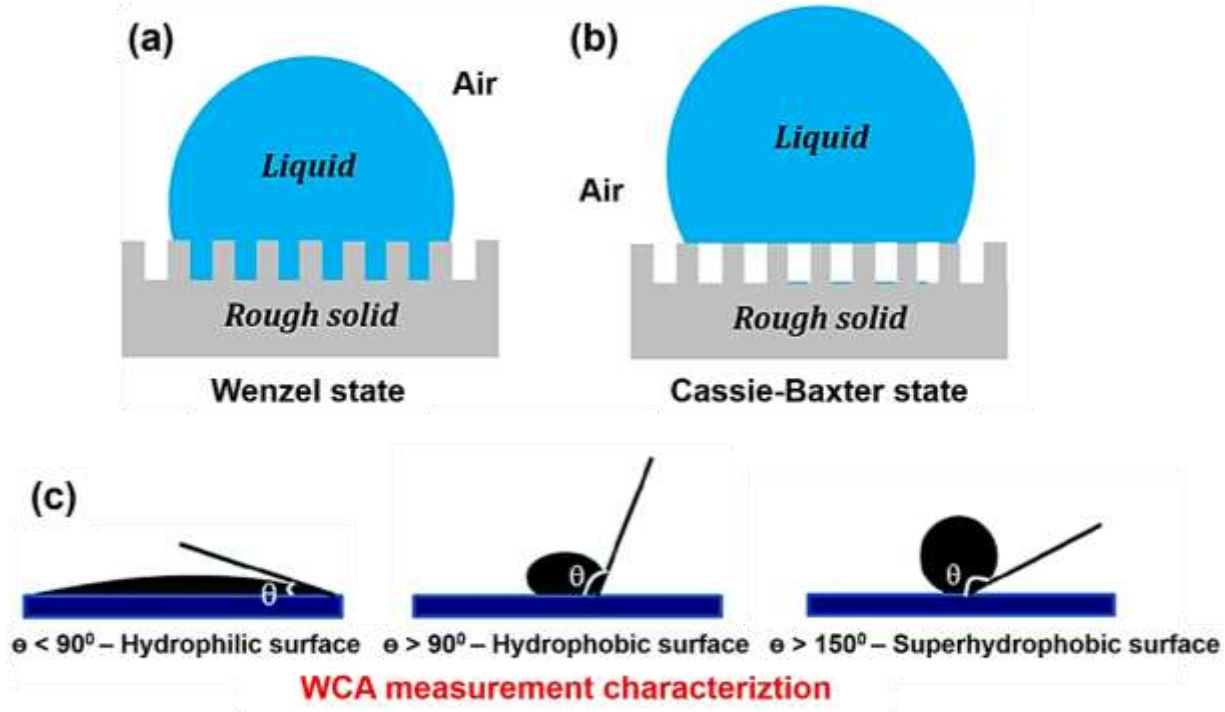

Figure 2.1. The comparison of water droplet interaction with rough surfaces through (a) Wenzel model and (b) Cassie-Baxter model of superhydrophobicity [24] and (c) schematic illustration of wettability characterization from WCA measurement [16].

In the Cassie-Baxter model (**Figure 2.1b**), droplet penetration into the rough solid surface is limited due to small protrusions on the material surfaces. Instead, air pockets are usually formed between the droplets and surfaces, allowing stay suspended on top of the air grooves[20]. This is

referred to as “heterogeneous wetting” and the WCA based on this model is calculated from Equation 3

$$cos\,\emptyset_{CB} = f_s\,(cos\emptyset_o + 1) - 1 \qquad (3)$$

where $\emptyset_{CB}$, $\emptyset_c$, f_s are the Cassie-Baxter WCA, WCA of smooth surface from Young’s equation, and fraction area of solid in contact with probing liquid, respectively[20,23].

2.2.3 Contact angle hysteresis

According to Young’s equation, there is only one possible WCA, where the droplet resides on the smooth surface. However, this is completely erroneous and does not apply in cases involving surface roughness and chemically heterogeneous surfaces, as the droplet can form a wide range of stable angles with such surfaces[25]. Contact angle hysteresis (CAH) is the difference in contact angle between an advancing liquid ($\emptyset_{adv}$) and a receding liquid ($\emptyset_{rec}$), and is usually the result from surface roughness and heterogeneity[19,26]. In other words, CAH is the difference in droplet angles when surface of material is tilted at specific angles. Smaller CAH is observed in smoother and more homogenous surfaces, which could be due to weak adhesion of solid to liquid phase while larger CAH usually observed for rough surfaces as the liquid droplet tends to adhere more to the surface[19,24]. CAH is considered a critical parameter to determine adhesion, wettability and energy dissipation of flowing droplet[24].

2.2.4 Classifications of wettability

Material wettability and superhydrophobicity are characterized using water contact angle of droplets on material surfaces. These can be categorized under three surfaces types: hydrophilic, hydrophobic, and superhydrophobic (or ultra-hydrophobic) as demonstrated in **Figure 2.1c** When the WCA is less than 90^o, the droplet has a good interaction with material surface and this surface

is considered hydrophilic. Hydrophobic surfaces are defined by their contact angle value between 90^o and 150^o while superhydrophobic surfaces normally exhibit a WCA of $>150^o$[14]. Sliding angle (SA), which is the measured angle where a droplet contacts a tilted surface is another common parameter commonly reported along with WCA[27]. With superhydrophobic surfaces, water droplets form a very small SA with the surface and allow the droplet to roll off the surface of materials effortlessly[6,10]. Lotus leaves and water strider legs are examples bio-structured superhydrophobic materials, exhibiting a WCA greater than 150^o and SA less than 5^o [10,15].

2.3 What can we learn from nature?

Many technologies and products in modern-day life are inspired by the observations and investigations of mother nature. The "lotus effect" and superhydrophobicity are interchangeably used terms, was discovered thousand years ago; however, the explanations behind this remarkable phenomenon was not explained until the mid-1960s. The invention of the high-resolution scanning electron microscope (SEM) was an incredible technology that revealed the science and mechanism behind the superhydrophobicity of lotus and other superhydrophobic surfaces occurring in nature[12]. Two specific superhydrophobic materials in nature, sacred lotus leaf and water stride legs, will be discussed in terms of their topography and mechanisms behind their superhydrophobicity.

In many cultures, lotus leaf is a representation of purity, and this is due to the fact that the leaf maintains cleanliness through its self-cleaning capability[28]. This observation has led to the investigations to determine the topographical structures and compositions behind this property. The epicuticular wax is found on the lotus leaf and has a low surface energy due to its chemical composition; however, the WCA study of this wax revealed the angle of only 110^o, which is not a

sufficient explanation of the superhydrophobicity behind the lotus leaves[10]. **Figure 2.2a** shows a water droplet on the surface of a lotus leaf and **Figure 2.2b and 2c** are the topographic images from the SEM analysis of a lotus leaf at different magnifications. Two different roughnesses are observed on the lotus leaf: hierarchical microstructure (around 10μm) and nanostructure (about 100 nm)[10]. The superhydrophobicity comes from the combination of hydrophobic epicuticular wax and the surface roughness from the micro-nano structures[10,29]. The presence of the wax coating on the rough surface allows for the entrapment of air pockets at the water droplet-solid surface interface, resulting to a very high WCA and small SA of 161 ± 2.7^{o} and less than 5^{o}, respectively[10,29].

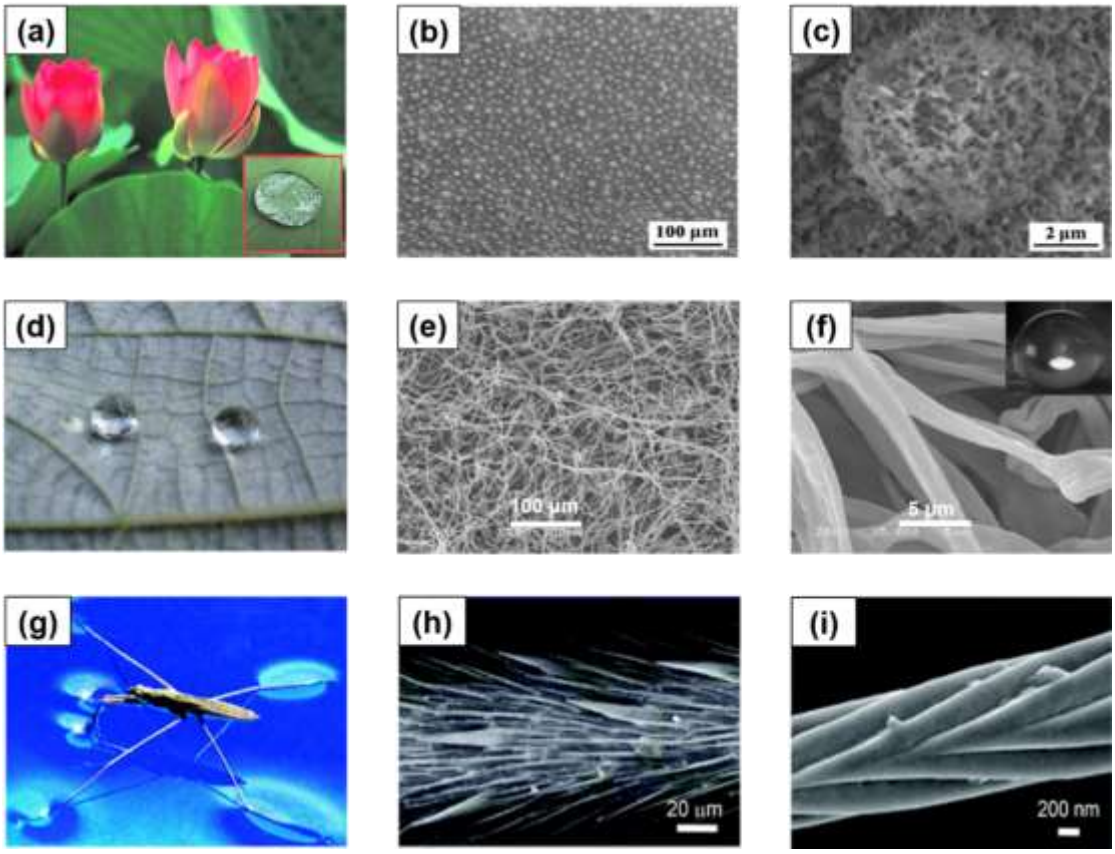

Figure 2.2. (a) photograph of lotus leaf with a water droplet on surface (insert), (b and c) low and high-resolution SEM images of lotus leaf surface, respectively measurement [30], (d-f) photograph of water droplet formed on rear face of ramee leaf, low and high-resolution SEM images, respectively. (The inset in (f) is the WCA of ramee leaf (rear face)) [31], (g) photograph

of a water strider suspended on the water surface without piercing the water surface, (h and i) low and high magnification SEM images of water strider leg structure, respectively [32].

Many other plant leaves have similar topographic structures to that of the lotus leaf such as rice leaf, taro leaf, Indian canna leaf, purple setcreasea leaf, and plant leaves of perfoliate knotweed with WCA of 157 ± 2^o, 159 ± 2^o, 165 ± 2^o, 167 ± 2^o (frontal face) and 162 ± 2^o (frontal face), respectively[31]. Aside from hierarchical structures on plant leaf surfaces of, the unitary structures are also observed to repel water using similar a mechanism to that of the lotus leaf. Ramee leaf is an example of a surface with a unitary structure. It is interesting to note that the frontal face of a ramee leaf is not superhydrophobic with a WCA only around 38 ± 2^o. However, the rear face of the ramee leaf is superhydrophobic **Figure 2.2d)** with a WCA of 164 ± 2 ^{o}. **Figure 2.2e and 2.2f** show the rear face morphology of ramee leaf using SEM analysis. It can be seen that the surface of the leaf is covered with the unitary distribution of fiber-like structures with a diameter of about 1-2 μm[16,31]. Chinese watermelon also exhibits fiber-like unitary distribution similar to ramee leaf with WCA of 159 ± 2 ^{o}. In addition to the hierarchal structure found in the majority of plant leaves, the unitary structures also contribute to the superhydrophobicity found in nature[31].

Plant leaves are not the only nature-made superhydrophobic material. Water strider also show water repellent properties and the ability to slide across water surfaces without breaking the surface with the creation of a "dimple effect" and dimple depth of up to 4.38 ± 0.02 mm[15] (**Figure 2.2g**) while **Figure 2.2h** shows the surface structure of water strider's leg, revealing needle-like microstructure, aligned inclined at an angle of 20^o. On each needle-like microstructure, nanoscale grooves are observed **(Figure 2.2i)**, which are responsible for creating air pockets at the water/leg surface interface[15,32] in conjunction with a wax coating[32]. The superhydrophobicity

of material surfaces is ascribed mainly to two phenomena: (1) materials with low surface energy and (2) micro and nano structure such as roughness of the surfaces.

2.4 Engineering superhydrophobic coatings

Bioinspired superhydrophobic surfaces such as plant leaves and water strider legs are mainly dependent on the microstructural roughness and low energy material composition forming the superhydrophobic surface. Engineering of artificial superhydrophobic surfaces will require the utilization of low surface energy materials and the development of fabrication techniques and methods to produce micro and nano structural roughness.

2.4.1 Low surface energy materials

2.4.1.1 Fluorinated molecules

Fluorinated molecules are commonly used in the application of superhydrophobicity. Fluorinated molecules are typically polymer chains containing mainly fluorine and carbon elements. Poly-tetrafluoroethylene (PTFE, aka Teflon films) was the first fluoropolymer invented in 1938. The invention of PTFE opened the door to further opportunities for intense research in developing high performing fluorinated polymers. Strong carbon-carbon bonds, carbon-fluorine bonds, high electronegativity and low polarizability of fluorine elements are responsible for the impressive intrinsic properties of fluorinated materials such as high thermal stability, good chemical resistance, high resistance to mechanical friction and most importantly lower surface energy[33]. However, there is a limitation to utilizing fluoropolymers as they are large compounds and tend to have low solubility, which makes them unideal for processing in many superhydrophobic applications. Generally, fluorinated carbons are used by linking or blending the chains with other materials for superhydrophobic coatings[34].

Lee et al. was able to create superhydrophobic/translucent superamphiphobic coating on steel by spraying silica-fluoropolymer hybrid nanoparticles (SFNs) without any post-treatment step[35]. The nanoparticles provided the micro/nano-structure roughness while the fluoropolymer lowered the surface energy of the coating. Interestingly, the increase in SFNs sol spray concentration caused the conversion from a superhydrophobic to superamphobic state. Similarly, Lin et al. used a two-step dip-coating process to prepare a superhydrophobic and superoleophobic cotton fabrics with modified SiO_2 and fluoropolymer[36]. First, the cotton fabric was immersed in DDS-SiO_2 (commercial hydrophobic fumed silica after treatment with dimethyldichlorosilane), and then dipped into a solution containing 10 % of fluoropolymers. The treated cotton fabrics were shown to have low water and oil absorption, good self-cleaning properties and good laundering durability.

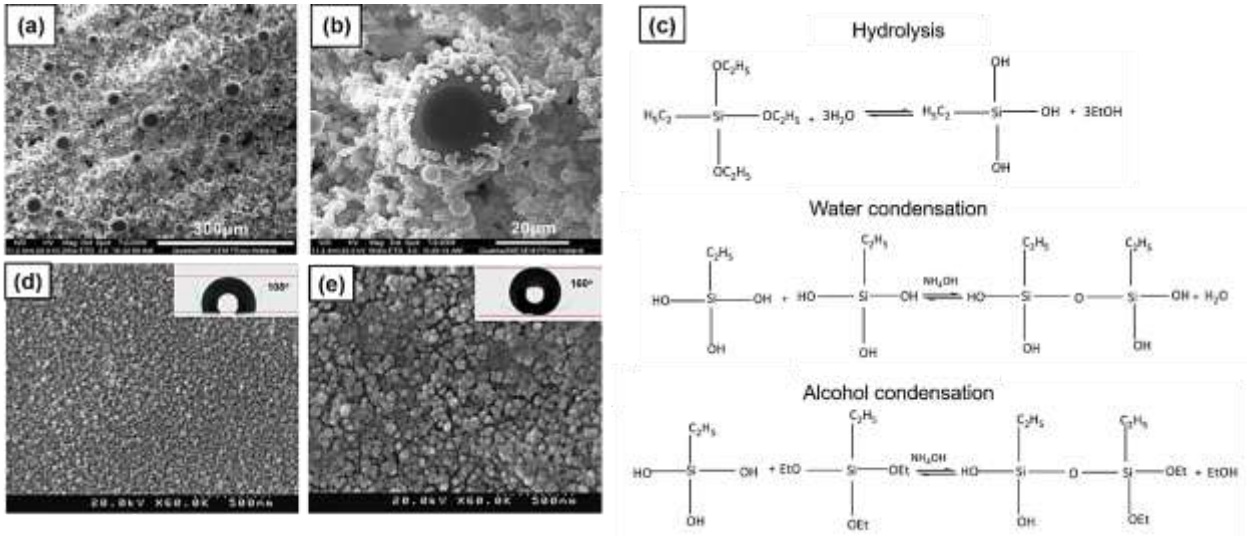

Figure 2.3. Micrographs of copolymer films from silica and fluoropolymers at (a) low and (b) high magnifications[37], (c) reaction mechanisms of formation of Si-O-Si network using ETES precursors, (d and e) micrographs of unmodified and 15% iso-OTMS treated silica films, respectively (Inserts in (d and e) are their WCA) [38] .

Wei et al. prepared a copolymer of styrene and 2,2,3,4,4,4-hexafluorobutyl methacrylate (HFMA) using bulk polymerization. Thereafter, they were able to obtain superhydrophobic films

utilizing phase separation method[37]. The surface morphology of the films was studied using an environmental scanning electron microscope (ESEM) and was revealed to exhibit binary hierarchical structures (**Figure 2.3a and 2.3b)**, which is similar to the topography of lotus leaf. HFMA is a fluorine-containing monomer and is used to lower surface energies. The combination of HFMA with the engineered surface roughness through phase separation led to a high WCA of 154.3^{o} and SA of 5.8^{o}. Chemical grafting of substrate surfaces with fluoropolymers can also be used to improve the superhydrophobicity as well as for better controlling the structure and density of the polymers on the substrate surfaces.

For example, Yuan et al. prepared superhydrophobic copper coating by surface initiated free radical polymerization of fluoropolymer film[39]. First, the copper plate was etched and treated with vinyl-terminated trimethoxysilane to impart the vinyl functional groups. Fluoromonomers, 2,2,3,4,4,4-hexafluorobutyl acrylate (HFBA) were reacted with the vinyl groups through graft polymerization to form the fluoropolymer coating on the copper substrates. The superhydrophobic coating was shown to exhibit a WCA greater than 150^{o} with an improvement in anticorrosion in 3.5% NaCl aqueous solution.

2.4.1.2 Silicones

Silicones are an attractive class of low surface energy substances commonly found in anticorrosion, antifouling, flame retarding, self-cleaning and anti-icing applications[40,41]. Silicones are compounds containing silicon and oxygen alternating in repeating blocks called siloxane. Polydimethylsiloxane (PDMS) was one of the first materials discovery of silicone. The particular Si-O and C-O bonds, in addition to higher bond dissociation energy, provide incredible physiochemical properties of PDMS [40]. Roughening the low surface energy PDMS surface

would lead to constructing micro/nano-structures and hence superhydrophobic properties[41]. Another silicone compound is silica nanoparticles, which can be deposited followed by modification with low surface tension energy materials like silane reagents, leading to material surfaces with superhydrophobic properties[41].

Ramezeni et al. utilized the sol-gel method to prepare superhydrophobic silica film on glass substrates via two-step dip coating[38]. Ethyltriethoxysilane (ETES) was first used as a precursor to form silica film on glass substrate through typical sol-gel reactions involving hydrolysis, water and alcohol condensation as shown in **Figure 2.3c**. Then, this silica film-coated glasses were dipped coating with solution of isooctyltrimethoxysilane (iso-OTMS) as a hydrophobic modifying agent. The morphology of unmodified compared to modified film was revealed from field emission scanning electron microscope (FE-SEM) as shown in **Figure 2.3d and 2.3e**. The silica nanoparticles modified with iso-OTMS are observed to increase its size from 26 nm to 42 nm due to condensation effect of the alkyl chain of iso-OTMS onto the surface of silica particles and this form like outer shell surrounding silica nanoparticles. The WCA of silica films was observed to increase from 108^{o} to 160^{o} in modified samples which due to the hydrophobic C_8H_{17} chains of the iso-OTMS agents. Similarly, Jia and et al. prepared high-water resistance superhydrophobic wood by depositing vinyltriethoxysilane (VTES) treated silica nanoparticles on surfaces. The superhydrophobic wood has a WCA of 154^{o} with close to 0^{o} of SA. In addition to superhydrophobicity, the treated wood had demonstrated to have robust wear resistance, and long-term stability even under an extreme condition like boiling water[42].

2.4.1.3 Organic Materials

Traditionally, organic materials such as polyethylene, polystyrene, polyamide, polycarbonate, and alkylketene dimer have been used to prepare superhydrophobic surfaces[34]. In recent years, there has been so much interest in the use of graphene, carbon nanotubes (CNTs), carbon nanofibers (CNFs) to initiate surface roughness and introduce mechanical strength to superhydrophobic coating. For example, Yang et al. prepared anti-corrosion and self-cleaning epoxy coating on copper substrates through the incorporation of fluorographene (FG) nanosheets. First, the copper was coated with the epoxy layer through dip coating and then FG powders were dispersed on epoxy layers and pressurized to increase the adhesion of FG nanosheets on epoxy surfaces.

Figure 2.4 (a-c) show and compare the epoxy coating, graphene oxide coated epoxy (GOc) and FG coated epoxy (FGc), respectively. The presence of GOc increased the microstructure roughness, leading to a WCA increase from 82^{o} of epoxy coating to 116^{o}. On the other hand, the epoxy coating containing FG were shown to possess micro-nano structures on the surface with different sizes and shapes as shown in **Figure 2.4c**. This increased the surface roughness even further and the WCA of the coating was improved to 154^{o}[43].

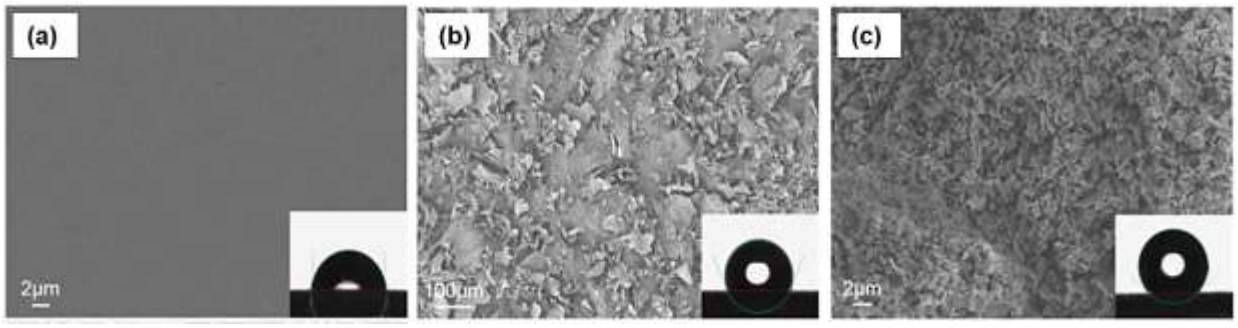

Figure 2.4. FE-SEM images of (a) epoxy coating (b) epoxy coating with GOc and (c) epoxy with FGc (Adapted from Yang et al.[43] with permission from Elsevier copyright © 2017).

Nicola et al. grew multiwall carbon nanotubes (MWCNTs) from the surface of stainless steel via chemical vapour deposition (CVD) for superhydrophobicity[44]. The reaction was initiated at a temperature below 1000^{o}C without the need for a catalyst. The topographies of MWCNTs grown on stainless steel. MWCNTs were uniformly grown and randomly distributed on the stainless-steel surfaces with an average tube diameter of 58.19 ± 18.35 nm. The growth of MWCNTs on the surface increased the WCA to 154^{o}. The water repellency of MWCNTs on the stainless steel could be explained using the Salvinia effect. The tip of MWCNTs are capped with carbonaceous nanostructures that are able to attract water; however, the repulsive interaction of hydrophobic MWCNT is responsible for trapping large amounts of air in air pockets and stabilize the water droplet and hence making it superhydrophobic.

2.4.1.4 Inorganic materials

Inorganic materials have made their way towards use as nanostructured materials in the creation of rough surface for superhydrophobic coatings on substrates. Ebert and Bhushan prepared transparent superhydrophobic glass and various polymer substrate with surface functionalized silicon oxide (SiO_2), zinc oxide (ZnO) and indium tin oxide (ITO)[45]. The hydrophobic modified SiO_2, ZnO and ITO were dispersed in 40%-60% of tetrahydrofuran-isopropyl alcohol (THF-IPA) solvent and substrates were then dipped coated in the solvent mixture. **Figure 2.5a-2.5c** show the SEM images of SiO_2, ZnO and ITO coated on the surface of the glass, respectively. All three nanoparticles formed a network of islands. However, SiO_2 and ZnO nanoparticles covered the glass surface more in comparison to ITO nanoparticle coating. As a result, the WCA of ITO coated glass was the lowest compared to SiO_2 and ZnO coating, which again could be from the unevenly distributed microscale islands and reduced surface roughness (fewer height variations).

Aluminum oxide (Al_2O_3) has also been used to prepare the superhydrophobic coating, and this has been studied by Nishimoto et al[46] They coated the hydrophobic octadecyltrimethoxysilane self-assembled monolayer (ODS SAM) of Al_2O_3 on hydrophilic TiO_2 film. The surface morphology was studied by an optical microscope and AFM, and are shown in **Figure 2.5d**. Al_2O_3 nanoparticles formed amorphous structures on the TiO_2 film with a thickness of about 100 nm, enough to create the surface roughness on the TiO_2 film required for superhydrophobicity. The effect of UV radiation on the film was also studied and was shown that the ODS SAM Al_2O_3 coated TiO_2 was able to maintain high WCA of greater than 162^o, while the ODS modified TiO_2 had its WCA close to 0^o after UV radiation. The excellent resistance to UV radiation comes from the fact that ODS SAM was preserved on photo-catalytically inert Al_2O_3[46]. Inorganic salts have also appeared in a few studies in the field of superhydrophobicity.

Lu et al. immersed mild steel in copper chloride solution followed by chemical treatment with 1H,1H,2H,2H-perfluorooctyltriethoxysilane (FAS)[47]. The surface morphology changed from a smooth texture for untreated mild steel to more textured for $CuCl_2$ treated mild steel. Combining the surface texture with a low surface energy of FAS, they were able to obtain WCA of above 150^o.

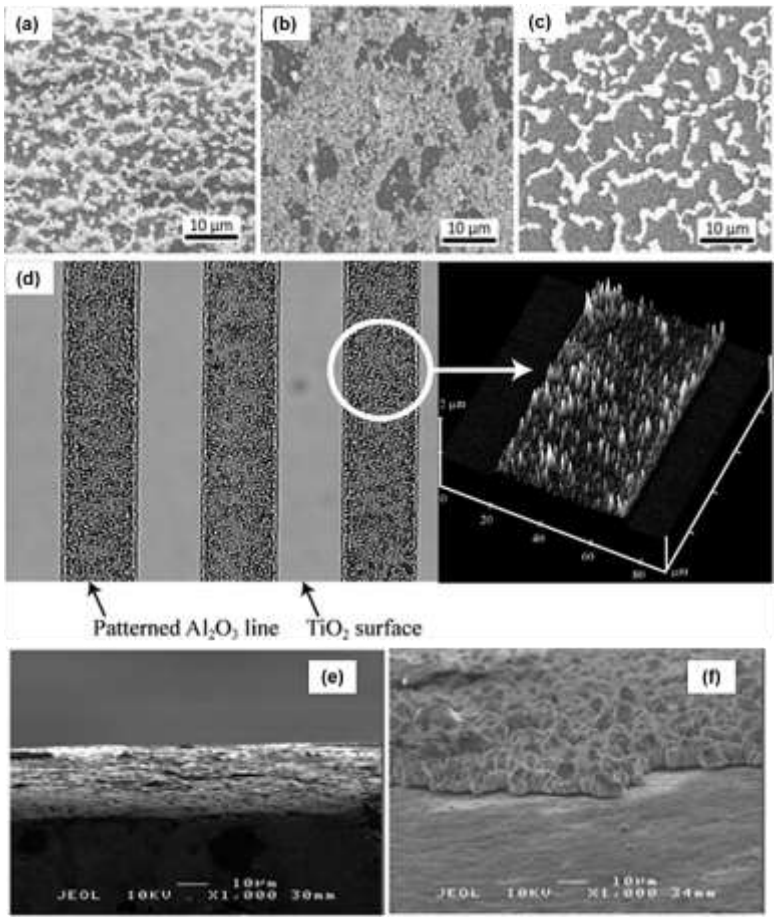

Figure 2.5. SEM micrographs of (a) SiO_2, (b) ZnO and (c) ITO coated on glass substrate [45], (d) optical microscope photograph (left) and AFM images of the topographical measurement (right) of patterned Al_2O_3 coated on TiO_2 films study [46], (e, f) side views micrographs of mild steel before and after immersion in $CuCl_2$ solution, respectively [47].

Similar treatment was prepared on mild steel mesh and the mesh was used to separate oil from a mixture of oil and water through gravity induction. This gravity-induced oil-water separation has demonstrated excellent efficiency of oil collection up to 96%. Similarly, Choi et al. prepared a PDMS superhydrophobic surface using sodium chloride to assist in creating the hierarchical structures on the PDMS surface, and the roughness was observed to improve compared to untreated PDMS[48]. The WCA of inorganic salt treated PDMS film was determined to be 151^o with a SA of 6^o.

2.4.2 Formation of surface roughness

2.4.2.1 Etching treatments

Etching is one of the simplest approaches to create surface roughness for superhydrophobicity. Different strategies of etching including physical etching, chemical etching, plasma etching and ion etching have been developed[34]. Chemical etching refers to a method, which uses chemical etchant to remove layers from the surfaces of materials to create roughness. The concept of chemical etching, which was developed about a half-century ago, was thought to relate to the dissolution of dislocation defects on crystalline metal surfaces. The surface of metal contains large numbers of dislocation defects, which effortlessly allows the chemical etchants to attack and destroy these defects first and result in surface roughness[49]. This was predominantly used due to the low-cost, simplicity of process, controllable etching rate, and scalability[50]. Chemical etching alone cannot produce a superhydrophobic surface. Typically, the metals are etched first, and then hydrophobic low surface energy materials used to modify the rough surfaces.

Rezayi and Entezari demonstrated the effect of chemical etching in their work preparing durable superhydrophobic aluminium surfaces with ZnO nanoparticle deposition[51]. The aluminum plate, which had been etched by immersing in hydrochloric (HCl) solution before ZnO nanoparticle deposition on the surface and followed by stearic acid modification, showed a drastic increase in WCA. Likewise, improved long term stability in 3.5% NaCl solution was observed (**Figure 2.6a, bottom**) compared to samples without prior etching process (**Figure 2.6a, top**). This can be explained by the formation of hierarchical structures on the surface from the etching process, that allowed a large amount of trapped air between the grooves. This prevented the corrosive molecules from coming in contact with the metal surface.

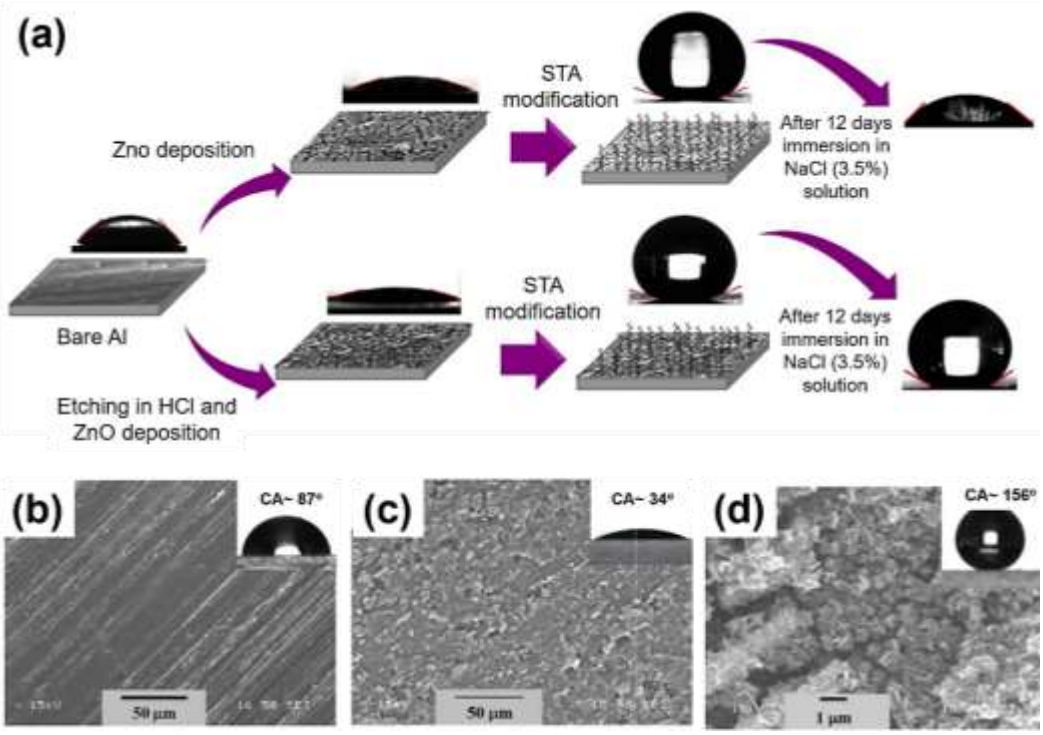

Figure 2.6. (a) The effect of HCl etching on WCA and the demonstration of long term stability of water droplet on coatings after 12 days of immersion in NaCl solution [51], SEM images of aluminium alloy (b) before NaOH etching (c) after NaOH etching and (d) NaOH etching followed by the chemical passivation with SA solution [52].

Similarly, Huang et al. studied the etching of aluminium alloy substrate with NaOH followed by submersing the etched plate into ethanolic stearic acid (SA) solution. **Figure 2.6(b-d)** show SEM micrographs of the aluminium surface before and after etching, and etching followed by chemical modification, respectively. The morphological analysis indicated that the etching process created more roughness on the surface of aluminium (**Figure 2.6c**), but the WCA was decreased from 87 ^{o} to 34^{o} due to the increase in the surface area and the possibility of compositional changes on the surface of the aluminium. The post-treatment with SA combined with increased surface roughness from the etching process created the flake-like micro/nano-structures, resulting in a very high WCA of 156 ^{o} (**Figure 2.6d)**[52].

In recent years, plasma etching treatment has been increasingly used. In a study by Tri et al., the plasma treatments were performed on cotton fibers prior to dip coating with silica nanoparticles and tetraethyl orthosilicate (TEOS). The results showed a very high WCA of 173^{o}, which was attributed to the homogenous roughness created by plasma pre-treatment and ultrafine silica that formed air pocket and repelled the water droplets[53].

2.4.2.2 Electrodeposition

Electrodeposition is a strategy where layers of materials are deposited on the surface of substrates such as polymers and metals from a chemical species in an electrolyte medium to improve wear resistance and corrosion resistance [54]. This technique is considered a simple method to create the surface roughness for superhydrophobic materials due to cost efficiency, scalability and ability to deposit many types of materials and complex structures[54,55].

A typical electrodeposition setup is shown in **Figure 2.7a,** and the required components consist of cathode, anode, electrolyte system and electrical potential. When the potential is applied to the system, the species in solution get oxidized to ions, and travel to the surface of the substrate at the cathode where it is reduced to form the rough coating [54]. The control of surface morphology in electrodeposition can be varied by current density, voltage, time, temperature, and addition of additives[54,55]. To create superhydrophobic coatings through electrodeposition, two different approaches can be taken; (1) creating the roughness of surface through electrodeposition followed by chemical modification to obtain low surface energy the coating or (2) co-deposition of low surface energy as well as roughness into coating. Obviously, a one-step deposition process has advantages over the two- step process in creating the superhydrophobic surface.

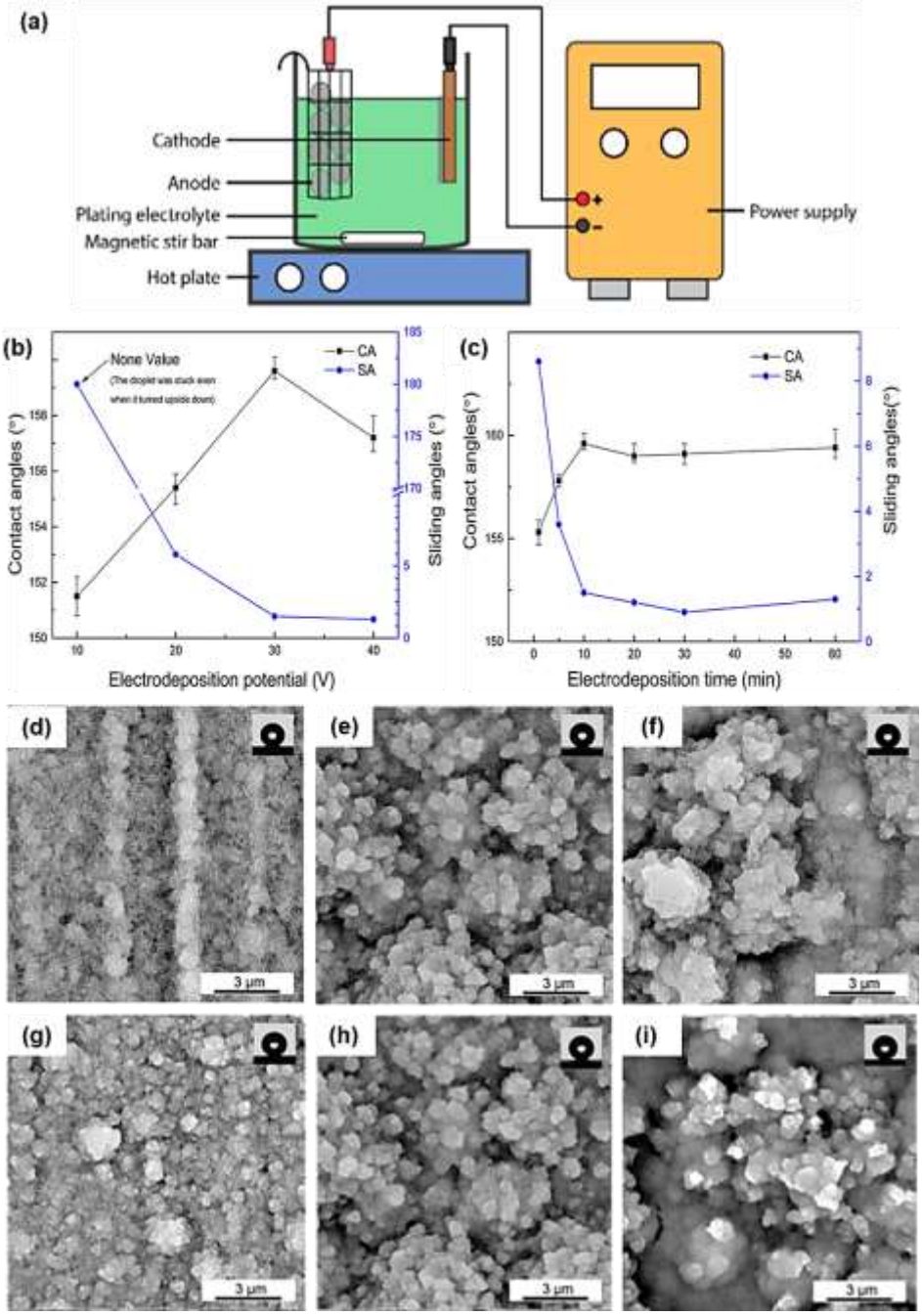

Figure 2.7. (a) illustration of electrodeposition setup [54], effect of electrodeposition (b) potential and (c) time on WCA and SA, and SEM images of potential deposition of co-deposition of Magnesium alloys at (d-f) 10, 30 and 40V and (g-i) 1, 10, and 30 mins, respectively[56].

Liu et. al. studied magnesium alloy electrodeposition using cerium nitrate hexahydrate and myristic acid in ethanol solution. **Figure 2.7b** shows the result from the study of varying applied potential during co-deposition on the WCA and SA of magnesium alloy[56]. Different

electrodeposition voltage was able to create different morphology on the surface of substrates. At potential lower than 30V, a sheet-like structure is observed (**Figure 2.7d)**. The hierarchical micro-nanoscale papillae structures were only formed and distributed homogenously at 30V (**Figure 2.7e)**. At a higher voltage of 40V, the morphology was destroyed (**Figure 2.7f)**. The electrodeposition time was also observed to affect the WCA and SA of magnesium alloys as shown in **Figure 2.7c**. A high WCA is observed after both 1 and 10 minutes of electrodeposition (**Figure 2.7g and 2.7h)** as the hierarchical papillae structures were homogeneously distributed on the surface of the magnesium alloy. The longer deposition time than 30 minutes (**Figure 2.7i)** caused a decrease in WCA due to the creation of holes by the prolong current flowing on the surfaces. The maximum WCA in this study was increased from 46.1^{o} to 159.8^{o} after co-deposition.

2.4.2.3 Lithography

Lithography refers to a technique where the projected patterns can be stamped or transferred onto the surface of materials. Photo-lithography was the original lithographic method used to produce patterns on substrate surfaces. Many different categories of lithography were later developed including soft lithography, nanoimprint lithography, laser lithography and nanosphere lithography. Among all, soft lithography standout due to lower cost, ease of pattern formation and more practical for large-scale productions[57]. Soft lithography creates micro and nanostructure patterns using self-assembly and replica molding strategies[57].

One common method is to utilize lotus leaf to create the micro-nano structure. Zhang et al. used soft lithography to fabricate superhydrophobic epoxy coating with PDMS as a template to replicate the micro/nano-structure from fresh lotus leaf[58]. **Figure 2.8a** illustrates the process of obtaining a superhydrophobic epoxy coating through soft lithography. The SEM images (**Figure**

2.8b and **2.8c**) revealed that the superhydrophobic epoxy coating exhibits the same topography (micropapillary structures) as the fresh lotus leaf with an average diameter of 10 µm, which might be responsible for the high WCA of 154^{o} for the modified coating. It should be noted that the smooth epoxy coating only exhibits WCA of around 87^{o}. The lotus leaf-like superhydrophobic epoxy coating also improved the corrosion resistance and barrier properties when immersed in 3.5 wt. % NaCl solution for 90 days, as compared to smooth epoxy coating. Confocal laser scanning microscopy (CLSM), shown in **Figure 2.8d**, was used to determine the surface roughness. It was found that the superhydrophobic coating had a roughness of about 3.57 µm.

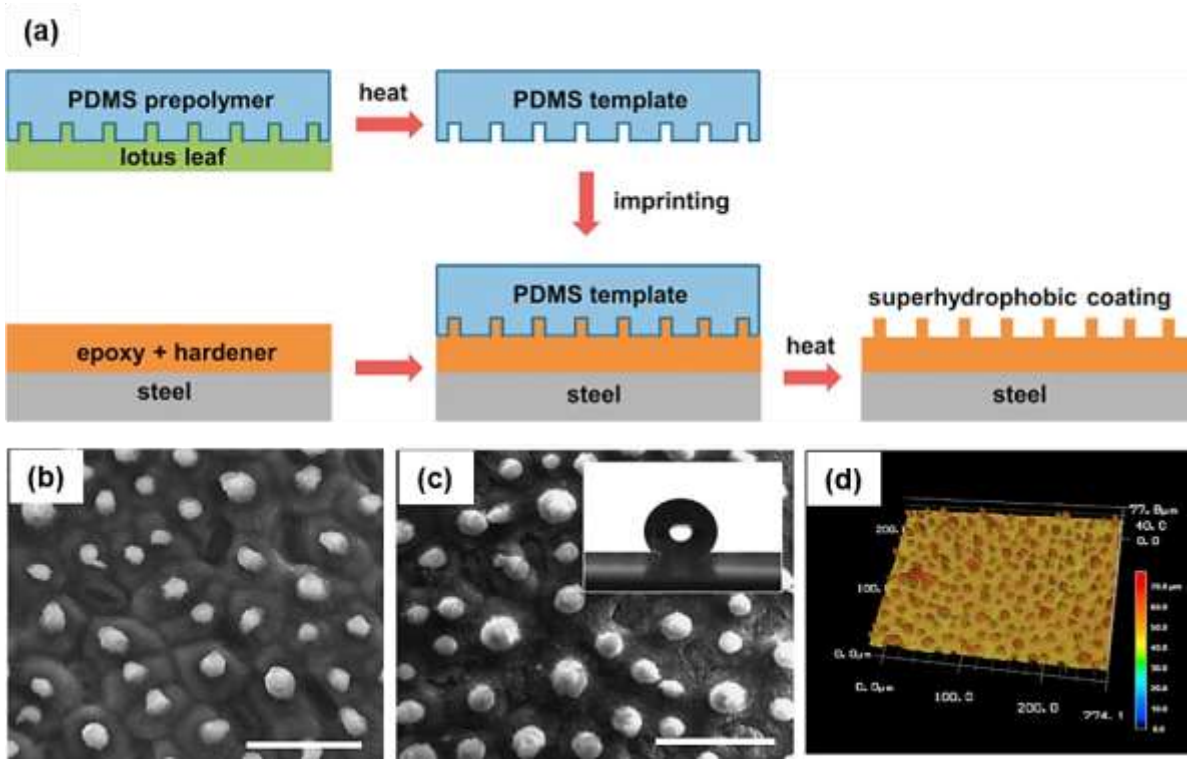

Figure 2.8. (a) schematic process of preparing superhydrophobic epoxy coating on steel using soft lithography, (b) SEM image of lotus leaf, (c) SEM image of the superhydrophobic epoxy. and (d) its micrograph from CLSM analysis[58].

Similarly, Wang et al. took advantage of the micro/nano-structure of fresh lotus leaf to create patterns on PDMS films[59]. These patterned PDMS films were used as a seal onto bamboo surfaces. The results showed that the topography of the treated bamboo contained micro-nano

papillate structures, which were responsible for the superhydrophobic and water corrosion resistance of the bamboos with an improvement in the WCA from 14.5 to 156.5^{o}. Similarly, Weng et al. used fresh Xanthosoma sagittifolium leaf to create the leaf-like pattern on PDMS templates, which was later transferred to the superhydrophobic electroactive epoxy (SEE) coating[60].The SSE coating exhibit an improvement in WCA from 81^{o} on smooth epoxy coating to 153^{o} on the pattern epoxy coating. The anticorrosion properties were also enhanced with the SEE coating.

Nanoimprint lithography (NIL) is another common technique used to produce the nanostructural pattern required for superhydrophobicity. The advantages of this technique are the economical outlook with efficiency in large-scale production[61]. **Figure 2.9** demonstrates the routine procedures of producing patterns on material surfaces using NIL. Three steps are involved in this technique: mold pressing, mold removal and reactive ion etching (RIE). In the first step, the mold containing nanostructures is pressed on the substrate with the resist film. Next, the mold is then removed, and the mold pattern transferred onto the resist film. This creates a thickness contrast in the resist film. In the last step, the RIE recognizes the thickness contrast and uses this to facilitate the elimination of any resist residual to obtain a clean nanostructure patterned surface[61,62].

Sung et al. used nanoimprinting technology to fabricate nanoscale pillar patterns on thermal shrinkage films (TSFs)[63]. **Figure 2.10a** shows the fabrication process where PDMS and poly (phenyl-co- methacryloxypropyl) silsesquioxane (LPMA64) were used as molds to create nano and micro complex pattern (NCMP) on bare TSFs. UV combined with CF_4/O_2 were then used as the etchant to remove all the residues from NMCP-TSFs. Finally, the NMCP-TSFs were shrunk using heat annealing. **Figure 2.10b** shows the SEM images of NMCP-TSFs with the nanoscale roughness maintained after heat annealing.

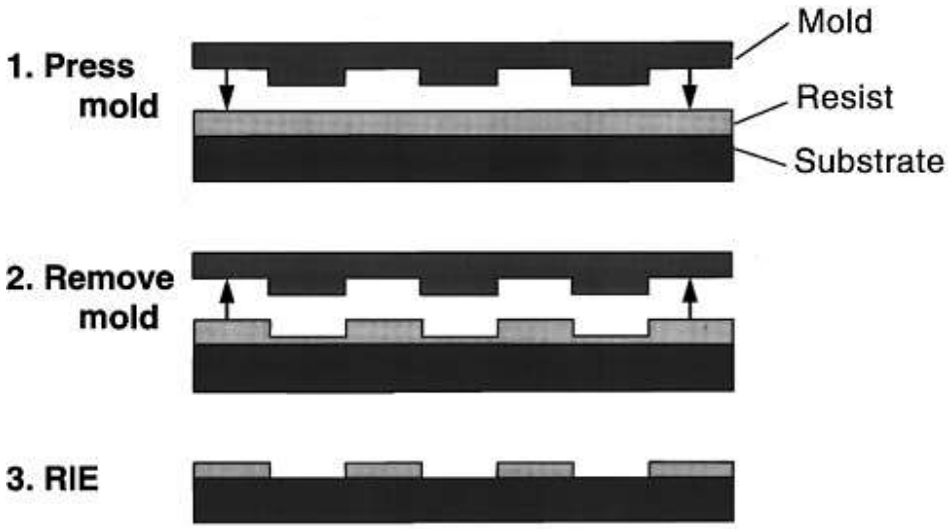

Figure 2.9. Schematic illustration of nanoimprint lithography [61].

This study also used the NMCP-TSFs as a master mold to first replicate the pattern on polyurethane acrylate, which later was contacted with polycarbonate film on glass substrate for a second replication. **Figure 2.10c and 2.10d** compare the morphologies of the first and second replica using NMCP-TSFs, respectively. The pattern seen in the second replica (**Figure 2.10d)** was similar to the original NMCP-TSFs (**Figure 2.10b)**, which justifies the similarity in WCA of 149.8 ^{o} and 150.3 ^{o}. **Figure 2.10e-2.10g** illustrate the self-cleaning ability of NCMP-TSF from the cleaning test with the silicon oxide nano powders coated on the surfaces. When the surface was tiled at a 4^{o} angle, water droplets start to roll off and taking along the nano-powder from the coated surface. The result confirmed that the NCMP-TSF superhydrophobic surface improved the self-cleaning effect.

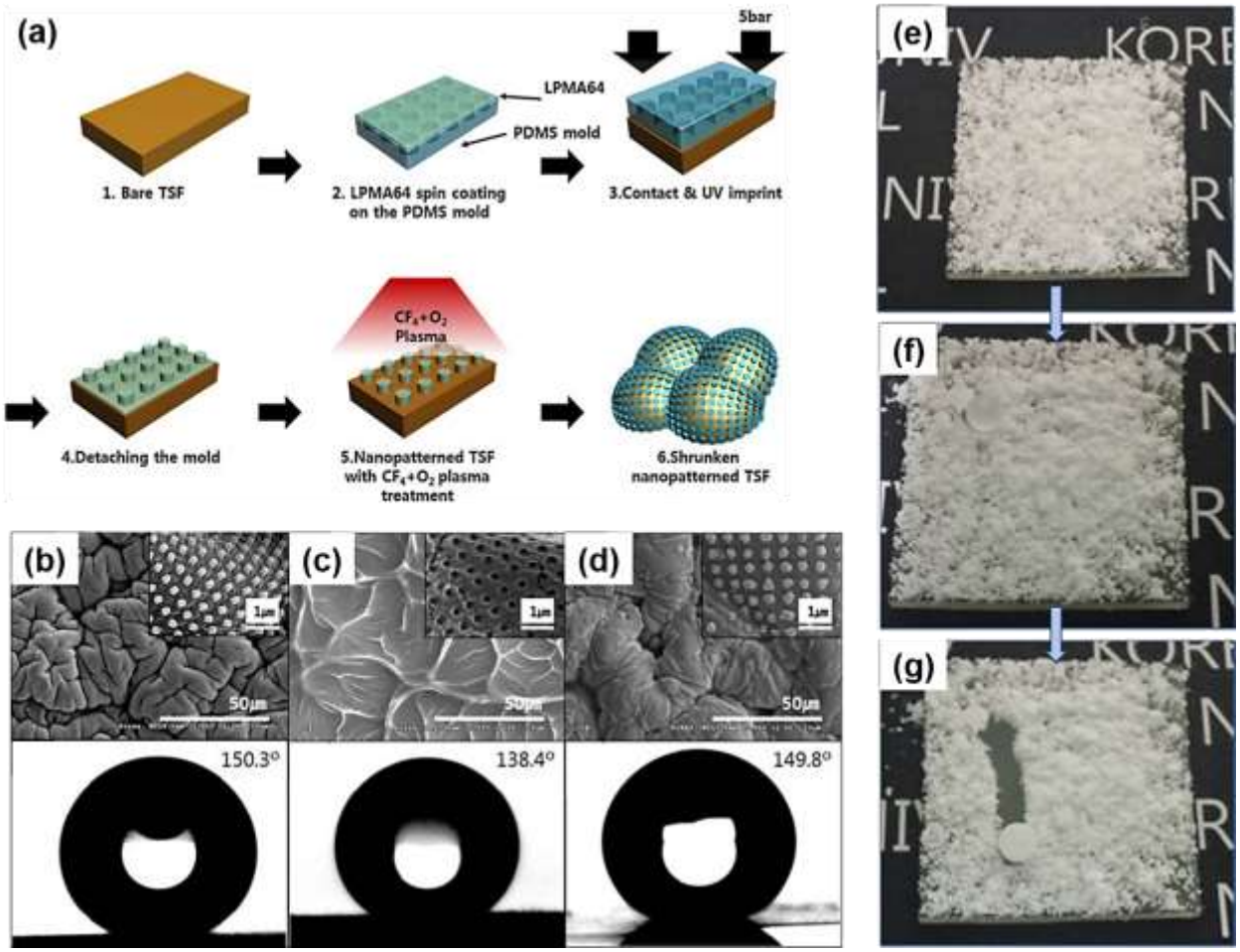

Figure 2.10. (a) graphic illustration of fabricating the shrunken nanopattern TSF via nanoimprint lithography. (b-d) are the SEM images and WCA of NMCP TSF, the first replication and second replication using NMCP TFS as a master stamp, respectively. (e-g) cleaning test of NCMP TSFs with silicon oxide powder before, during and after contact with water droplet [63].

2.4.2.4 Electrospinning

Electrospinning is a straightforward method used to produce continuous fibers (diameter ranging from micro to nanometers) for surface roughness of superhydrophobicity. However, this method did not gain a lot of interest from an industrial outlook due to the limitations to small scale production[64–66] . **Figure 2.11** illustrates a typical electrospinning system for the production of fiber-like materials. Typically, the syringe is filled with a polymer solution and a high electric field or force is used to overcome the surface tension of the polymer solution at the tip of the needle

attached to the syringe to create a liquid jet. The electrostatic field is further used to elongate the liquid jet thousands of times, thereby, producing very thin fibers. The fibers are collected at the collector plate and allowed to dry[65]. In order to prepare the superhydrophobic electrospun films, the polymer fibers from liquid jet are distributed randomly on the collector plate to form a very thin mat [67]. The surface morphology can be controlled by adjusting various parameters such as the polymer viscoelasticity, their conductivity level and surface tension[68,69].

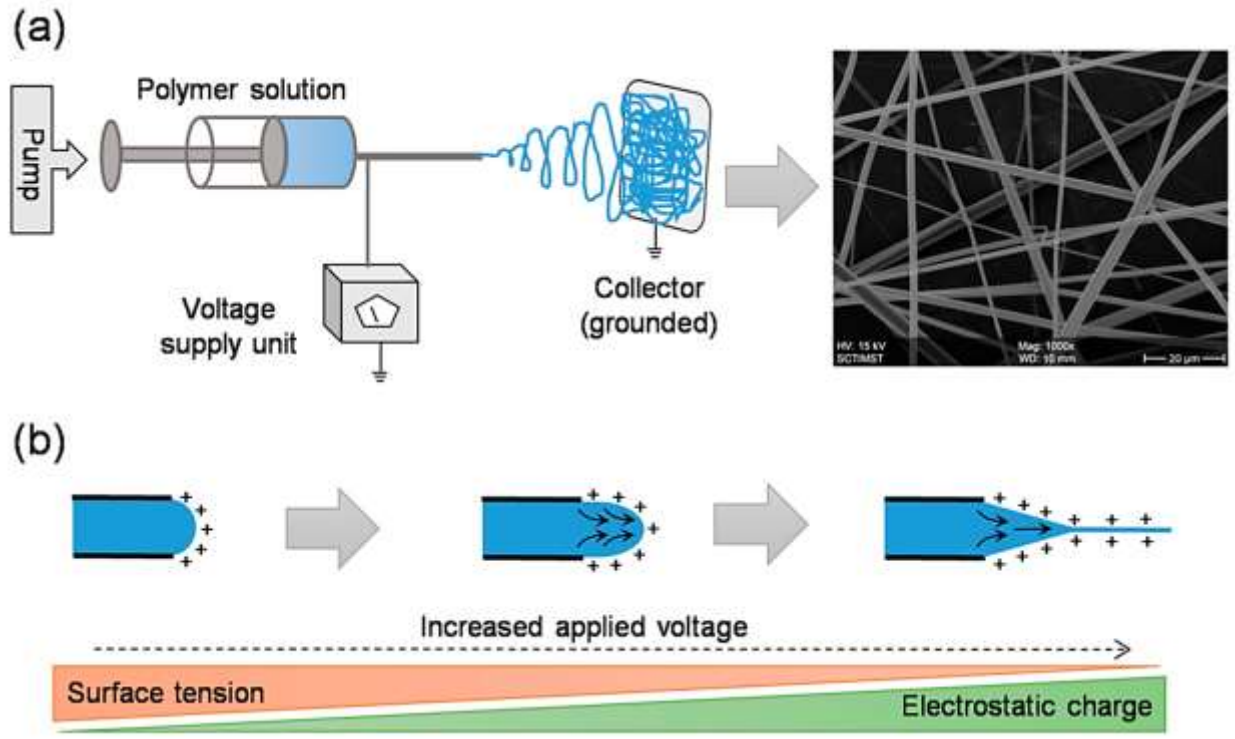

Figure 2.11. Typical setup for electrospinning process showing (a) application of voltage and extrusion of polymer solution through a syringe, leading to the formation of a smooth continuous fiber jet and (b) formation of fiber from syringe tip through solvent evaporation and fiber elongation [70].

Liu et al. was able to create superhydrophobic poly-vinylidene fluoride (PVDF) membrane with ZnO nanoparticles via electrospinning technique[68]. A solution of PVDF was prepared in ethyl acetate/DMF solution, after which ZnO nanoparticles and 1H,1H,2H,2H-perfluorodecyltriethoxysilane (POTS) used as low surface energy modification were incorporated

into the PVDF solution prior to electrospinning to form PVDF membranes. **Figure 2.12a-2.12d** show the effect of voltage during the electrospinning process on the diameter of the PVDF fibers. Increasing the voltage from 15 to 30 kV decreased the average diameter of the PVDF fibers from 237 nm to 85 nm. The highest WCA of the pure PVDF was 146 ±1.3 ^{o} at an operating voltage of 25 kV. At lower voltages, the fibers formed show uniform microstructure while micro/nanostructure are created at 25 kV.

However, the increase in voltage to 30 kV led to the transition from a micro/nanostructure to nanostructures, which resulted in a decrease in WCA of 141 ± 1.3^{o}. The morphology of the electrospun fibers changed with the incorporation of ZnO nanoparticles (**Figure 2.12e-2.12g**). The increase in ZnO content from 0 to 10 wt. % increased the diameters of the fibers from 127 nm to 1.8 µm with WCA from 146 ± 1.3^{o} to 171 ± 1.5^{o}, respectively. ZnO nanoparticles are known to increase the coarsening and roughness of the electrospun fibers as shown by the formation of nanodot on microfibers (**Figure 2.12g**).

Similarly, Radwan and et al. successfully prepared an effective corrosion protection coating with (PVDF) and ZnO using electrospinning technique. This coating provided better corrosion compared to bare PVDF for aluminium substrate and WCA was measured to be around WCA 155 ± 2^{o}. The roughness of the PVDF-ZnO nanocomposite coating has higher roughness of 40 nm compared to only 20 nm in PVDF coating as shown by AFM images (**Figure 2.12h and 2.12i**).

Again, the increase in surface roughness could be attributed to the cooperation of ZnO nanoparticle, which also increases the hydrophobicity of the coating. Moreover, the SEM images of PVDF-ZnO nanocomposite (**Figure 2.12k**) show strong adhesion to aluminium substrate

despite the PVDF coating forms large cavities from corrosion damages after immersing in 3.5% NaCl solution of Tafel test [71]. From these studies, it can be included that the electrospinning is a desirable method to create micro/nano-structure fibers and the incorporation of nanoparticles in the electrospinning process improve the properties of the membrane coating even further.

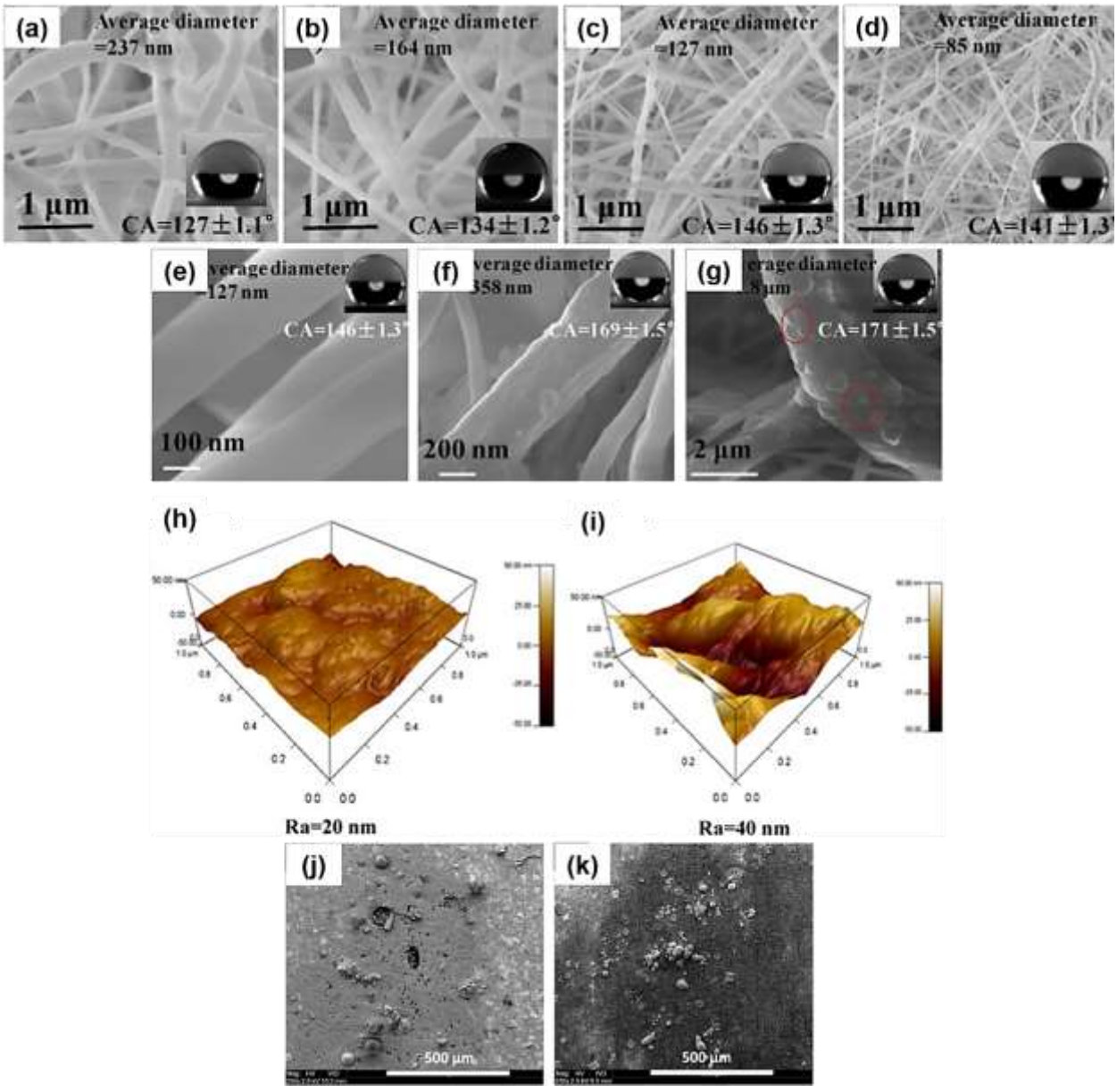

Figure 2.12. (a-d) SEM images of electro-spun fibers at 5, 10, 25 and 30 kV, respectively. (e-g) are the SEM images of PVDF membrane with 0, 5 and 10 wt. % of ZnO nanoparticle incorporation [68]; AFM images of (h) PVDF coating and (i) PVDF-ZnO nanocomposite

coating, respectively. (j, k) are SEM images of PVDF coating and PVDF-ZnO after Tafel polarization test in 3.5% NaCl solution [71].

2.4.2.5 Sol-gel process

Sol-gel process is used to form surface roughness through the engineering of micro/nano-structures on surfaces by the gelation of sol solution [72]. The first sol-gel synthesis was performed by Ebelman in 1846 to produce the silica gel[73]. The advantages of this method are low cost, low-temperature requirement, simple experimental setup and better control for the size and shape of the nanostructures[73,74]. In this process, the solution containing precursors are allowed to hydrolyze or polymerize to form a sol, which later forms a gelation network. Typically, the sol-gel process is accompanied by electro deposition, dip coating or spin coating to form thin films on the substrates. **Figure 2.13** shows the general process of utilizing sol-gel to form coating on substrates. Many factors can affect the sol-gel process and morphology of the coating including an initial concentration of precursors, type of solvent, pH of solution, nature of chosen precursors, gelation time and addition of catalyst[72].

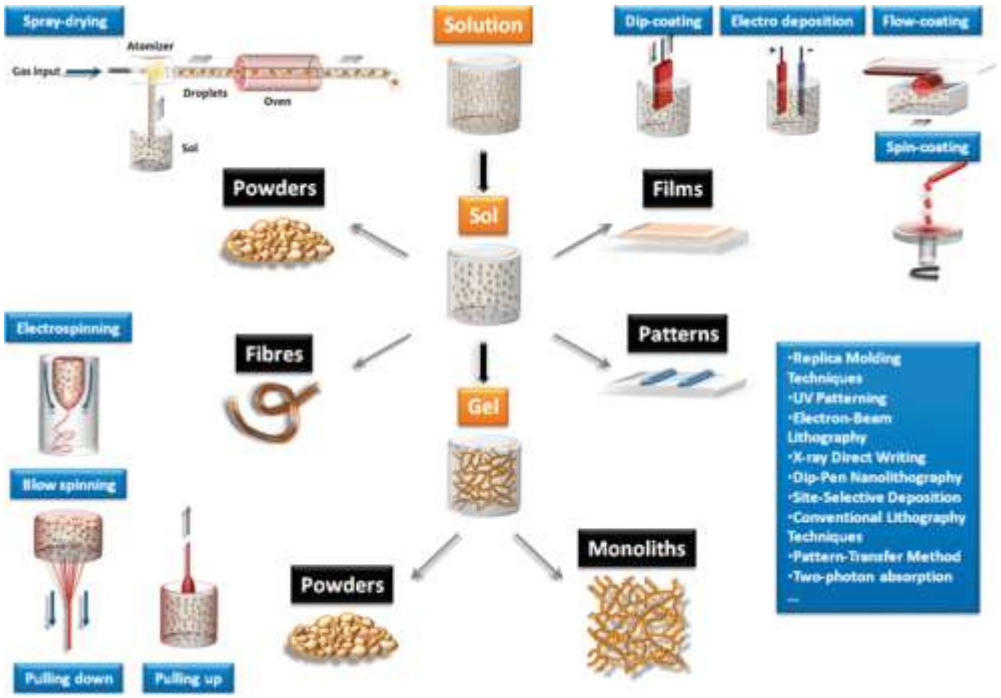

Figure 2.13. Application of sol-gel towards materials synthesis of (a) different forms and (b) methods used to synthesize the various forms of synthesized materials (Adapted from Sanchez et al.[75] with permission from RSC Publications copyright © 2011).

Liu et al. successfully prepared transparent and self-cleaning superhydrophobic coating from (Heptadecafluoro-1,1,2,2-tetrahydrodecyl) trimethoxysilane (17FTMS) via the sol-gel method[76]. The synthesis was performed in ethanol solution and ammonia was used as catalyst to assist the sol-gel chemistry. Through the hydrolysis and polycondensation of the methoxy group, the gel networks were formed. Glass substrates were dipped in the sol solution at different times: 10, 100, 300 and 600s. **Figure 2.14a-2.14d** show the effect of sol-gel deposition time on morphology of the coated glass substrates using FE-SEM and laser microscope. Increasing deposition times caused large hill-like islands formation and increased the surface roughness from 100 to 210 nm. This coarseness created air pockets in the surface grooves and allowed for water droplets to rest on the coated surfaces. However, the surface roughness of the coating decreased to 170 nm when the deposition time was extended to 600s. This was as a result of further network connection of islands to form smoother surfaces. The morphology of the coating was observed to

affect the WCA and revealed that the increase in roughness caused an increase in WCA. The coating after 300s of deposition time (**Figure 2.14c**) shows the highest WCA of 169^{o}. The sol-gel modified coating after 300s of deposition maintained its roughness and superhydrophobic property, despite the abrasion from high-speed water jet. During under water-jet impact test.

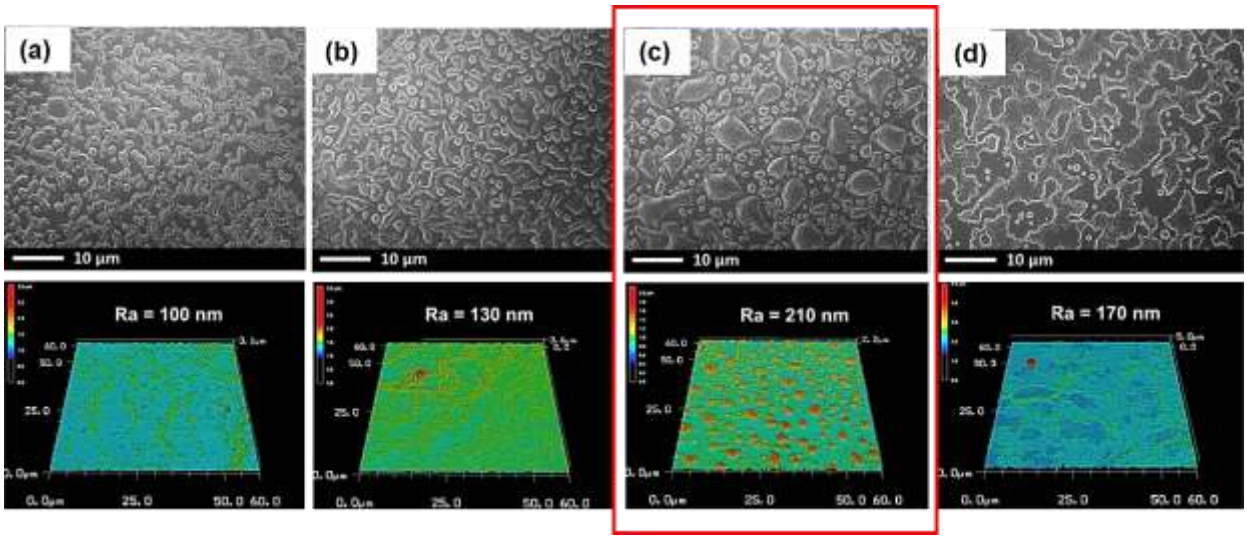

Figure 2.14. (a-d) showing FE-SEM and corresponding laser microscope images of coating at 10, 100, 300 and 600s of sol-gel deposition time, respectively[76].

2.4.2.6 Chemical vapour deposition (CVD)

Chemical vapor deposition (CVD) is a method of depositing a thin film of material on a substrate. Typically, precursors for deposition are carried in the vapor phase and a chemical reaction occurs in both the vapor phase and on the substrate to be deposited [77]. One advantage of using conventional CVD is that it is solvent-free and it can be used for the deposition of various complex structures on substrates[64]. **Figure 2.15a** shows the typical reactor for the CVD process. The gas-phase precursors are supplied through the gas precursor inlet and the carried gas carry the gas precursors to the heating zone of the reactor, where a chemical reaction occurs and produce intermediate precursors. Heat, UV and plasma energies can be used as sources of energy to initiate

the chemical reaction of the precursors[77]. These intermediates are then transported to the surface of the substrates, where they are adsorbed, diffused, nucleated and chemical reacted on the surface of the substrate to form a thin film coating. Finally, any unreacted species on the surface are desorbed from the surface[77,78].

Shang and Zhou developed porous silica coatings on glass slides for self-cleaning and anti-fogging applications[79]. **Figure 2.15b** shows the synthesis and preparation of hollow SiO_2 microspheres. First, the glass slide was primed by immersion in poly (diallyldimethylammonium chloride (PDDA) and followed by immersion in sodium poly (4-styrenesulfonate) (PSS). The treated glass slide was then immersed in the polystyrene@silica ($PS@SiO_2$) solution for a number of cycles and the calcination was used to remove the PS core and leave behind the hollow sphere SiO_2. **Figure 2.15c and 2.15d** compares the morphology of dense $PS@SiO_2$ microsphere and hollow SiO_2 microsphere. Deposition of 1H,1H,2H,2H-Perfluorodecyltriethoxysilane (PFOTS) on the surface of the hollow spheres to make them more hydrophobic was applied using CVD. The roughness of the surface coating was found to be proportional to the number of deposited cycles (**Figure 2.15e-2.15h**). Increased deposition cycles led to higher coating densities and WCAs (**Figure 2.15i**). The superhydrophobic coating with the hollow sphere also exhibited anti-fogging properties in comparison to bare glass (**Figure 2.15j and 2.15k**).

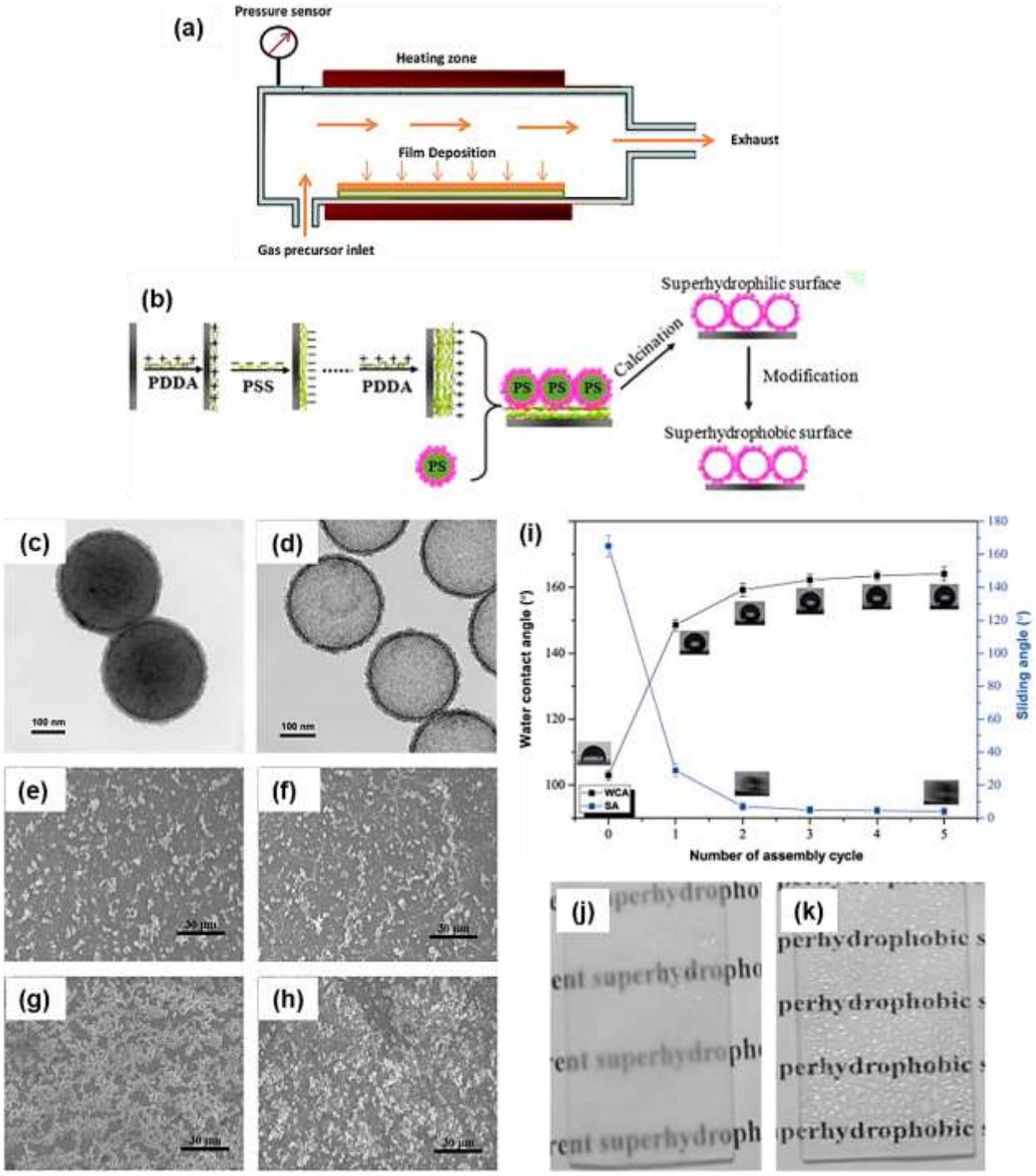

Figure 2.15. Schematic representation of (a) typical CVD reactor [78], (b) hollow SiO_2 particles preparation, (c and d) TEM images of dense PS@SiO_2 and hollow SiO_2 microspheres, respectively, (e-h) SEM images of hollow SiO_2 particles coated on glass slides with 2, 3, 4 and 5 cycles of fabrication, respectively, (i and j) bare glass and hollow sphere coated glass showing fogging and antifogging properties, respectively [79].

In recent years, aerosol assisted chemical vapor deposition (AACVD) has also gained a lot of interest. In AACVD, the precursor is first dissolved in a solvent and deposited onto the surface of a substrate as aerosol droplets. The advantage of this technique is that any involatile precursor can be utilized as long as they are soluble in suitable solvents[80,81]. Zhuang et al. prepared hierarchical micro-nano-structured PTFE films on glass substrate via AACVD. A similar result was found; the WCA was observed to increase with increasing surface roughness. However, the coating transparency reduced with the increase in roughness[80]. Although, the CVD process can produce good surface roughness for superhydrophobicity, this method is not considered a viable method as a sealed vessel is required and is not suitable for larger scale or object deposition.

2.4.2.7 Spray coating

To prepare the superhydrophobic surface, many engineering methods can be used as discussed in the previous sections. However, methods are either primarily based on laboratory conditions or relatively low-cost equipment. Moreover, they are tedious processes and hamper the broad use of substrates categories. Spray coating has been considered to be an ideal approach considering that it is less time consuming and more practical on an industrial scale. The superior functionality of spray coating is that it can be used on both new and surface damaged substrates[82]. Typically, the coating species are dispersed in solvents and sprayed onto substrates using a spraying gun.

Liu et al. prepared superhydrophobic coatings via spray coating using a PDMS/PMMA hybrid[82]. PDMS and PMMA were dissolved in THF solution and sprayed onto a glass substrate. The WCA of 157.5^{o} was achieved and the coating was shown to have good stability against sand abrasion, water impact droplet and stable in strong acid and alkali solutions.

In recent years, many studies have focused on spray-coated various nanoparticles onto substrates to create superhydrophobic coatings. Feng et al. was able to prepare superhydrophobic coatings via spray coating of modified halloysite nanoparticles on different substrates[83]. Halloysites (HNTs) are nanoclays, containing silanol groups on their surface, which readily react with silane agent and form polysiloxane modified nanoparticles (POS@HNTs). The modified nanoparticles were dispersed in toluene and sprayed onto different substrates. The super-antiwetting coatings prepared are demonstrated in the schematic shown in **Figure 2.16a**. The morphology comparisons of HNTs and POS@HNTs were analyzed using TEM and are shown in **Figure 2.16b**. The HNTs observed to be without any surface coatings while the POS@HNTs exhibited a layer of polymer surrounding nanotubes. The SEM images (**Figure 2.16c)** reveals the increase in surface roughness of POS@HNTs coating, which is from the silanization of nanoparticle surface modification. Four different substrates (steel, cotton, paper and wood) were coated with POS@HNTs and a droplet of water was placed on each substrate (**Figure 2.16d).** The results show that the POS@HNTs can be coated on different substrates while maintaining superhydrophobicity with a WCA ranging from 153-157^{o}. Aside from clay nanoparticles, silica nanoparticles are commonly used to prepare superhydrophobic coatings via spray coating.

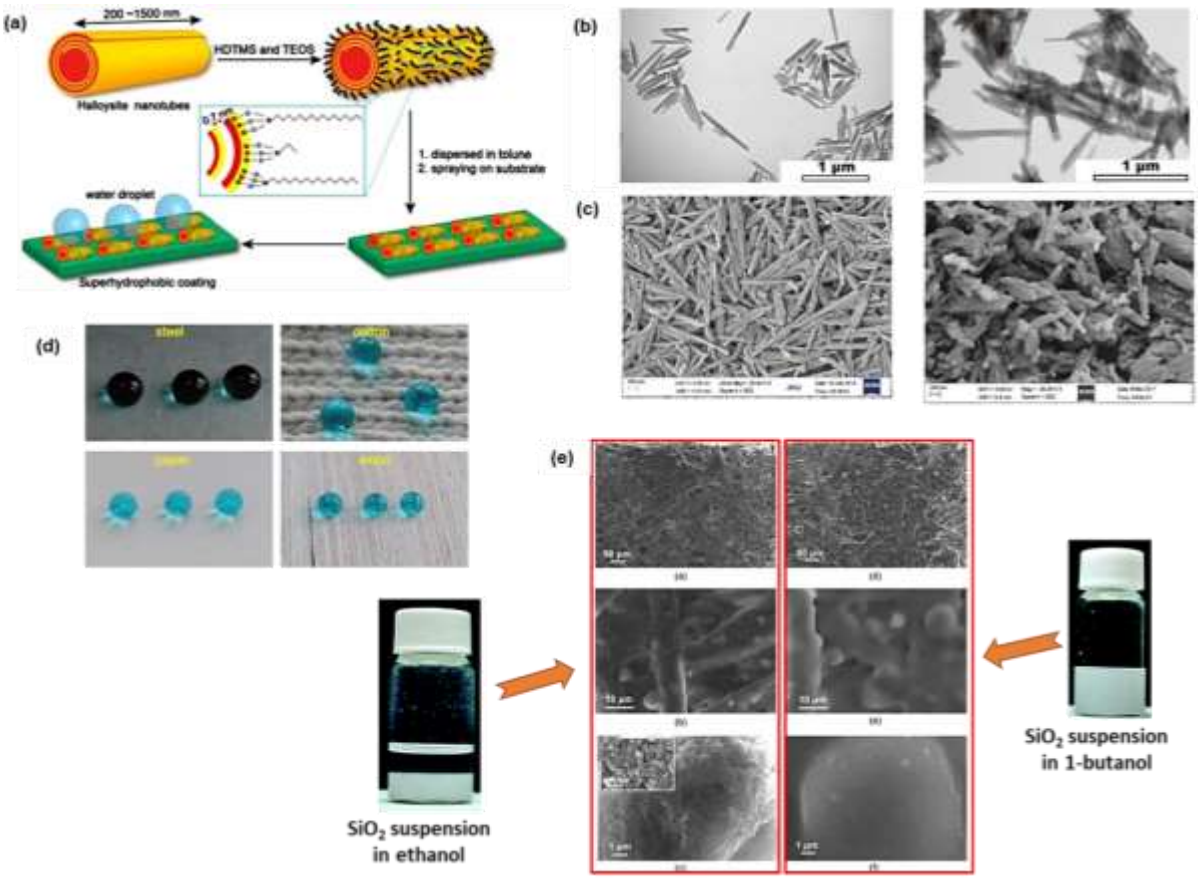

Figure 2.16. (a) schematic of preparing superhydrophobic through spray coating of halloysite nanoparticles, (b, c) TEM and SEM of unmodified HTNs (left) and POS@HNTs (right), respectively and (d) photographs of a blue-dyed water droplet on different POS@HNTs coated substrates [83], (e) photograph of SiO_2 in ethanol and 1-butanol and their corresponded SEM images at different magnification[84].

Ogihara et al. spray-coated various alcohol suspensions of SiO_2 nanoparticles on paper[84]. The results show that different alcohol solvents affect the aggregation state of nanoparticles and results in different WCA and SA. **Figure 2.16e** shows the photograph of SiO_2 suspended in ethanol and 1-butanol solution, and their corresponding SEM images at different magnification. The SEM images at low magnification reveal similar morphology regardless of the solvent used for spraying; however, at higher magnifications, the coating from SiO_2 dispersed in ethanol exhibited micron-scale rough surface and higher WCA of 155^o and SA of 7^o. However, the coating from SiO_2 dispersed in 1-butanol exhibited a smoother surface with a WCA of only 149 ^{o} and SA of 50^o.

From the dispersion photograph, the SiO_2 nanoparticles are observed to aggregate and settle more in ethanol even before spraying while SiO_2 is observed to disperse better in 1-butanol, leading to finer particles during spraying and a smooth surface coating. Similarly, Li et al. prepared non-fluorinated superhydrophobic coating by spraying suspensions of trimethoxypropylsilane-silica nanoparticles sol solution on glass sides with a WCA of 158.5^o[85]. In addition to water repellent property, the modified coatings are proven to be stable under high temperature, humidity and UV radiation. In conclusion, the spraying method reduces the amount of starting materials, entails simple and straight forward solution preparation, is less time consuming, requires less expensive equipment and can easily to be used to coat any surface including damaged surfaces.

2.4.2.8 Composite coatings

All the previous discussions have focused on the preparation of superhydrophobic surfaces from low surface energy materials such as fluorine-based materials, nanoparticles and inorganics. In this section, the effect of combining low surface energy materials with hydrophobic polymers and their effect on superhydrophobicity is discussed. Similar to the sol-gel process, formulation of composite coatings is further accompanied by application techniques such as dip coating, brush painting, spin coating and spray coating.

Qing et al. successfully prepared a superhydrophobic composite from modified TiO_2 and polyvinylidene fluoride (PVDF)[86]. TiO_2 was modified with heptadecafluoro-1,1,2,2-tetradecyl) trimethoxysilane (FAS) to form FAS-TiO_2, mixed with PVDF, curing agent, dispersant and catalyst to form composites as shown in **Figure 2.17a**. The coatings were deposited on copper substrates by dip coating, resulting in a WCA and SA of 160.1° and 5.5°, respectively. The surface morphology of FAS-TiO_2 (**Figure 2.17b**) exhibits agglomeration on a monolayer film with roughness, while the composite of FAS-TiO_2/PVDF (**Figure 2.17c**) shows the micro/nano-

structure s with an increase in surface roughness, leading to a change in WCA from 154.3° to 160.1°. AFM image analysis (**Figure 2.17d and 17e)**, reveal that the surface roughness of the composite was 58.8 nm as compared to just 50.6 nm in FAS-TiO_2 coated substrate. One interesting discovery from this study is that the coatings have switchable wettability from UV and heat exposure. **Figure 2.17f** shows the effect of UV exposure time on the WCA of coatings. The WCA was observed to decrease with increasing UV exposure time. The opposite effect was observed when the coatings were heated; the WCA increased with heating time (**Figure 2.17g**).

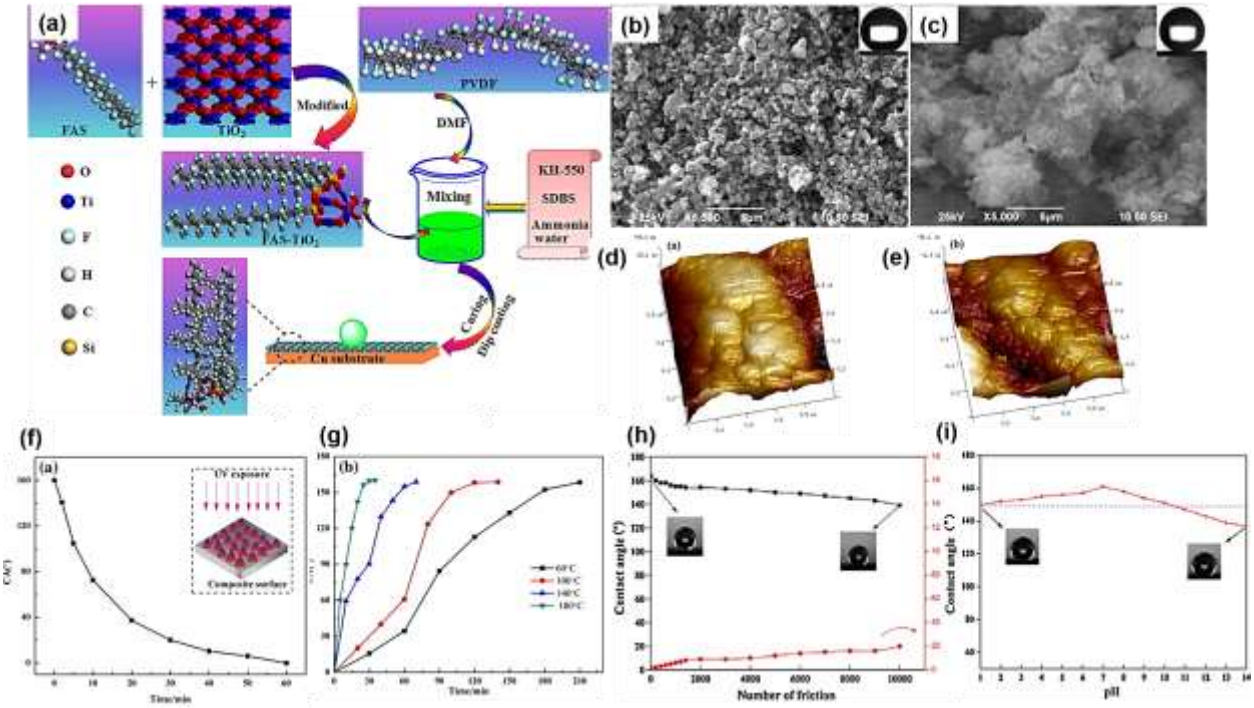

Figure 2.17. (a) schematic process of preparing superhydrophobic composite on Cu substrate (b, c) SEM (d, e) AFM images of FAS-TiO_2 compared to FAS-TiO_2 composite coating, respectively (f) WCA as a function of UV exposure time (g) the effect of heating temperature on WCA of coating[86], (h) the abrasion and (i) pH effect on WCA of the PVDF/FEP/CNFs coating [87].

Wang et al. prepared a similar coating from PVDF/fluorinated ethylene propylene (FEP)/carbon nanofibers (CNFs) with wear and corrosion resistance properties[87]. In this study, PVDF, CNFs and FEP were mixed together to form a composite, which was then spray-coated onto HCl acid etched aluminium plate. A WCA of 164 ± 1.5° was obtained, resulting from a

combination of the etching process and composite coating. **Figure 2.17h and 2.17i** show the effect of abrasion and pH on WCA of the superhydrophobic coating. The coating demonstrates the good wear resistance and stability in acidic and alkaline solution with an insignificant effect on the WCAs.

2.5 Hydrophobic and superhydrophobic nanocellulose

With a heightened sense of urgency and concern for the environment, an increasing number of scientists have delved into developing renewable, biobased materials to partially or fully replace those currently used in various applications. Regarding the raw materials used for superhydrophobic surfaces such as fluorinated materials and silicones, researchers have shifted their interest in biodegradable and bio-sustainable raw materials.

Cellulose, consisting of a repeating unit of β (1→4) D glucopyranose is considered the most abundant polymer with 1.5 $x10^{12}$ tons of total annual production[3,88]. The dissolution of amorphous domains in cellulose yields interesting nanoparticles called nanocellulose[88]. Two main nanocellulose that have gained so much interest due to their intrinsic properties are cellulose nanocrystals (CNCs) and cellulose nanofibrils (CNFs)[2]. In this section, the utilization of CNCs and CNFs in superhydrophobic applications are discussed.

2.5.1 Cellulose nanocrystals

Cellulose nanocrystals (CNCs) are rod-like nanoparticles as shown from TEM image in **Figure 2.18a** with a range in width and length of 3-5 and 50-100 nm, respectively[2,3]. However, these ranges can be wider depending on the biomass source used. CNCs are found in diverse biomass sources including wood, cotton, hemp, linen, tunicates and bacterial cellulose. The isolation of CNC nanoparticles is achieved through acid hydrolysis. The surface chemistry of

CNCs is very interesting due to the abundance (-OH) functional group, which allows for a variety of chemical modification with low surface energy materials[89]. In addition, the high surface area to volume ratio makes this nanomaterial suitable for superhydrophobic applications[2].

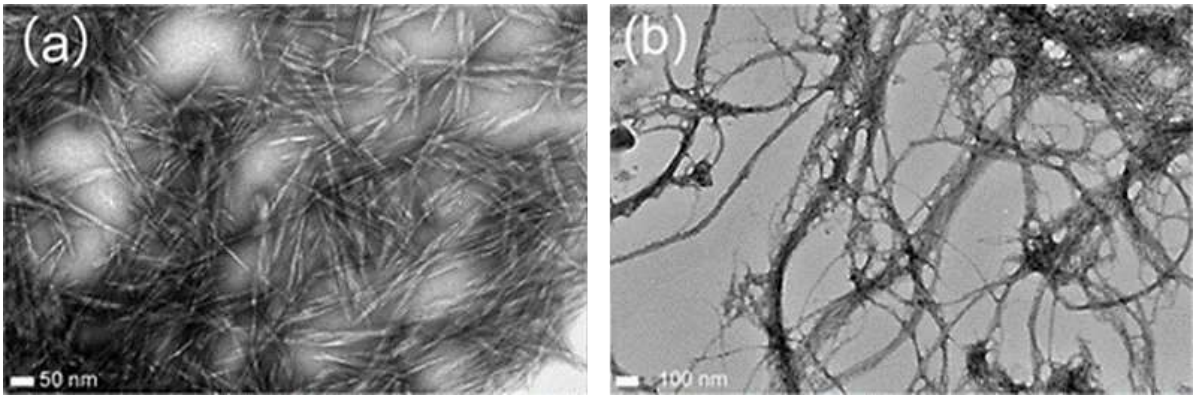

Figure 2.18. Transmission electron microscopic images of (a) CNCs and (b) CNFs[3].

There are many studies on the preparation of hydrophobic/superhydrophobic surfaces using CNCs through surface modification of CNC with low surface energy, incorporating CNC nanoparticle to create micro/nano-structure surface roughness or a combination of both methods. In the literature, the chemical modification of CNCs is achieved by attaching low surface energy agent such as fatty acids, silanes and fluorinated materials, while the surface roughness techniques involve the use of spay-coating, dip-coating, sprinkling and CVD. Hu et al successfully created hydrophobic CNCs by modifying the CNC surface with tannic acid (TA), followed by the incorporation of decylamine (DA) at room temperature as shown in reaction scheme in **Figure 2.19a**[90]**.** It is believed that TA oxidized and reacted with CNC at a pH of 8 to form quinones, which reacted with the primary amine of DA through Schiff base reaction and/or Michael addition. The WCA of CNC improved from 21^{o} to 74^{o}, which was attributed to the alkyl chain of DA.

Salam et al. modified CNCs in a mixture of toluene/pyridine solution with pentafluorobenzoyl chloride, which is a fluorinating reagent. The modified CNCs were more easily

dispersed in acetone due to strong fluorine-fluorine repulsion of the surface-modified CNCs. As a result, affinity towards the water was reduced for the modified and hence, increased the to 112^{o} at 10 s[91].

Although the hydrophobicity of CNC has been improved with the addition of low surface energy agents, it is not sufficient enough to create superhydrophobic CNCs without engineering surface roughness. **Figure 2.19b and 2.19c** show the reaction mechanism for creating superhydrophobic surfaces by utilizing both low surface energy materials and engineering surface roughness. Cheng et al. was able to prepare novel and degradable superhydrophobic cotton fabric with a WCA of 157^{o}[92]. The cotton fabric was dip-coated in a solution containing epoxidized soybean oil (ESO) and curing agents. The cotton fabric was then immersed in a CNC water dispersion, cured and finally modified with hexadecyltrimethoxysilane (HDTS). Morphology study through SEM revealed that the surface structure of the cotton fabric became rougher after the addition of CNC nanoparticles, with an increase in WCA to 143^{o}. However, a maximum WCA of 157 ^{o} was reached only after surface modification a with a silane agent. The superhydrophobic surface stability was also analyzed and revealed that the wettability of the cotton fabric remained unchanged after water immersion, decane and DMF. The fabric also exhibited good resistance to acid and alkali solutions.

Huang et al. was able to prepare necklace rod-like CNC/SiO_2 nanostructure via in situ growth and sprayed them onto substrates with commercial spray adhesive to create superhydrophobic coatings[93]. In the preparation process, the ethanol solvent exchange of CNC aqueous solution was performed and then modified with tetraethyl orthosilicate (TEOS) to form and grow CNC/SiO_2 rods. The ethanol solution containing CNC/SiO2 rods were then smeared or sprayed onto glass, wood, textile and filter paper, which were applied with the spray adhesive

beforehand and finally the coatings were allowed to dry to remove any excess ethanol solution with the step-by-step procedures illustrated in **Figure 2.19b**. For all substrates, the WCAs were observed to be greater than 159º. The presence of network-like structures by CNC/SiO_2 nanoparticles are responsible for the micro/nano-structure of the coatings and hence the superhydrophobic properties.

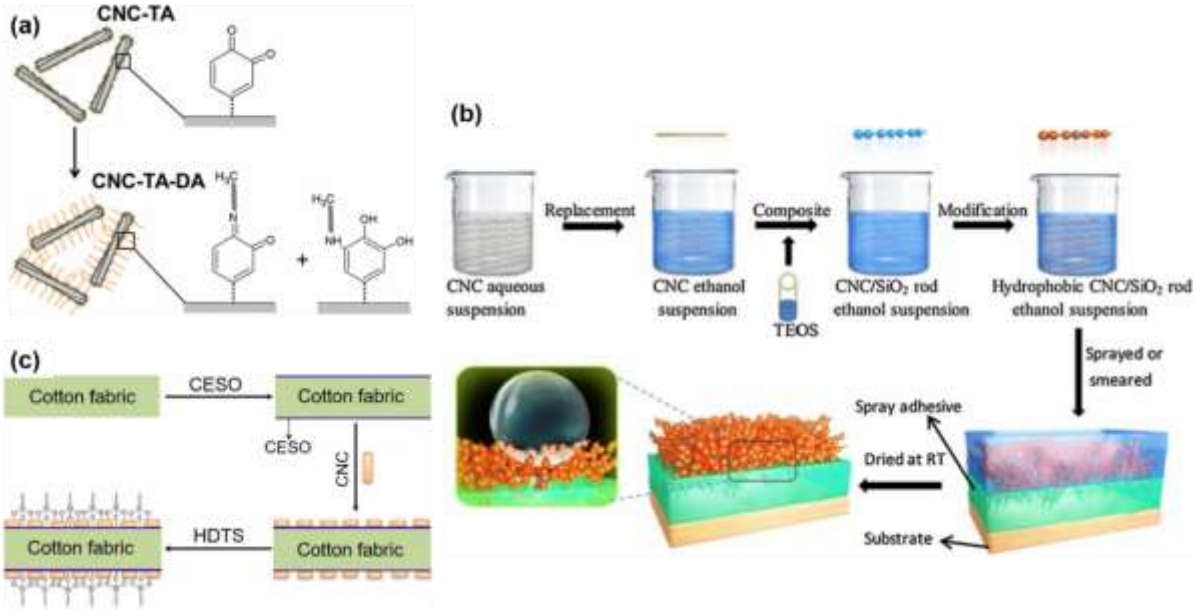

Figure 2.19. Reaction schemes of hydrophobic/superhydrophobic CNCs showing (a) the modification of CNCs with tannic acid and the functionalization with decylamine [90], (b) in situ growth of necklace rod-like CNC/SiO_2 nanostructures on CNCs[93] and (c) epoxidized soybean oil modification of CNC producing superhydrophobic degradable surfaces[92].

2.5.2 Cellulose nanofibrils

Cellulose nanofibrils (CNFs) are the smallest unit of cellulose nanofibers having network-like nanoparticles (**Figure 2.18b**). Similar to CNCs, CNFs are derived from wood or other agricultural products and can be isolated through mechanical and chemo-mechanical processes[2,4]. The properties of CNFs such high aspect ratio, high Young's modulus, high crystallinity, low density, sustainability, and biodegradability attract researchers to investigate its application ranging from superhydrophobic surfaces to aerogel applications[4,94].

Zhou et al. successfully prepared superhydrophobic CNF-assembled aerogels through freeze-drying of silylated CNF and SiO_2 nanoparticles suspensions[4]. The SiO_2 was added into the suspension of CNFs, and then methyltrimethoxysilane (MTMS) was incorporated to form -Si-O- networks and lower surface energy as shown in **Figure 2.20a**. SEM analysis revealed aerogel morphology with hierarchical structures with roughness, which contributed to an increase in WCA of up to 168.4°. This composite aerogel was used to separate oil from surfactant stabilized water in an oil emulsion with an efficiency greater than 99%. In addition, the superhydrophobic aerogels have strong antifouling properties and can be recycled.

Mertanieme et al. compared two different approaches of preparing superhydrophobic coating on glass substrates **Figure 2.20b**) by spraying CNFs followed by fluorination through CVD (**Figure 2.20c**), and fluorination of CNFs followed by spraying[95]. Tridecafluoro-1,1,2,2-tetrahydrooctyl trichlorosilane (FOTS) was used as a fluorination reagent to reduce the surface energy of CNFs and form CNF superhydrophobic coating. In both approaches, hierarchical surface roughness, similar to that of the lotus leaf was observed to have similar WCAs (169 ± 4^o and 163 ± 3^o).

However, the technique involved in the fluorination prior to spraying is more efficient because of a one-step coating process. Uniform and dense layers were observed from the morphological analysis as compared to that of the other method. The superhydrophobic properties were confirmed by the appearance reflected light from the air-water interface of trapped air when the coated glass was immersed in water (**Figure 2.20d**). CNFs has also been used to prepared superhydrophobic and high thermal insulation surfaces[96]. In that study, methytrimethoxysilane was used to modify CNFs to form polymethylsilsesquioxane−cellulose nanofiber (PMSQ-CNF)

composite aerogels via sol-gel process. The PMSQ-CNF composite aerogel exhibited low density and thermal conductivity and high flexibility, making it a practical insulation material.

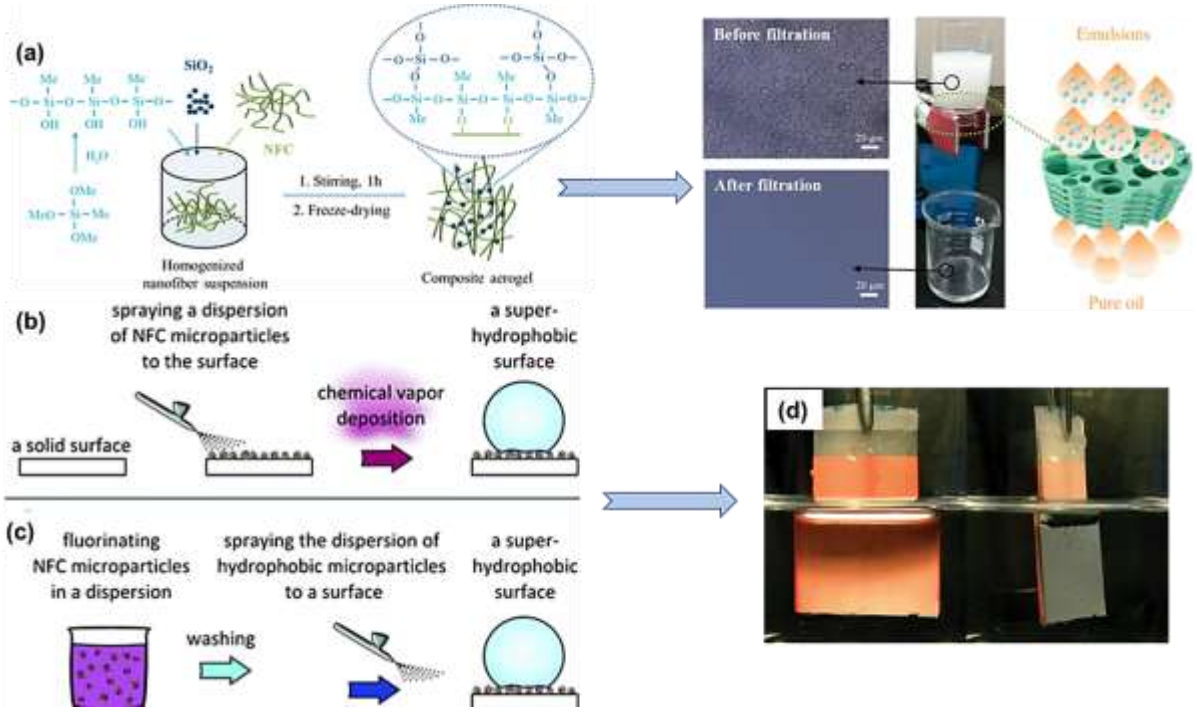

Figure 2.20. Schematic showing the preparation process of (a) superhydrophobic CNF-assembled aerogel and the oil-water separation process [4]. Two approaches of preparing superhydrophobic coatings with (b) fluorination after dry spraying and (c) spraying before fluorination reaction, respectively; (d) photograph of light reflection test of superhydrophobic coated glass with the orange paper attached to the back of the glass slide to enhance the visibility of trapped air at the air-water interface [95].

Fabrication of hydrophobic/superhydrophobic materials using the abundant and biodegradable nanocellulose in various studies have been demonstrated to be a to sustainable, renewable and environmentally friendly viable route and alternative to synthetically produced materials. The nanocellulose is not only used for superhydrophobicity but can introduce thermal and mechanical strength to the materials. A summary of up to date investigations relating to the utilization of CNCs and CNFs nanoparticles for hydrophobic and superhydrophobic coating is given in **Table *2.1***.

Table 2.1. Summary of chemical modifications of nanocellulose for hydrophobic/superhydrophobic functions/applications.

Material	Modifying agent	Method	Substrates	Features	Ref.
CNCs	Cured epoxidized oil resin (CESO)	Dip coating	Cotton fabrics	- High stability, chemical and solvent resistances with a WCA of 157° - Oil/water separation application (98% efficiency) and degradability in buffer solution	[92]
	Tetraethyl orthosilicate (TEOS)	Spraying/ smearing	Glass, wood, textile, paper	- Ultra-high mechanical robustness, abrasion resistance with a WCA of greater than 159° - Stability under acid and alkaline as well as UV radiation	[93]
	Perfluorooctyltrichlorosilan (FOTS)	Spraying	Stainless steel mesh	- Demonstrated good self-cleaning, high mechanical strength, high resistance to corrosion and UV radiation with a WCA of 163 ° with potential for oil/water separation	[97]
Lignin coated CNCs	1H,1H,2H,2H-perfluorooctyltrichlorosilane (PFTS)	Sprinkling	Glass slide	- WCA of greater than 161° depended on adhesive used - Self-cleaning, high mechanical strength, durability under sand abrasion, winger-wipe, knife scratch, water jet, UV, high temperature, acid and alkaline solution	[98]
CNCs	Lignin, methyltrimethoxysilane (MTMS)	Spray drying	Filter paper	- Excellent Water repellent and self-cleaning ability with a WCA of 165.2° with 10% lignin - Lignin addition caused doughnut-shaped microparticle which lead to fast evaporations	[99]
	perfluorononanoic acid, Perfluoroundecanoyl chloride	Spin coating	Multipurpose paper	- WCA of greater than 150° - Application in packaging materials, outdoor clothing, textiles and microfluidic devices.	[100]
Lignin coated CNCs	Polyvinyl alcohol (PVA), Perfluorooctyltrichlorosilane	Spraying/CVD	Wood	- Potential for food packaging with a WCA of greater than 157° - Self-cleaning, good abrasion resistance and no addition of organic solvent	[101]
CNCs	Pentafluorobenzoyl chloride	N/A	N/A	- Excellent hydrophobic and oleophobic properties with WCA of 112°	[91]
	Isocyanate-terminated castor oil,	N/A	N/A	- Surface energy dropped to almost zero from 21.5 mJ/m^2 with WCA of 97°	[102]
	Tannic acid, decylamine	Spin coating	Si wafers	- Bio-based nanoparticles with a WCA of 74°	[90]

	Alkylquaternaryammoniumbromides / acryloylchloride	Spraying	Wood	- Increased scratch resistance from 24 to 38%	[103]
CNFs	Trichlorovinylsilane (TCVS), perfluoroalkyl thiols	N/A	Glass slide	- The film is highly transparent, flexible and patternable with a WCA of 167° - Photo "click" thiol–ene reaction induced by UV light - Potential in biosensing, display protection, biomedical and diagnostics devices.	[94]
	Alkyl ketene dimer (AKD) or amino propyl trimethoxy silane (APMS)	Rod coater	Paperboard	- Reduced cracking in the coating with a WCA of 150° with AKD modified CNFs - Potential for bio-based building materials, lab-on- chip microfluidic devices and food packaging.	[104]
	Methytrimethoxysilane	N/A	N/A	- A potential material for thermal insulation with a WCA of greater than 150 - Composite aerogels PMSQ-CNF show good flexibility, low-density thermal conductivity	[96]
	Precipitated Calcium Carbonate (PCC), alkyl ketene dimer (AKD)	Dip coating	Filter paper	- WCA of greater than 160 - CNFs act as binder to bind PCC particle onto filer paper.	[105]
	Methyltrimethoxysi- lane (MTMS), silica (SiO_2) nanoparticles	N/A	N/A	- Great antifouling performance with WCA of greater than 168.4 - Aerogel used for separation oil from water-oil emulsion with an efficiency of >99%	[4]
	Tridecafluoro-1,1,2,2-tetrahydrooctyl) trichlorosilane (FOTS)	Dried spraying	Glass	- WCA of 169 ± 4^{o} and163 ± 3^{o} depend on the coating method - Reflection test demonstrated superhydrophobic properties of coating	[95]
CNCs	Surfactants	Casting	Glass	- More than 100 % increase in WCA	[106]

2.6 Superhydrophobic coating and corrosion resistance

2.6.1 Mechanisms of corrosion resistance

One of the main applications of superhydrophobic surface is to enhance the corrosion resistance of metal substrates. Aluminum, copper, magnesium, zinc substrates are among the candidates that have utilized the advance technology of superhydrophobicity [107]. Two factors can be used to explain mechanisms of anticorrosion of superhydrophobic surfaces. First, the superhydrophobic surfaces work by acting as a passivation layer and preventing underneath metal substrates from undergoing electrochemical reaction and hence metal corrosion [107]. The micro and nano structural surface roughness of superhydrophobic surfaces allow airs to be trapped in the surface grooves and prevent corrosive ions such as Cl^- ions to penetrate through surfaces and destroy the substrates. **Figure 2.21** demonstrates the process of superhydrophobicity in preventing corrosives ions from getting through the surfaces and protect metal from corrosion. Second, capillary forces are also accounted for the corrosion resistance of superhydrophobic coatings [108]. The roughness of superhydrophobic surface are thought to work as a vertical cylinder. Typically, when a cylinder is placed in water, the solution rise and forms a meniscus shape inside the cylinder tubes. This phenomenon is true when the cylinder is made from hydrophilic materials. When the surfaces of the tube is hydrophobic, the liquid is depressed [107,108]. **Equation 4** can be used for calculating the height of liquid rise of capillary tubes.

$$h = \frac{2\gamma cos\theta}{\rho g R} \qquad (4)$$

where γ, θ, ρ, g, R are surface tension, water contact angle, liquid density, gravity acceleration and a radius of cylinder tube, respectively. For superhydrophobic surfaces, contact angle is

typically greater than 150º with the small pore diameters (micro-nano structures). As the result, the water is pushed out from the superhydrophobic surfaces (h<0) [107,108].

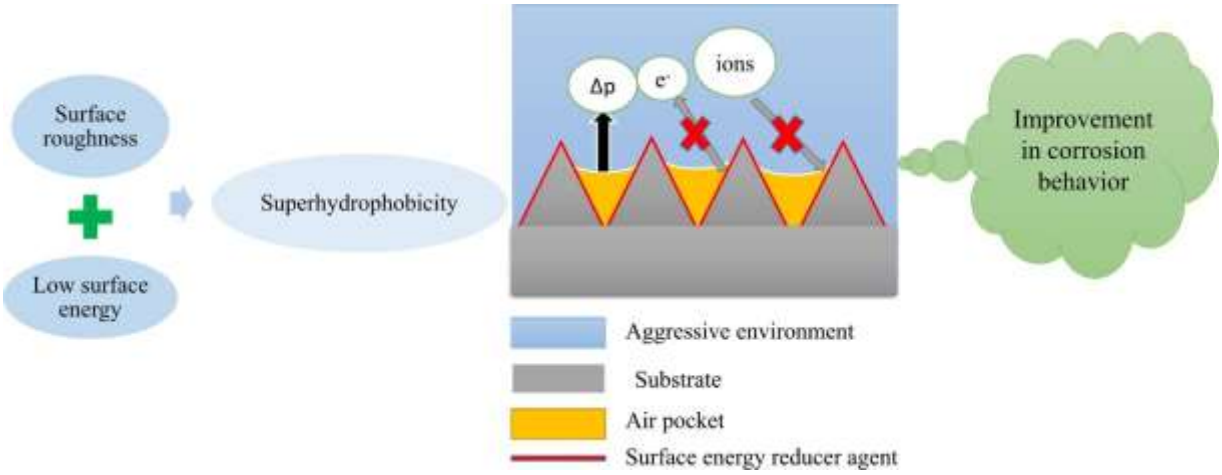

Figure 2.21. Schematic of corrosion protection from superhydrophobic coating surfaces[107].

2.6.2 Electrochemical measurements of corrosion resistance

To evaluate anticorrosion performances of superhydrophobic surfaces, various electrochemical tests such as opening circuit potential (OCP), potentiodynamic polarization and electrochemical impedance spectroscopy (EIS) are typically performed. A three-electrode electrochemical cell consisted of a working electrode, a counter electrode and a reference electrode are used in the studies. Sodium chloride solutions (3-3.5 wt. %) are used as the electrolyte solution to enhance the electrochemical responses [109,110].

In OCP test, the current responses are obtained at rest potential states. In other words, there is no current flow or any applied potential being applied to working electrode in the cell [111]. Tafel method can be employed to OCP experimental data to obtain info such as open circuit potential (E_{ocp}), polarization resistance (R_p) and corrosion current density (i_{corr}) [112]. Typically, more positive values of OCP responses indicates better performances of coatings [110].

Potentiodynamic polarization test can be setup in similar manners as OCP test; however, the external potential is applied to the cell and the responses are recorded.

In EIS study, a wide range of frequency are applied to superhydrophobic coated substrates and the impendence response are collected for evaluation [113]. This electrochemical technique allows for obtaining certain parameters related to kinetic and mechanistic of corrosion responses, which provide advantages for improving properties of coatings against corrosion [109]. To obtain EIS parameters such as capacitance and resistance of coating, two analyzing pathways can be performed. In one method, various electrical equivalent circuit models can be used to fit the experimental data [109]. The capacitance and the resistance in the circuit are varied until the data fit with the experimental data. In another method, EIS parameters can be determined by plotting bode and Nyquist plots and analyze their graphs.

2.7 Concluding Remarks and Future Outlook

Inspired by the self-cleaning and antiwetting properties of the lotus leaf and other materials found in nature, researchers and engineers have developed a variety of techniques to mimic the micro-nanostructure roughness of those surfaces. The combination of techniques for surface roughness and low surface energy materials allow superhydrophobic surfaces to be created, which open opportunities towards tremendous superhydrophobic application such as water-repellent clothing, stain-resistant textiles, self-cleaning windows, antifogging glasses and anti-corrosion paints. Engineered methods for creating surface roughness including chemical etching, lithography, electrodeposition, electrospinning, chemical vapour deposition, sol-gel process, and spray coating was discussed alongside addressing the advances and limitations of each technique. Likewise, recent breakthrough using these methods in preparing superhydrophobic surfaces were

analyzed. The modern alternatives to low surface energy materials such as fluoropolymer and silicones for superhydrophobicity with improved performances, as well as the introduction of multifunctional properties into these materials using nanoparticles such as graphene, carbon nanotubes, carbon nanofibers and specifically nanocellulose were shown to be highly effective and comparable to previously used materials.

Bio-sourced biodegradable materials such as nanocellulose encompassing CNCs and CNFs, possessing great intrinsic properties have been incorporated into preparing process of superhydrophobic coatings and aerogels. This has led to improved thermal resistance and mechanical strength of the materials and most importantly the replacement of non-renewable and sometimes toxic materials that have previously been used. Engineering surface roughness onto substrates via spray drying, dip-coating and spin-coating are prominent methods due to cost-efficiency requirement of minimal equipment, and applicable to many substrates.

The modification of nanocellulose to impart low surface energy for superhydrophobic surfaces has typically been achieved through the grafting of fluorocarbons to their surfaces, as they are well-known to produce low energy surfaces. However, environmental concerns regarding the toxicity of fluoropolymers still linger and need to be addressed. Hence, a great need for the development of alternatives to these reagents for superhydrophobic application is lacking. A trend in the development of hydrophobic and superhydrophobic surfaces is the modification of biobased materials such as nanocellulose and starch with alternative low energy substances such as fatty acids or silane agents, which are alternatives for environmental health safety and/or bio sustainable. It is anticipated that nano-cellulosic materials would become one of the next generations of nanoparticles to not only introduce roughness for superhydrophobicity but also

improve overall material properties. The future of this bio-based nanoparticles would be expected to be extended to many applications of superhydrophobicity in the near future.

Chapter 3. Cationic Surfactant Modified Cellulose Nanocrystals for Corrosion Protective Epoxy Nanocomposite Surface Coatings

3.1 Introduction

Polymeric coatings are common types of organic coatings applied to metal surfaces as a physical barrier against corrosive molecules [114–116]. However, the long term durability of these coatings is still inadequate due to their susceptibility to scratch, which leads to defects in the coating layer [117]. These defects act as pathways for corrosive substances to penetrate the coating and corrode metal substrates [118]. To tackle this problem, corrosion inhibitors such as micro- and nanoparticles are incorporated into the coating formulation to form (nano)composite coatings. For instance, graphene oxide nanomaterials have previously been incorporated in polyurethane coatings to prevent the corrosion of copper and carbon steel [119]. The results of this study showed that the coating provided a great reduction in the corrosion rate (CR) (CR of 1.81 $x10^{-5}$ mm per year) with just 1 wt. % loading of exfoliated graphene oxide [119]. Likewise, a nanocomposite of polyurethane with 4,4´-diaminodiphenylmethane modified nanoclay for stainless steel disk coating revealed one order lower in the corrosion rate as compared to pure polyurethane coating due to the enhanced dispersion of the modified nanoclays in the polyurethane matrix [120]. Polyaniline nanoparticles were also shown to improve the anticorrosion of epoxy paint coatings [121].

The anticorrosion property enhancement of nanocomposite comes from the fact that these nanoparticles are capable of filling the porosity of polymer matrices and increase the tortuosity through which the corrosive molecules have to pass to penetrate the coatings [122]. CNCs are nanorods isolated from cellulosic fibers of woods, plants, tunicates, algae and bacterial cellulose with a length ranging from 50-300 nm [123,124]. As a result of their low density, high aspect ratio, outstanding mechanical properties and biodegradability of CNCs, they have attracted substantial

attention for nanocomposite applications [2,125]. Acid hydrolysis, such as sulfuric acid, is usually employed to separate the crystal domain of cellulose from cellulosic fibers. This results in CNCs with an abundant hydroxyl groups with a small fraction of sulfate ester group on its surface [124,126]. While these surface functional groups make CNCs highly dispersible in aqueous solution, it circumvents their dispersibility in non-polar media including most polymers that are typically non-polar usually due to hydrogen bonding mediated aggregation of the CNCs.

To successfully prepare polymer nanocomposites based on CNCs for coating applications, CNCs need to be dispersed in the non-polar polymer matrices, and this could be achieved through hydrophobic modification of CNCs [89,127]. Since CNCs contain a substantial amount of -OH functional groups on their surface, it is amenable to several modification chemistries [128,129]. Synthetic methods, which rely heavily on covalent bonding, including etherification, esterification, and living polymerization, are generally more efficient in achieving the desired functional properties of CNCs [130–135]. Non-covalent surface modification techniques that include the use of surfactants and physical adsorption to tailor CNC surfaces for functional applications have been reported with some success [135]. The non-covalent modifications could be the preferred route in several cases. This is because non-covalent tailoring processes are usually less expensive, less aggressive in terms of reaction conditions, which usually maintains the nanostructure and morphology of CNCs, and such processes typically require little to no use of organic solvents [136]. The choices of surfactants for modification include non-ionic surfactants, anionic surfactants, and cationic surfactants. Among the three types, the cationic surfactants are proved to provide the best adsorption on to negative charged CNCs due to the higher magnitude of electrostatic interaction of charged ions compared to secondary interaction of non-ionic and anionic surfactants with CNCs [137]. Previous investigation has shown a successful adsorption of

cationic surfactants such as cetyltetramethylammoniumbromide (CTAB), polyethyleneimine (PEI), hexadecyltrimethylammonium (HDTMA) onto negatively charged sulfuric acid derived CNCs [123,136].

In this study, CNCs were first modified with 2,2,6,6-tetramethyl-piperidinyl-1-oxyl (TEMPO) to introduce carboxylic groups (COO^-), which increased the negative charges on the surface of the CNCs. The carboxylated CNCs were then decorated with three different types of cationic surfactants via electrostatic adsorption. The selected surfactants were cetyltetramethylammoniumbromide (CTAB, C16 single chain), dimethyldidodecylammonium bromide (DDAB**,** C12 double chains**),** and dimethyldihexadecylammonium **(**DHAB, C12 double chains) with chemical structures shown in **Figure 3.1**. The selected surfactants differ from each other in terms of chain length and numbers of tails, and this is expected to affect their adsorption on the carboxylated CNCs. It was hypothesized that through the adsorption of the surfactants, the CNCs will be more hydrophobic and compatible with non-polar polymers. To the best of our knowledge, no studies have been conducted to determine the effect of surfactant modified CNCs on coating applications. In this work, the modified CNCs were incorporated into epoxy resins to produce nanocomposite coatings. These formulations were then used to coat mild steel, and the anticorrosion properties of these nanocomposite coatings were explored in detail.

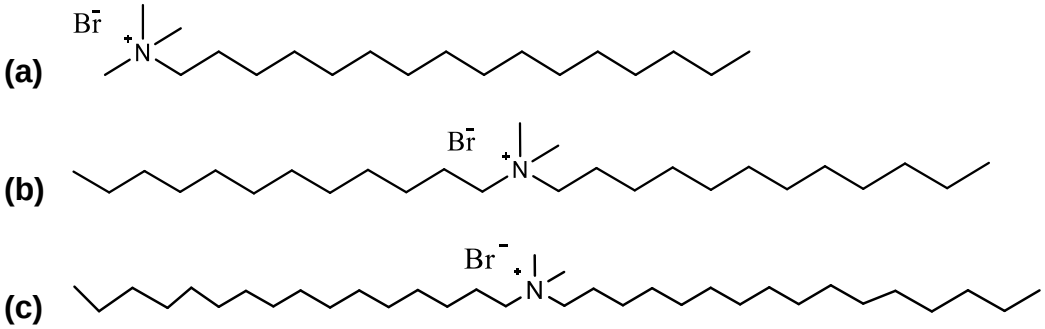

Figure 3.1. Molecular structures of cationic surfactants (a) CTAB (b) DDAB and (c) DHAB.

3.2 Experimental Section

3.2.1 Materials

Dried CNC powder was provided by CelluForce Inc. (Montreal, Canada). The CNC powder contains about 0.87% sulfur stemming from the acid hydrolysis process. 2,2,6,6-Tetramethyl-1-piperidinyloxy (TEMPO, 98%), sodium hypochlorite (NaClO, 10-14% W/W), sodium hydroxide (NaOH, ≥ 97%), dimethyldidodecylammonium bromide (DDAB, 98%), dimethyldihexadecylammonium bromide (DHAB, 97%), epoxy resin (Araldite 506, epoxide equivalent weight 172 – 185 Da) and amine curing agent poly(propylene glycol) bis (2-aminopropyl ether) were purchased from Sigma-Aldrich Corporation (Missouri, USA). Sodium bromide (NaBr, 99+ %) and hexadecyltrimethylammonium bromide (CTAB, 98%) were obtained from Fisher Scientific Company (New Hampshire, USA). Carbon steel panels (Q panel R46) were obtained from Q-Lab Corporation (OH, USA). All chemical products were used as received without any modifications.

3.2.2 Modification of Cellulose Nanocrystals

Cationic surfactant modification of CNCs was conducted through a three-step process. In the first step, the hydroxyl moiety of CNCs was oxidized generating carboxylic functional group through TEMPO mediated oxidation. TEMPO oxidation was performed based on the method described by Saito *et al* [138]. Firstly, 3 wt.% of dried CNC powder was dispersed in deionized (DI) water and homogenized (25,000 rpm, PowerGen 700 Homogenizer) until a uniform gel dispersion was obtained. TEMPO (0.18 g) and NaBr (1.2 g) were added into the prepared dispersion and stirred at 500 rpm for 5 min using a magnetic stir bar. NaClO (8.6 g) was then slowly added into the dispersion over a 30 min period and the pH was adjusted to 10 using NaOH (1 M). The reaction completed point was when the pH of the dispersion solution reached 10 and it

stabilized at this pH 10. Thereafter, the dispersion was neutralized using HCl (1 M) to prevent any degradation from the basic solution. The dispersion was centrifuged (Heraeus Megafuge Centrifuge, Thermo Fisher Scientific) at 4000 rpm for 10 min to concentrate and separate the oxidized CNCs (oCNC) from the supernatant. The gel-like product was then washed and centrifuged three times with DI water to remove any side or un-reacted products. The final product was stored in a fridge at 4 ^{o}C for further modification. In the second step, the pH of the oCNC gel dispersion obtained in the first step was re-adjusted to pH 10 using 1 M of NaOH to form a basic dispersion of oCNC. The pH change converted the oCNC (COOH) to oCNC (COO^-) form. In the final step, surfactant modification of CNC was conducted through the adsorption of cationic surfactants onto the negatively charged surface of oCNC. For this, solutions containing 1 wt.% of each surfactant (CTAB, DDAB and DHAB) was prepared and placed in individual beakers. These beakers were stirred and heated to 60 ^{o}C to ensure complete solubilization of DDAB and DHAB as they are insoluble in aqueous solution at room temperature. CTAB was also treated the same for comparison purposes. The basic oCNC (0.7 g solid content) dispersion was then added slowly to each surfactant solution (30 mL, 1 wt.%) at 60 ^{o}C for 2 hunder continuous stirring. After that, the solutions were centrifuged at 4000 rpm for 10 min, and the supernatant was decanted. The final products were repeatedly washed with DI water (three cycles of redispersion and centrifugation) and stored at 4 ^{o}C.

3.2.3 Characterization of surfactant modified CNCs

3.2.3.1 Morphology of modified CNCs

The morphology of modified CNCs compared to unmodified CNCs were acquired via Transmission electron microscopy (TEM) (Philips, CM 10). The THF dispersible modified CNCs

and native CNCs (0.3 wt.%) were stained with uranyl acetate before casting on TEM carbon-coated copper grid for analysis.

3.2.3.2 Fourier transform infrared (FTIR) spectroscopy

IR Spectra of native CNC, oCNC, CTAB-oCNC, DDAB-oCNC and DHAB-oCNC were obtained from Attenuated Total Reflectance (ATR) – FTIR (ATR-FTIR Nicolet 6700, Thermo Scientific Inc). IR samples were prepared by mixing dried powder of potassium bromide (KBr, 200 mg) and dried native and modified CNC samples (5mg). The mixed samples were first ground using a mortar and pestle and pressed into pellets for FTIR analysis. The measurements were collected between 500 and 4000 cm^{-1} using transmittance mode and at 32 scans.

3.2.3.3 Elemental analysis

The elemental analysis of native and surfactant modified CNCs (CTAB-oCNC, DDAB-oCNC, and DHAB-oCNC) were obtained using a 4010 Elemental Analyzer (Costech Instrument, Italy). The carbon and nitrogen contents were calculated, and the average and standard deviation results are reported.

3.2.3.4 X- ray diffraction (XRD)

The crystallinity profiles of native CNC, CTAB-oCNC, DDAB-oCNC, and DHAB-oCNC were acquired using X-ray diffractometer D8 Discover (Bruker, Kaelsruhe, Germany) with a Cu-Kα as the radiation source. The diffraction angles (2θ) were recorded between 5 to 40 ^{o} with parameter setting of 40 kV, 40 mA, and 0.02 step size.

3.2.3.5 Thermogravimetric analysis (TGA)

The thermal stability of the surfactant modified CNCs compared to the native CNC was analyzed using Thermogravimetric analysis (TGA 500, TA Instrument). The temperature scan

range was from 100 to 600 ^{o} C with a ramp rate of 5 ^{o}C/min under nitrogen flow. The effect of the surfactant modifications was analyzed by evaluating the degradation temperature and weight loss on the TGA thermograms.

3.2.3.6 Dispersibility and compatibility of modified CNCs in different solvents

The change in polarity of the modified CNCs was evaluated from the nanoparticle dispersibility in water (polar solvent) and tetrahydrofuran (THF) (aprotic solvent). For this, about 1 wt.% of CNCs and modified CNCs were directly dispersed in water and THF solvent while visually observing the dispersions over time. The particle size of the native and the surfactant modified CNCs in water and THF solutions were obtained using a particle size analyzer (Brookhaven instrument, New York, USA). Additionally, samples (0.3 wt.%) were dispersed in water and THF, homogenized for 2 min, and then sonicated using a probe sonicator (sonic dimembrator model 120, Fisher Scientific Inc.) for an additional 2 min to further aid the dispersion of the particles in the solvents. It is important to highlight here that this instrument provides particle size based on spherical particle geometry (hydrodynamic radius). Thus, the obtained values c were not the actual particle sizes of the CNC but they are good indicators of dispersibility/compatibility with different polarity solvents [139]. Smaller particle sizes were considered here as good indicators of dispersibility and therefore improved compatibility with the solvent.

3.2.3.7 Water contact angle measurements

The water contact angle (WCA) of native and surfactant modified CNCs were obtained from a custom-built optical sessile drop system. Dried powder samples were first dispersed in toluene and sonicated for 30 min before casting on glass slides. Three repeated castings were performed to ensure that the materials fully covered the slides for analysis. A droplet of DI water

(30 µL at 23 ^{o}C) was then allowed to drop on the coated surface, and images were taken at the instant the droplet contacted the sample surface. ImageJ software was used to measure the WCA of the samples.

3.2.3.8 Zeta potential measurements

The zeta potential of native and the three surfactant-modified CNC samples (CTAB-oCNC, DDAB-oCNC and DHAB-oCNC) were measured using a Malvern Zetasizer (Westborough, MA). The samples (0.1 wt.%) were first dispersed in DI water and homogenized for 2 min followed by sonication for 2 more min. A folded capillary cell (Zetasizer nanoseries, DTS 1061) was used as a measuring cell. Three consecutive measurements were taken for each sample solution at 25 ^{o}C, and the average zeta potential was reported.

3.2.4 Fabrication of epoxy/CNC nanocomposite coatings

Native CNC and surfactant modified CNCs (CTAB-oCNC, DDAB-oCNC, DHAB-oCNC) were incorporated into the epoxy resin at 5 wt.% loading. For this, water dispersed CNC samples were solvent exchanged with acetone (repeated washing and centrifugation) to remove traces of water, after which they were added into the epoxy resin and homogenized (2 min) and sonicated (2 min). Amine curing agent was then added to each dispersion (epoxy/amine curing agent ratio of 7:3), stirred continuously for 5 min and degassed in a vacuum oven at 60 ^{o}C until no bubble was noticed. A doctor blade film applicator that provides 200 µm thickness (Yuchengtech, China) was used to coat the nanocomposite formulations onto the carbon steel panels (Q panel R46, Q-Lab Corporation). The composite coatings on the steel were cured and conditioned at room temperature and relative humidity of about 50% for 7 days. The neat epoxy coating formulation and application was prepared in a similar fashion for comparison.

3.2.5 Nanocomposite characterizations

3.2.5.1 Morphology studies of nanocomposites

The morphology of the nanocomposites and dispersibility of the native and surfactant modified CNC particles in the epoxy matrix were evaluated using Scanning Electron Microscopy (SEM) instrument (Zeiss Leo, 1530). Nanocomposite sample specimens for SEM studies were obtained by coating a thin film of the prepared formulation on a Teflon sheet. The cured films were removed from the Teflon sheet and gold-coated (~10nm) using a gold sputter coater, and SEM images were collected. Transmission electron microscopy (TEM) (Philips, CM 10) was utilized to study the dispersibility of native and modified CNC nanoparticles in the epoxy matrix. Microtoming was employed to prepare thin films (50nm) for TEM analysis.

3.2.5.2 Salt spray test

The corrosion performance of the neat epoxy control, epoxy/CNC, and epoxy/surfactant modified CNC nanocomposites were analyzed using a neutral salt spray method. The specimens were prepared according to ASTM B117 standard with some modifications. In this test, manual spraying of sodium chloride (5 wt. %) solutions was employed instead of the automatic spraying from a test chamber as outlined in the ASTM B117. All experiments were performed at room temperature. Before the test, the coated steel plates were scratched to obtain a uniform dimension letter “x” using a sharp knife. The scratched plates were then sprayed with the salt solution every 2 h for the first 10 h, and every 24 h afterward for a total of 15 days. A digital camera was used to collect images of corrosion progress around the scratch area.

3.2.5.3 Electrochemistry study of corrosion progress

To verify the anticorrosion performance of the nanocomposite coatings, an open circuit potential (OCP) and potentiodynamic polarization scan electrochemical test were conducted on

the coated steel plates. A three-electrode chemical system was used in all the electrochemical studies. Steel plates with 1 cm x 1 cm surface area were used as the working electrode while an Ag/AgCl electrode was used as a reference electrode along with a platinum wire as the counter electrode. Both OCP and potentiodynamic polarization tests were performed at room temperature in a neutral solution of sodium chloride (3 wt. %). For the OCP test, the three electrodes were first submerged in the test solution, and the electrochemical corrosion potentials were recorded after 2 h. A potential of -2.5 to 2.5 V was then applied to the solution and potentiodynamic polarization curves were acquired.

3.2.6 Statistical analysis

The experimental data were analyzed using the statistical software package Minitab (Version 18). Single factor analysis of variance (ANOVA) was employed to identify significant differences among mean values with a 95% confidence level ($P < 0.05$) of LSD criteria. Factor used was the type of surfactant.

3.3 Results and discussions

3.3.1 Surface modification of CNCs with surfactants

The proposed hydrophobic modification of the surface of CNCs occurred in three steps as illustrated in **Figure 3.2**. First, the TEMPO mediated oxidation method was employed to convert the hydroxyl functional groups of CNCs to a carboxylic acid. This method introduced the carboxylic group onto the position C6 (primary –OH) of the anhydroglucose monomer unit of the CNCs[138]. Through deprotonation with a basic solution, such functional groups were transformed from -COOH to COO^- group. Finally, the produced COO^- groups acted as the main site for the cationic surfactant adsorption via an electrostatic interaction [140]. To validate these

reactions, IR and elemental analysis were conducted on the native and modified CNC samples and results are presented below.

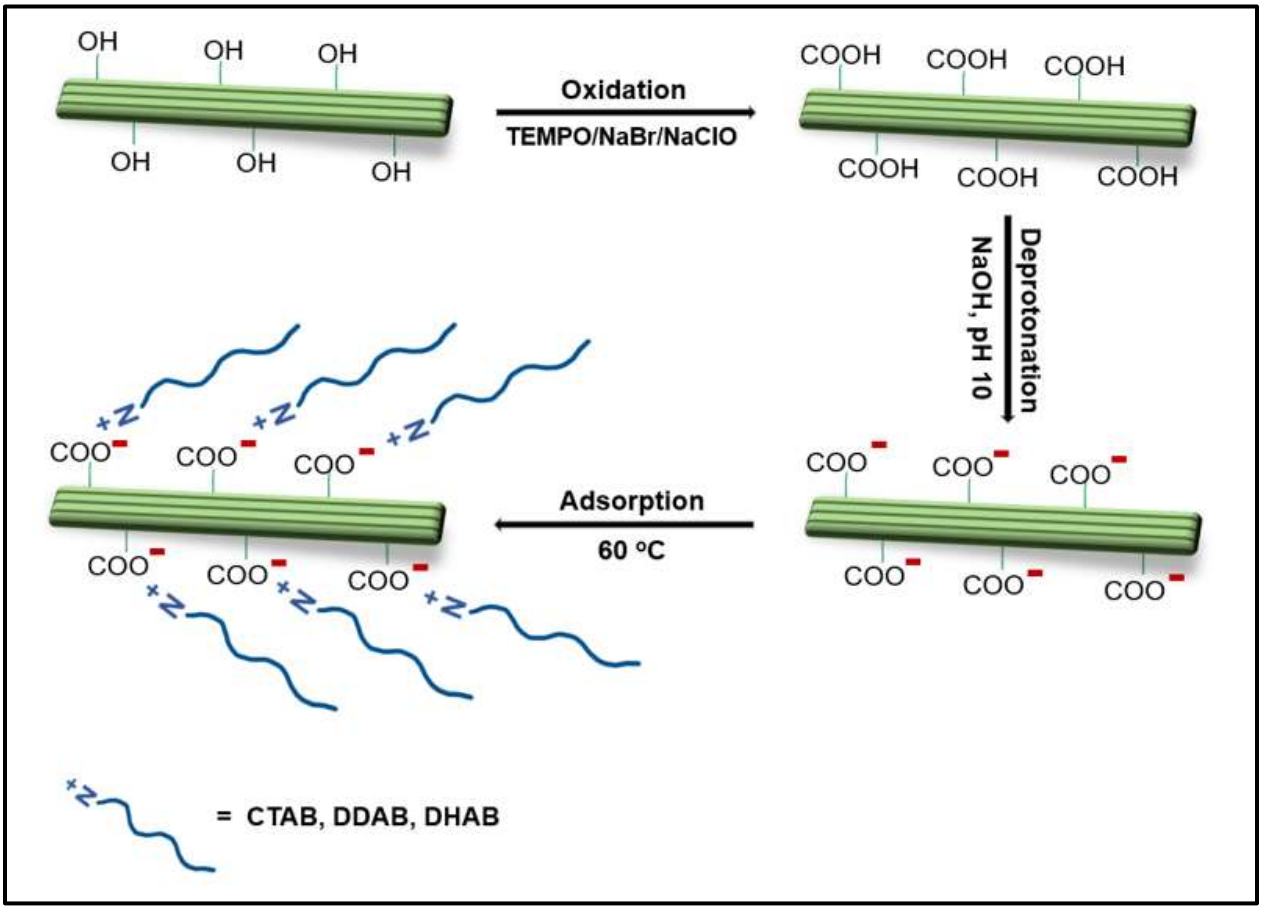

Figure 3.2. Schematic representation of surfactant modification of CNCs using a three-step process.

3.3.2 Morphology of surfactant modified CNCs

Figure 3.3 show the morphology comparison of native CNC with the three different surfactant modified CNC. Native CNC has similar morphology to CNC reported in literature [141,142]. From the images, it can be seen that all surfactant modified CNC (**Figure 3.3b-d**) are surrounded by black shadow, which could be from the orientation of surfactant chains used in the modification. The chosen surfactant contains nitrogen, which is a heavier element compared to the

carbon of CNCs. This induces the mass density contrast on TEM images since the electron beam is not passing easily through molecules and they scatter more electrons compared to CNC nanorods. It is noticeable that all surfactant modified CNC show less aggregated and more dispersed than unmodified CNCs with DDAB-oCNC (**Figure 3.3c**) show the best dispersion.

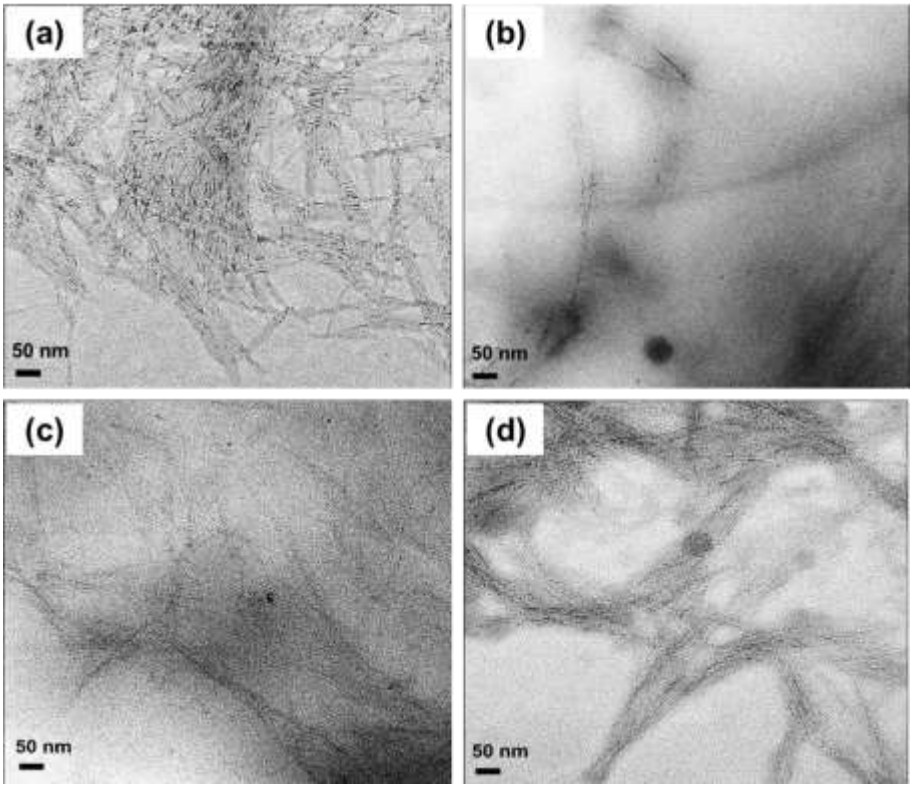

Figure 3.3. TEM images of (a) native CNCs, (b) CTAB-oCNC, (c) DDAB-oCNC and (d) DHAB-oCNC

3.3.3 Fourier transform infrared spectroscopy (FTIR)

FTIR was used to characterize the chemical structure changes of the CNCs as a result of the modifications. **Figure 3.4** illustrated the IR signals of CNC and the modified CNCs (oCNC, CTAB-oCNC, DDAB-oCNC and DHAB-oCNC). The IR spectra of pristine CNC agreed with other studies, showing distinct peaks at 3450 cm^{-1}, 2920 cm^{-1} associated with the O-H and C-H stretch of CNCs, respectively [143–145]. The spectra of the oCNC sample exhibited a peak at 1730 cm^{-1} (C=O stretch of COOH) and a broadening of the peak at 3450 cm^{-1} (O-H stretch), which

confirmed the conversion of hydroxyl group of CNC to carboxylic group of CNC [146,147]. The peak at 1640 cm^{-1} in all samples were attributed to an O-H bending vibration due to the adsorbed water [145,148]. It was noticed that all the surfactant modified CNCs (CTAB-oCNC, DDAB-oCNC and DHAB-oCNC) displayed similar peak characteristics due to the nature of C-H bonding of the surfactant molecules. All three surfactant modified samples contained a double peak at 2850 and 2915 cm^{-1}, which corresponded to the symmetric and asymmetric stretch of C-H bond of the surfactant alkyl chain [136,140]. In comparison to an oxidized CNC sample (oCNC), the peak of the surfactant modified samples at 1730 cm^{-1} has shifted to 1610 cm^{-1} that was likely stemming from the stretching interaction of the surfactant-carboxylate complex between COO^- and NH_3^+[149]. The IR results confirmed that the three cationic surfactants were successfully attached to the surface of CNCs.

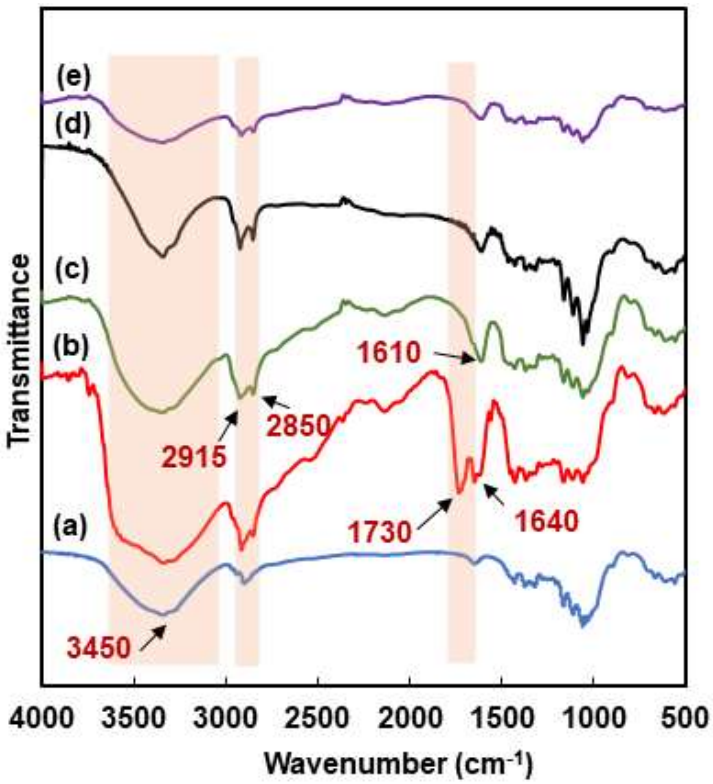

Figure 3.4. FTIR of (a) native CNC (b) acidified oCNC (c) CTAB-oCNC (d) DDAB-oCNC and (e) DHAB-oCNC.

3.3.4 Elemental analysis

Elemental analysis was performed to determine the amount of surfactant adsorbed onto the oCNC. **Table 3.1** depicts the summary of carbon and nitrogen content of CNC, oCNC, CTAB-oCNC, DDAB-oCNC and DHAB-oCNC from the elemental analysis. No nitrogen content was found in the CNC and oCNC samples as expected considering that both samples do not contain any elemental nitrogen in their chemical structures. The oCNC sample had about 4% less carbon compared to CNC, which was similar to previous studies by Wang *et al* (2017) [150] and this could indicate that there was a slight fragmentation of CNC structure during the TEMPO oxidation. In all the surfactant modified CNCs, the carbon contents had increased by about 14-15%, which were attributed to the carbon element of the long alkyl chain of the surfactant molecules [140]. The nitrogen contents (about 1%) were also observed in surfactant modified CNCs resulting from the ammonium head group of the surfactants. Since the nitrogen content is proportional to the concentration of surfactant, it can be assumed that all three different surfactants (CTAB, DDAB, DHAB) adsorb roughly equal onto oCNC, and the amount of surface charged oCNC was the factor controlling the surfactant adsorption. The elemental analysis clearly corroborated with the IR result and confirmed the surface modification of the CNCs via the surfactants.

Table 3.1. The elemental analysis of native CNC and three different cationic surfactant modified CNCs.

Sample	Total carbon (%)	Total Nitrogen (%)
CNC	44.98 ± 0.86^{a}	0
oCNC	39.89 ± 0.71^{b}	0
CTAB-oCNC	54.02 ± 1.20^{c}	1.08 ± 0.03^{a}
DDAB-oCNC	55.47 ± 2.20^{c}	0.95 ± 0.04^{b}

DHAB-oCNC	54.86± 1.10^{c}	0.81 ± 0.03^{c}

Value – mean ± standard deviation (n = 3), means with the same superscript letters within a column are not significantly different at the $P < 0.05$ level.

3.3.5 X-ray diffraction (XRD)

XRD analysis was used to evaluate the crystalline profile of the modified CNCs after the TEMPO oxidation and surfactant adsorption reaction. **Figure 3.5** showed the XRD diffraction patterns of CNCs and the modified CNCs. CNCs have diffraction peaks at 15.1º, 16.7º , 22.6º, and 34.2º which corresponded to $\overline{110}$, 110, 200, and 004 planes of the cellulose I crystal structure, respectively[143,151]. For the oCNC (**Figure 3.5a**), the peak at 200 diffracts at the same position as the CNC with a slight reduction in peak intensity while the 100 and 004 peaks were shifted to smaller diffraction angles at 12.3º and 26.2º, respectively. The oxidation reaction might have slightly penetrated the CNC crystal structure in addition to oxidizing the hydroxyl groups on the surface resulting in an increase in the d spacing along the 110 and 004 planes and hence lower 2θ [152]. Another explanation could be that the cellulose I crystals were dissolved and recrystallized to cellulose II crystal structure during and after the reaction, respectively [153,154]. However, the reaction conditions employed in this work were fairly mild to cause crystal dissolution.

All three surfactant-modified CNC samples (**Figure 3.5c-e)** exhibited similar crystal shape and peak position as that of the oCNC. It was interesting to note that the intensity of the peak at 200 reduced significantly, which could be because of the addition of the cationic surfactant chains. Surfactants work as capping agents along the crystal planes of oCNC leading to smaller particles, which ineffectively diffract X-ray beams [155]. The increase in the 004 plane peak of DHAB-oCNC (**Figure 3.5e)** might be from the crystal structure of DHAB that has a similar plane profile as the CNCs**.** In summary, the surfactant modified CNCs maintained their high crystallinity and the apparent weakening of the XRD signals were attributed to the masking effect of the surfactants.

Thus, the modified CNC can still be used as a structural reinforcing additive in epoxy or other polymer nanocomposites.

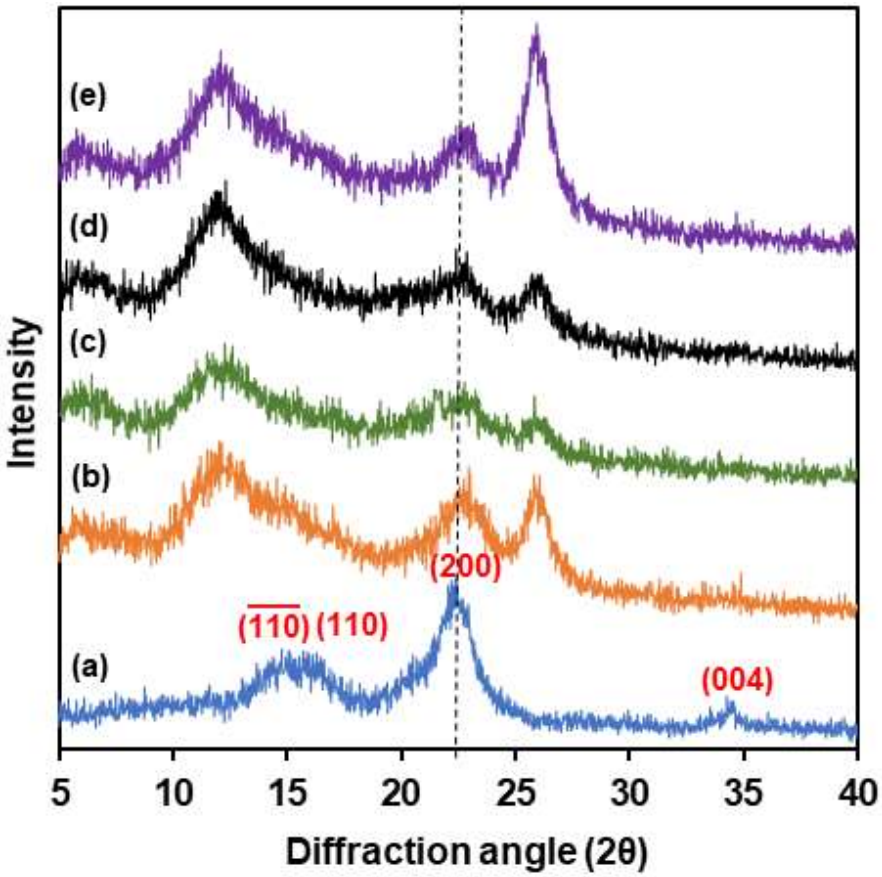

Figure 3.5. X ray diffraction of (a) native CNC, (b) oCNC (c) CTAB-oCNC (d) DDAB-oCNC and (e) DHAB-oCNC.

3.3.6 Thermogravimetric (TGA) analysis

It is crucial to understand the influence of the modifications on the thermal stability of CNCs as a reinforcing filler. This is because the fabrication of composites such as the curing of epoxy or the melt processing of thermoplastic polymer composites typically took place at elevated temperatures and the stability of fillers at such temperatures is a necessity. TGA was employed to obtain the thermal degradation profile of the native and the surfactant modified CNCs, and results are presented in **Figure 3.6** (**a-b).** The native CNC sample showed a peak weight loss at 312 ^{o}C, which was mainly from the depolymerization of its backbone chains into volatile compounds

[143]. The oCNC sample showed an early onset (212 ^{o}C) compared to CNC (290 ^{o}C), which could be stemming from the thermal cleavage of highly accessible –COOH functional groups on the oCNC as compared to the –OH of CNC [149]. For surfactant modified CNCs, two prominent weight loss peaks were observed around 245-260 and 325 ^{o}C irrespective of the type of surfactant used. While the first peak was associated with the degradation of the surfactant chains and carboxylic groups of CNCs [156], the second degradation peak could be affiliated with the CNC crystal structure dissociation [143]. Pure CTAB and DDAB have onset degradation temperatures at 249.9 and 213.4 ^{o}C, respectively [157]. It was interesting to notice that the degradation of the first peaks of surfactant modified CNC was clearly defined and improved, as opposed to the oCNC degradation. The improvement could be from the decrease in acidity (less carboxylic group) in response to the stabilization effect of the surfactant molecules on the CNC surfaces [158]. Among the three modified samples, the DDAB-oCNC and DHAB-oCNC displayed a slight improvement in their thermal stability as evidenced by the increased peak degradation temperature. Overall, the surfactant modified CNCs were stable at temperatures as high as 200 ^{o}C. This makes them suitable to be used in several polymers (including epoxy) that require lower processing temperatures.

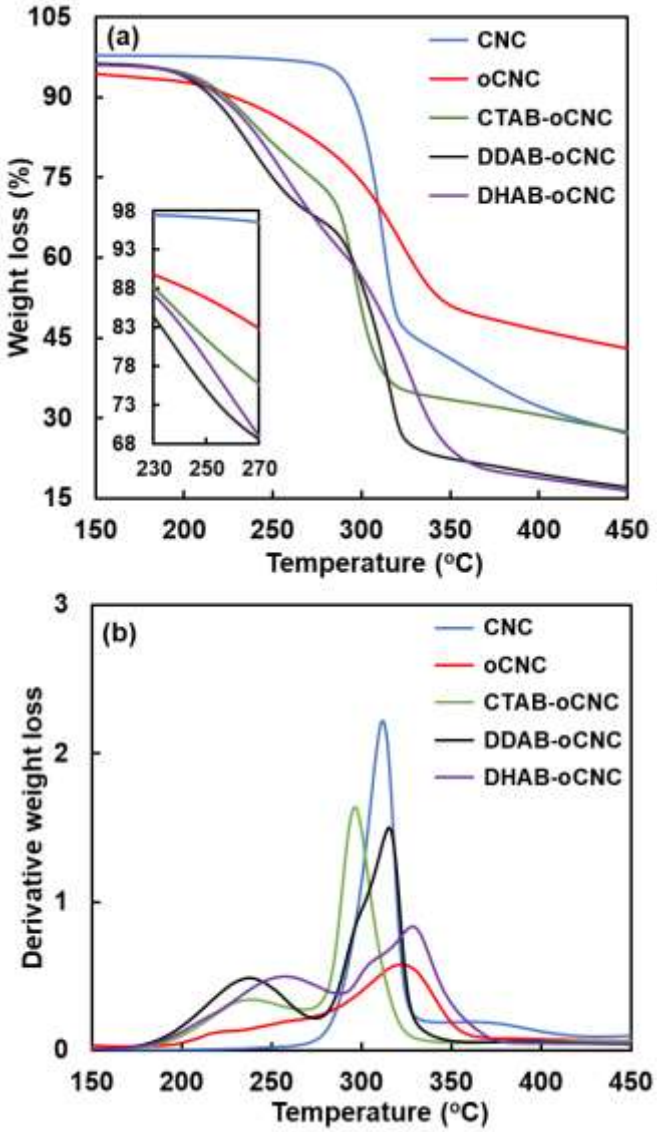

Figure 3.6. TGA of (a) weight % and (b) derivative weight percent of native CNC, oCNC and three different cationic surfactant modified CNC (CTAB-oCNC, DDAB-oCNC, DHAB-oCNC).

3.3.7 Dispersibility and compatibility of modified CNCs in different Solvent

The change in the polarity of CNC as a result of the surfactant modifications was evaluated by studying its dispersibility in water and THF before and after each modification. Water and THF with dielectric constants of 80.1 and 7.56, respectively were selected as dispersing solvents because of the wide gap in their polarity. Images presented in **Figure 3.7** showed the variation in the dispersibility of native and modified CNCs in water and THF solvents. Native CNCs (**Figure 3.7a)** formed a uniform and stable suspension in water as observed from the clarity of the solution.

This was because of the sulfate half-ester groups (sulfur content is 0.81 g/100 g CNC that is approximately 0.45 charges/nm^2) [90] existing on the structure of native CNCs accrued from the sulfuric acid hydrolysis based production process of CNCs in addition to the –OH moieties. However, the surfactant modified CNCs displayed some aggregation in water (**Figure 3.7b-d**) as noted form the turbid suspensions. This was due to the hydrophobicity of the modified CNCs associated with the aliphatic hydrocarbon chains of the adhered surfactant. The inverse results were noticed when the samples were dispersed in THF. All three surfactant-modified CNCs exhibited a fairly uniform and stable dispersibility in THF contrary to native CNC, which displayed poor dispersibility in THF. The findings here were in agreement with a previous study reported by Kaboorani *et al* [136]. In their study, the modification of CNCs with Hexadecyltrimethylammonium bromide (HDTMA) surfactant led to hydrophobic CNCs with good dispersibility in THF. It should be noted that the CTAB-oCNC and DDAB-oCNC remained fairly stable in THF solution after 24 h while DHAB-oCNC shows evidence of particle sedimentation. It is suspected that the sedimentation was probably due to the higher probability of aggregation of longer double chain lengths, compared to DDAB and CTAB surfactant molecules.

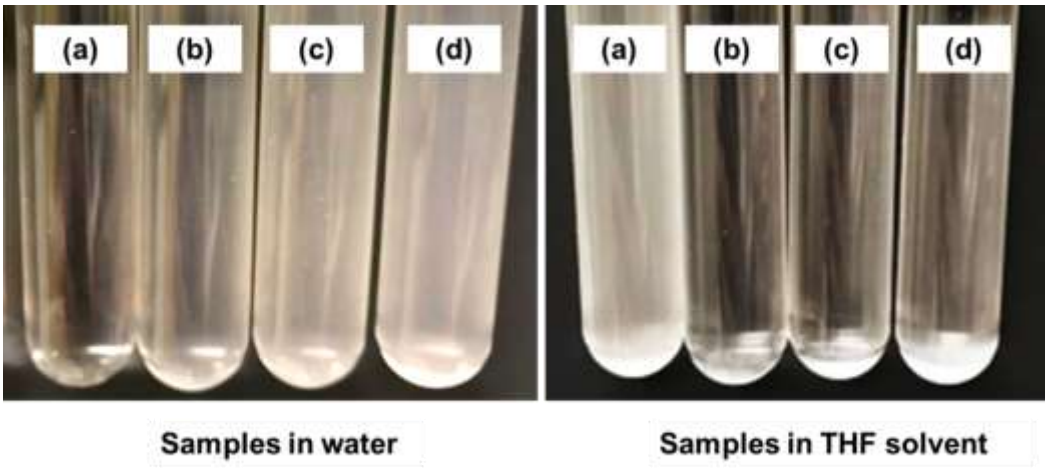

Figure 3.7. The dispersibility of (a) native CNC, (b) CTAB-oCNC, (c) DDAB-oCNC and (d) DHAB-oCNC in water and THF solvent.

Figure 3.8 presented the particle size of native and surfactant modified CNCs. The particle size analysis was carried out to validate the dispersion quality of the samples in the two solvents (water and THF) selected here. As expected, CNC exhibited the smallest particle size (average hydrodynamic diameter 250 nm) in water, confirming the excellent and individualized dispersion of native CNCs. On the contrary, the surfactant modified CNCs displayed aggregation as noted from the large average particle size (>1450 nm) measurement. Among the various surfactants, the DDAB modified CNC (DDAB-oCNC) sample exhibited the largest average particle size (~ 2.5 μm). This indicated that the DDAB modification created the most hydrophobic CNCs. It was reported in a previous study that double-tailed surfactants (DDAB) adsorbed better onto oxidized cellulose microfibrils than single tailed surfactant (CTAB) at low concentration; however, DHAB exhibited lower adsorption due to perhaps its poorer solubility in water during the modification process as compared to CTAB and DDAB [140].

The results here demonstrated that the surfactant modification had significantly changed the polarity of CNCs. Similarly, the modified CNCs had significantly smaller particle size as compared to native CNCs when dispersed in THF. The dispersibility tests and particle size analysis provided further confirmation of the successful conversion of the hydrophilic CNCs into a comparatively hydrophobic CNC via the cationic surfactant modification.

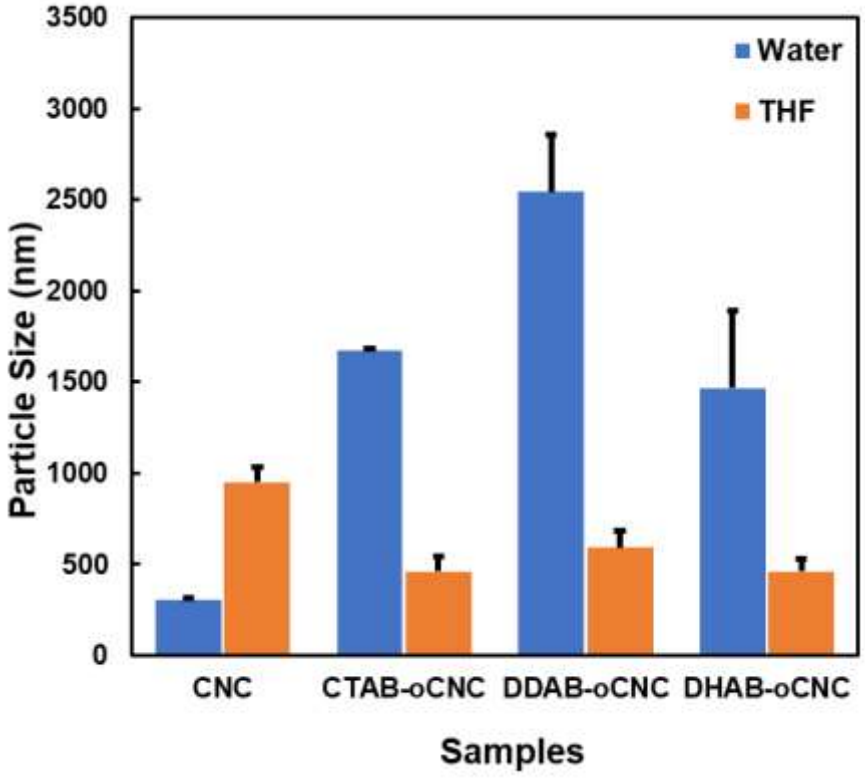

Figure 3.8. The particle size analysis of native CNC and three modified surfactant CNC dispersed in water and THF solvent.

3.3.8 Water contact angle measurements

Water contact angle is an important quantitative evaluation technique to evaluate the hydrophobicity of materials. In **Figure 3.9**, comparative images and contact angles of water droplets on sample surfaces of native and modified CNCs are presented. It was observed that all three different types of surfactant modified CNCs has higher WCA (47.9- 56.6^{o}) compared to native CNC (25.6^{o}). As mentioned in the previous sections, CNCs are very hydrophilic due to the abundant hydroxyl groups on their surface that associate with water molecules leading to hydrophilicity. The improvement in WCA in the modified samples can be attributed to the nature of surfactants used in the CNC modification. All three surfactant (CTAB, DDAB, DHAB) contains alkyl chains, which are able to orient their hydrophobic tails around the CNC surfaces leading to hydrophobicity. This appearance of surfactant surrounding CNC was confirmed by TEM analysis,

as shown in Figure 3. Salajkova *et al* reported a similar observation when they modified CNCs with quaternary ammonium salt bearing C18 alkyl chain. The WCA was found to be 48^{o} with water as the final washing step while 71^{o} was obtained with toluene washing [147]. In summary, the surfactant modified CNCs were less dispersible in water and relatively more hydrophobic than native CNCs.

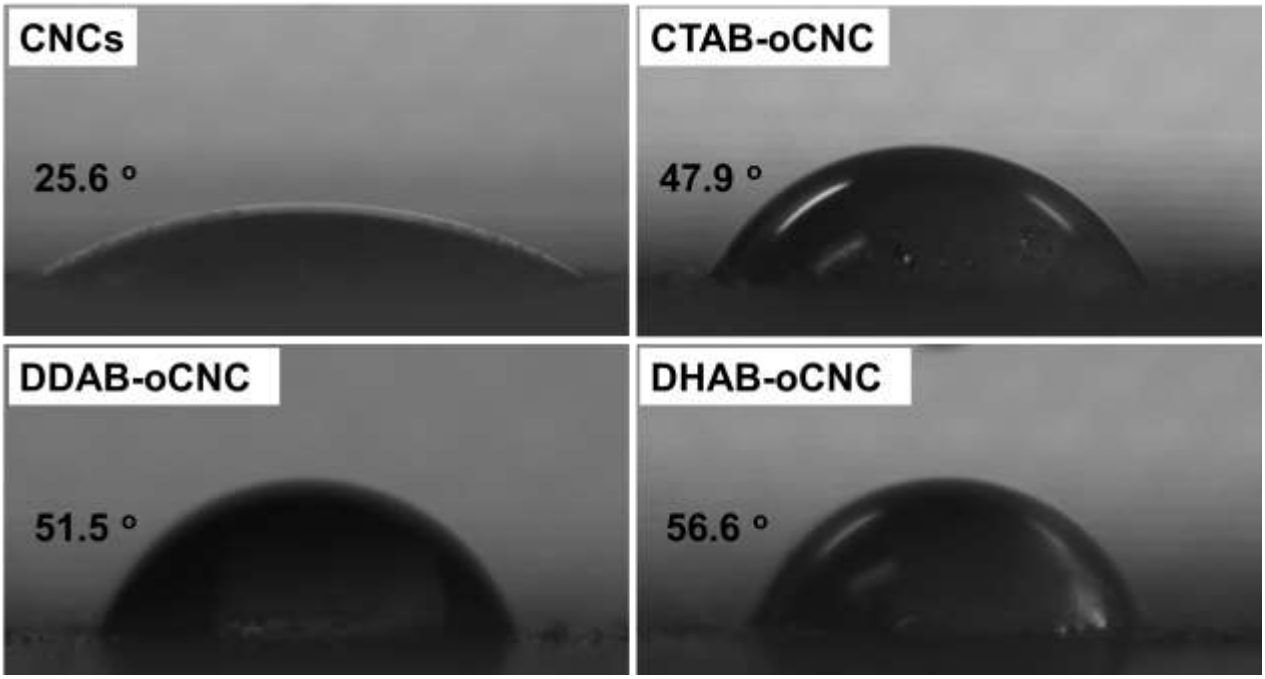

Figure 3.9. Images of water droplet on sample surfaces.

3.3.9 Zeta potential measurements

Zeta-potential is an extrinsic property defined as the value of the electrostatic potential on the imaginary slipping plane (also termed the surface of hydrodynamic shear), which is the surface where particles interact with one another or with other surfaces [159,160]. The colloidal stability, dissolution rate, aggregation, etc. of particles are affected zeta potential in addition to other extrinsic factors. Zeta potential measurement was employed here to explain the surface property changes of CNCs with the cationic surfactant modifications and to better understand the interaction

between polymer matrices and CNC particles modified as such. Herein, the zeta potential of the native and modified CNCs was measured in aqueous solutions and results are summarized in **Figure 3.10**. The zeta potential for the native CNC was -34.4 mV, which was similar to previous studies[161]. The negative charge of CNCs was accrued from the sulfate functional group introduced during the acid hydrolysis of the cellulosic fibers, and this improved its hydrophilicity and good dispersion in aqueous solution.[162] The zeta potential of oCNC (neutral pH) did not exhibit a significant difference from the CNC. Upon the modification, the zeta potential of the three surfactant-modified CNCs became less negatively charged. CTAB-oCNC, DDAB-oCNC and DHAB-oCNC provided zeta potential of -26.93, -3.1, and -15.1 mV, respectively. The observed change in the surface charge was attributed to the charge neutralization of the surfactant molecules [163]. With a decrease in electrical surface charges of the particles, electrostatic repulsion among the particles was suppressed, which resulted in the observed aggregation of the modified CNCs in water. Based on the zeta potential analysis DDAB-oCNC provided a surface charge that is close to zero (neutrality), which explained its' substantial aggregation in water that was noted from the particle size measurement (**Figure 3.8**).

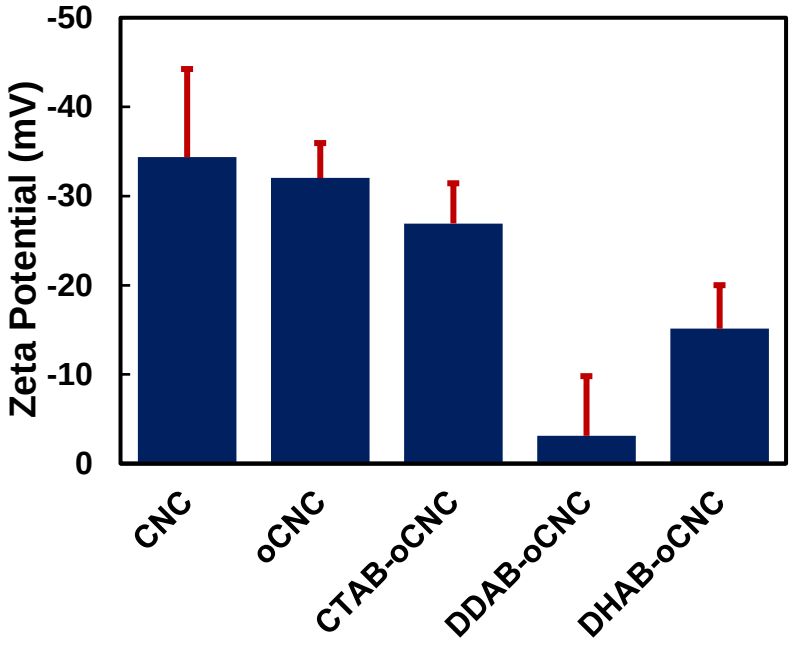

Figure 3.10. The comparison of zeta potential of native CNC, oCNC and three surfactant modified CNC.

3.3.10 Epoxy/CNC nanocomposite coatings

3.3.10.1 Morphologies of nanocomposites

The dispersibility of native and surfactant- modified CNCs in epoxy nanocomposites was investigated using SEM and the results are shown in **Figure 3.11**. The unfilled neat epoxy (**Figure 3.11a**) revealed a uniform and smooth surface, similar to previous studies [164]. The epoxy/CNC composites (**Figure 3.11b)** displayed evidence of aggregate and possibly agglomerate (aggregate of aggregate) formation with an estimated particle size of 4-5 µm. The hydroxyl groups of CNCs interact with each other to form the observed aggregates, especially in the presence of non-polar matrix such as epoxy [165]. The SEM images of the surfactant-modified CNCs (**Figure 3.11c-e**) depict better dispersion in the epoxy matrix, as observed from the smaller aggregate particles. The good dispersion of modified CNCs was mainly attributed to two factors: (1) the improved polarity match or compatibility between the polymer and modified nanoparticles and, (2) the improved interfacial interaction between the alkyl chain of the surfactant and the epoxy matrix.

Among the three nanocomposites containing the modified CNC, DDAB-oCNC (**Figure 3.11d)** demonstrated the most improved dispersion in the epoxy with an average particle size below 250 nm. This dispersibility investigation was confirmed by TEM imaging as shown in **Figure 3.12**. When DDAB-oCNC particles (**Figure 3.12b**) were dispersed in the epoxy, smaller and less aggregated particles were observed as compared to the larger aggregates detected in the native CNCs (**Figure 3.12a**). In the native CNC based composites, a poor interfacial interaction that resulted in the formation of air pockets was noted. Contrarily, the DDAB – oCNC displayed excellent interfacial interaction with no observation of air pockets. The good dispersion of DDAB-oCNC in the epoxy system was associated with the substantial change in the polarity and surface charge as noted from the solvent dispersibility as well as the zeta potential studies. The fairly longer aliphatic chain of the DDAB surfactant (average molecular mass 462 g/mol) as compared to the CTAB (average molecular mass 364.5Da) was the suspected reason for the enhanced hydrophobicity of DDAB-oCNC. Moreover, double chain surfactants adsorb better onto oxidized CNC than single-tailed surfactant, which provided a plausible reason for the observed hydrophobicity and the remarkable dispersion noted in the epoxy/DDAB-oCNC nanocomposites. From SEM and TEM observations, it can be deduced that the surfactant treated oCNC have better compatibility with the epoxy matrix, with the DDAB-oCNC showing the best dispersion among the three studied surfactants.

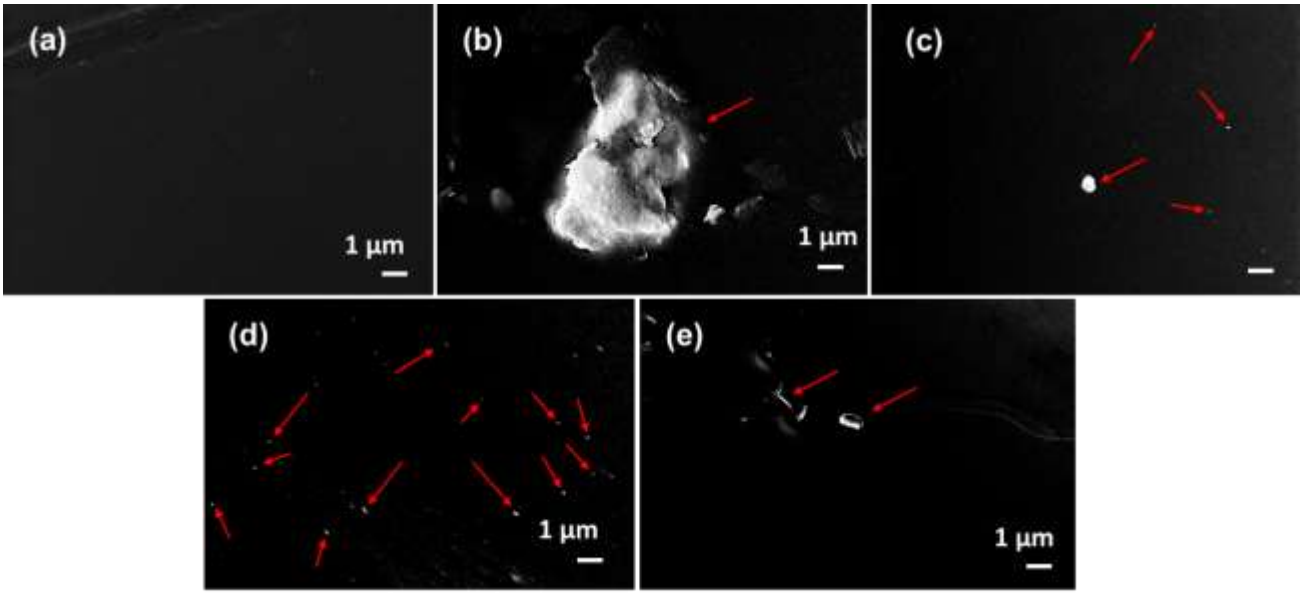

Figure 3.11. SEM images of the surface of (a) neat epoxy (b) epoxy/CNC nanocomposite (c) epoxy/CTAB-oCNC (d) epoxy/DDAB-oCNC and (e) epoxy/ DHAB-oCNC nanocomposite. Red arrow indicates the CNC or modified CNC particles.

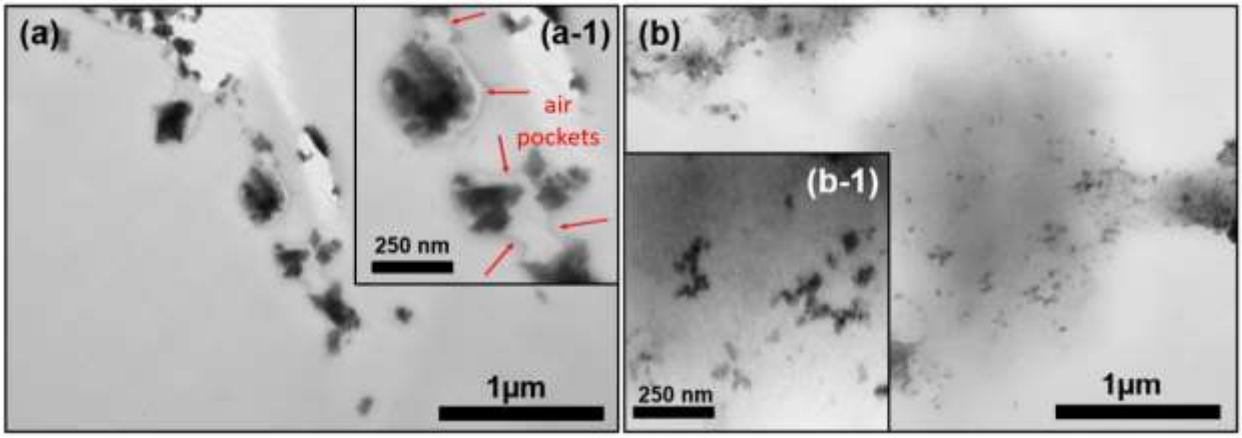

Figure 3.12. TEM images of (a) epoxy/CNC and (b) epoxy/DDAB-oCNC nanocomposites.

3.3.10.2 Salt spray test

A salt spray test was performed to evaluate the corrosion protection performance of the cationic surfactant modified CNC in comparison to unfilled and native CNC filled epoxy nanocomposite coatings. **Figure 3.13** illustrated the corrosion progress of steel coated with unfilled epoxy, epoxy/native CNC, epoxy/CTAB-oCNC epoxy/DDAB-oCNC, and epoxy/

DHAB-oCNC over 15-days experimental period. It was interesting to note that the steel coated with the neat epoxy (**1**) and epoxy/CNC (**2**) started to corrode immediately after day 1 while the epoxy/surfactant-oCNC (**3-5**) provided excellent protection for the metal substrate (**Figure 3.13b).** The addition of the hydrophilic CNC into the epoxy matrix was expected to increase the water absorption of the coating, which could have caused the accelerated corrosion noted in the CNC/epoxy samples. In addition, the native CNC had poor interfacial interaction with the epoxy matrix as noted from the air pockets around CNC aggregates (**Figure 3.12 (a-1)**). These air pockets could suck in and store water like a sponge and transfers to similar pockets adjacent to it. It is plausible that such a phenomenon has enhanced the diffusion of electrolytes that caused the observed high corrosion in the native CNC based coatings.

The nanocomposite with the surfactant-modified CNC revealed slight signs of corrosion after day 5 (**Figure 3.13c).** By day 15 (**Figure 3.13f),** the tests showed a distinct difference among the various surfactant modified CNC based composites. The DDAB-oCNC nanocomposite showed superior anticorrosion performance over the epoxy/CTAB-oCNC as well as the epoxy/DHAB-oCNC coating. The anticorrosion properties of the nanocomposite coating had likely emanated from the excellent dispersibility of the DDAB-oCNC in the epoxy matrix [119]. Such highly dispersed nanoparticles had likely filled micro- and nano- pores in the epoxy matrix to limit moisture (and electrolyte) penetration that causes corrosion. Furthermore, the higher level of hydrophobicity of DDAB-oCNC had provided better barrier against the salt solution used for the test.

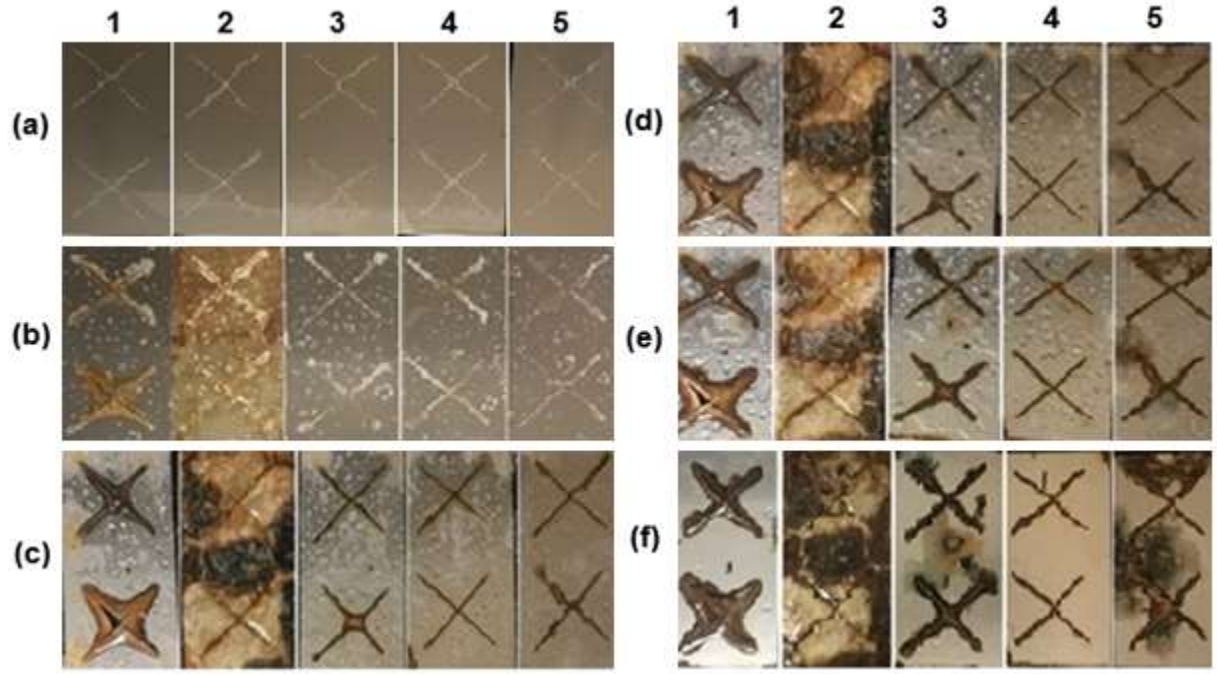

Figure 3.13. Photograph images of steel panels coated with different epoxy nanocomposite formulations under salt spray test at (a) day 0 (b) day 1 (c) day 5 (d) day 7 and (e) day 10 and (f) day 15. 1, 2, 3, 4 and 5 represent the neat epoxy, epoxy/CNC, epoxy/CTAB-oCNC, epoxy/DDAB-oCNC and epoxy/ DHAB-oCNC, respectively.

Figure 3.14 displayed the moisture barrier mechanism via the epoxy/surfactant-modified CNC nanocomposite coating that resulted in corrosion prevention properties. This model was based on the "tortuous path " model, which had been successfully used to explain the excellent barrier properties of polymer/clay and polymer/graphene nanocomposites [166]. In the absence of the modified CNCs in the matrix, the corrosive particles would diffuse rapidly into the coating. The addition of the compatible and better dispersing surfactant-modified CNCs could have increased the tortuosity of the salt solution to travel through the coating, and this has decreased the rate of corrosion of the nanocomposites as compared to the unfilled epoxy. According to this model, the DDAB-oCNC would produce the longest tortuous path and fill the porosity of the matrix, stemmed from the greatest hydrophobicity and hence enhanced dispersion and interfacial interaction in comparison with the other surfactant modified CNCs within the polymer matrix as

noted from the SEM result. Moreover, the hydrophobic CNCs retards the diffusion of water (carrier of electrolyte) through the coating. As such, the DDAB-oCNC based nanocomposites offered the best corrosion protection to the metal over the experimental period.

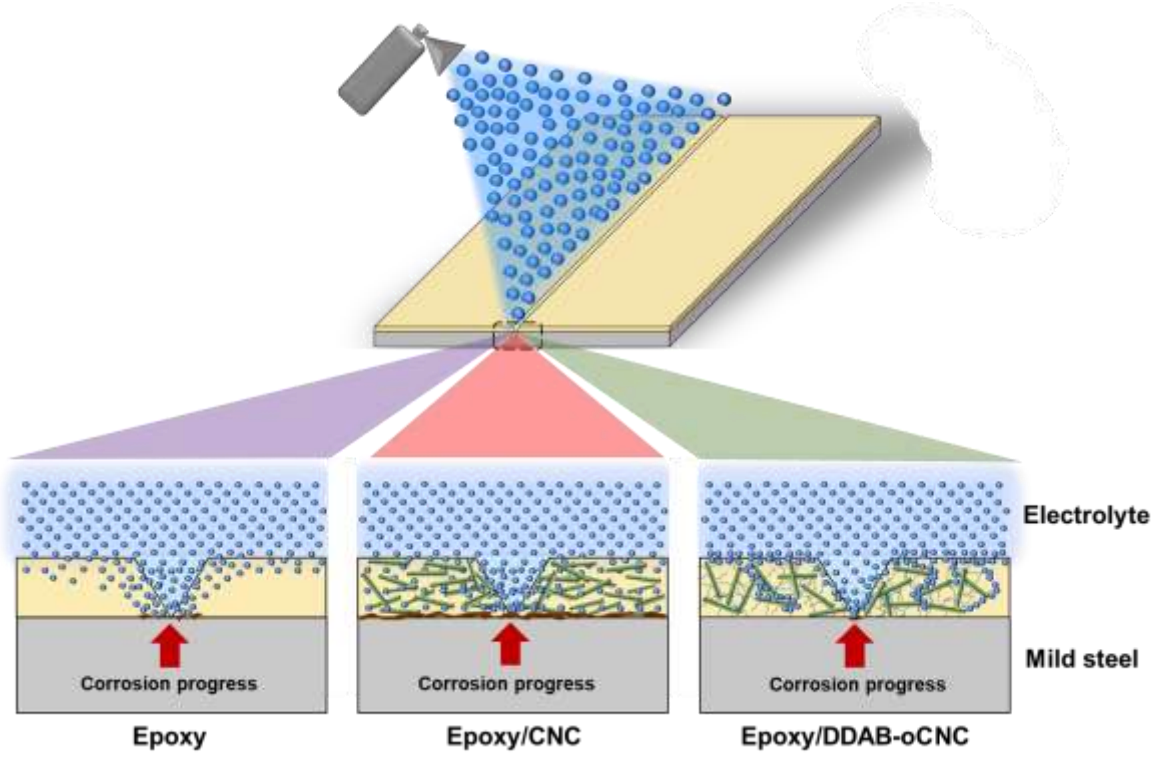

Figure 3.14. Schematic representative of tortuosity path (blue dots) of the corrosive molecules diffused through unfilled epoxy, epoxy/CNC and Epoxy/DDAB-oCNC nancocomposite coatings.

3.3.10.3 Electrochemistry of nanocomposites coating

The electrochemical corrosion studies were performed to complement the salt spray test finding as this analysis provides additional quantitative results. The open-circuit potential was studied for the unfilled epoxy and the nanocomposite coatings after a 2 h immersion in 3 wt. % NaCl solution. **Figure 3.15a** provided a summary of these measurements. A more positive corrosion potential (E_{corr}) was observed for the epoxy nanocomposites fabricated with the surfactant-modified CNCs, indicating better barrier properties by the protective coating against the corrosion inducing solution. Similar to the salt spray test, enhanced dispersion of the CNC

nanoparticles in the epoxy matrix led to a longer tortuous path and hence good corrosion protection behavior [114]. The neat epoxy and epoxy/CNC composites were susceptible to the diffusion of the corrosive molecules from the electrolyte solution and hence they have higher E_{corr} values. The epoxy/DDAB-oCNC showed the highest positive potential, and therefore the DDAB-oCNC was the best filler to bring about metal corrosion protection in coatings among the studied modifications.

The potentiodynamic polarization curves of all the formulations that were used to coat the mild steels are compiled in **Figure 3.15b**. The neat epoxy and epoxy/CNC show E_{corr} of -0.63 V, which signaled that they are the most vulnerable to corrosion. The coating with the epoxy/DDAB-oCNC exhibited the lowest E_{corr} (-0.58 V) and the corrosion current density I_{corr} (-1.58 mA/cm^2) as demonstrated in **Figure 3.15c**. The potentiodynamic polarization study further validated the OCP studies, the salt spray test, and the SEM observation that the epoxy/DDAB-oCNC nanocomposite coating performed the best in protecting metals from the corrosion

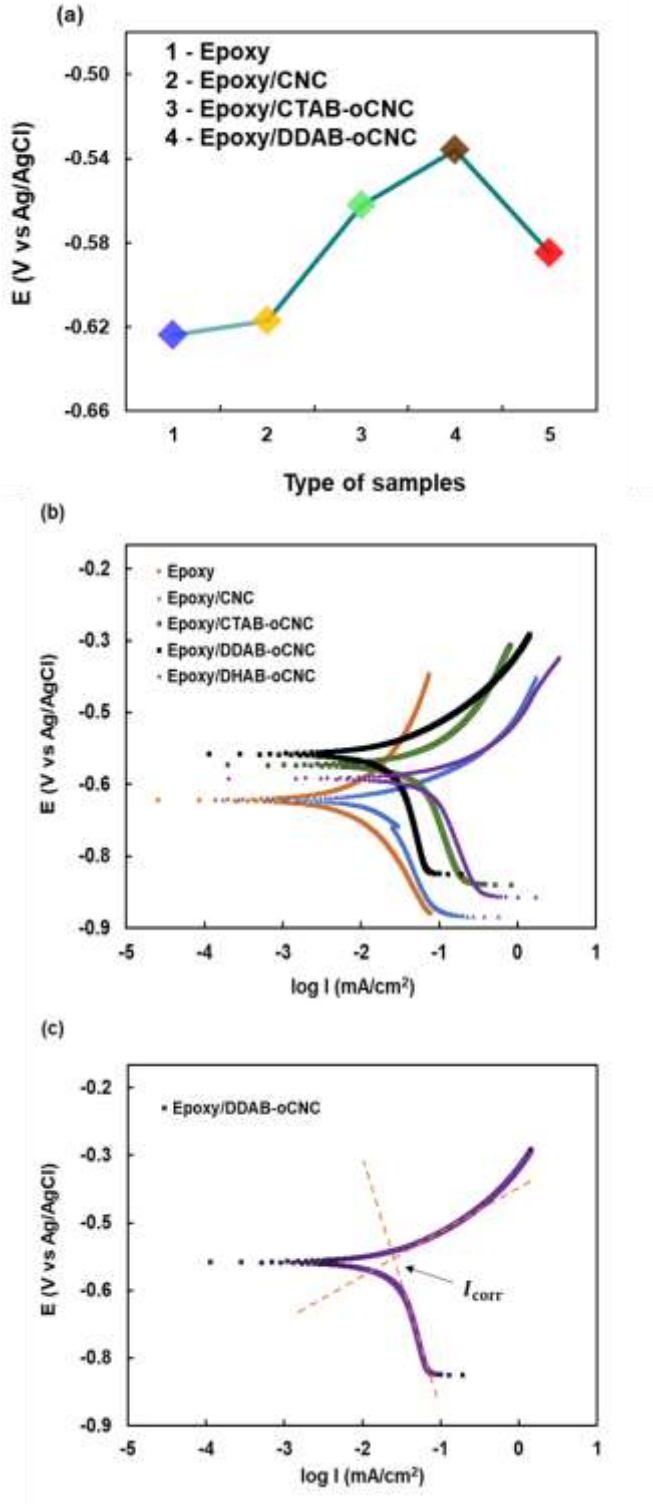

Figure 3.15. Electrochemical results of (a) open circuit potential after 2 h immersion, (b) potentiodynamic polarization curves of all composite coating and (c) polarization graph of epoxy/DDAB-oCNC nanocomposite.

3.4 Conclusions

In this work, CNC was modified with three different kinds of ammonium cationic surfactants (CTAB, DDAB, DHAB) through a three-step process. This involved oxidizing the CNC with the TEMPO catalyst followed by deprotonation of the oxidized CNCs and finally the adsorptions of the surfactants onto the deprotonated CNCs through electrostatic interaction. The surfactant-modified CNCs were shown to be more hydrophobic and dispersible in non-polar solvents, such as THF than the unmodified CNC. Moreover, water contact angle measurements displayed that the surfactant modified CNCs had100 – 200 % higher contact angles as compared to the native CNCs, conforming the hydrophobicity caused by the surfactant modification. The three types of surfactant-modified CNCs were incorporated into epoxy to form nanocomposite coating for mild steel substrates together with native CNC and unfilled epoxy-based control coating formulations. SEM results showed that the surfactant-modified CNCs were substantially more dispersible than native CNCs in epoxy matrices. Inspection of the steel corrosion from the salt spray test revealed that the DDAB-oCNC showed remarkable corrosion protection as compared to the other two surfactant-modified CNCs (DDAB-oCNC, DHAB-oCNC) as well as the control formulations. The electrochemical study provided further validation that this epoxy/DDAB-oCNC nanocomposite was the least susceptible to expose the metal to corrosion with the lowest E_{corr} (-0.58 V) and I_{corr} (-1.58 mA/cm^2). Overall, the surfactant modification improved the dispersibility of CNC in epoxy, due to the increase in the hydrophobicity that resulted in an enhanced dispersibility of the nanoparticle in the epoxy. This provided a remarkable barrier property against moisture or other corrosion inducing particles to the epoxy matrix. CNCs have already attracted substantial interest as a green nanomaterial that provides excellent mechanical reinforcement to epoxy as well as other polymers. The tailoring of CNC surfaces via a facile

process that maintained their desired crystallinity and nanostructure while enhancing their compatibility with hydrophobic polymer matrices could further expand their utility in several advanced multifunctional material applications.

Chapter 4. Hydrophobic Functionalization of Cellulose Nanocrystals for Enhanced Corrosion Resistance of Polyurethane Nanocomposite Coatings

4.1 Introduction

Organic coatings are extensively used in the industry to create a protective physical barrier to metal substrates from corrosions. However, environmental conditions such as oxygen, chlorides, and change in pH among others damage these coatings over time, leading to the loss of long term stability[167]. Researchers have incorporated corrosive inhibitors into organic coating formulations to improve their protective properties. Chen-Yang et al. have successfully incorporated quaternary ammonium salt modified montmorillonite clay into PU coating and observed through electrochemical studies that the corrosion protection of PU/clay nanocomposites was enhanced even at low clay loading concentrations [120]. Likewise, an improvement in thermal stability and flame retardancy of the composite coating was observed. Similarly, Pilch-Pitera et al. prepared sonication-assisted PU based powder clear coatings with modified multiwalled carbon nanotubes (MWCNTs) [168]. The result showed an improvement in nanofiller dispersion in PU, with the composites exhibiting increased electrical conductivity and corrosion resistance. Other nanofillers such as graphene oxide [169], titanium oxide [170], organically modified silicates [171], nano aluminum oxide [172] are also commonly used to improve corrosion properties of metal coatings.

Cellulose nanocrystals (CNC) are rod-like nanoparticles with 10-20 nm diameters and a few hundred nanometers in length [173,174], depending on the biological source and isolation protocol. These nanoparticles are commonly obtained by acid hydrolysis of cellulose fibres from wood, pulp, and plant fibres [143,174,175]. CNC is not only a corrosion inhibiting agent but it also possesses additional appealing properties that include high crystallinity, surface area (250-500

m^2/g) and stiffness (Young's modulus of 100-140 GPa), with low density, biodegradability, sustainability, and non-toxicity [88,125,176]. Due to the combination of these characteristics, they have been utilized as a reinforcing agent in many polymer composites such as polylactic acid, polyethylene, polypropylene, epoxy, and polyurethane [177]. One major drawback of utilizing native CNC in polymer composites coating is that it exhibits strong self-association due to hydrogen bonding of surface hydroxyl groups, which leads to particle aggregation that limits diminished or reduced integrity of the polymer composites. To improve nanoparticle dispersion in polymers, the surface of CNC can be functionalized with surfactants such as polyethyleneimine (PEI), cetyltetramethylammoniumbromide (CTAB), dimethyl dodecylethyl ammonium bromide (DDAB) or surface modified with hydrophobic molecules such as acrylonitrile butadiene rubber, fatty acids, pentafluorobenzoyl chloride, and chlorosilanes [2,89,91,106,123,143].

Among all CNC modifications, silanization is very attractive due to the large scale availability of silane, cost-effectiveness, variety of functional moieties of silane, ease of the reaction chemistry and mild aqueous reaction medium[178,179]. Moreover, silane agents are widely accepted in the polymer industry as adhesion promoters that enhance the bonding of fillers with organic polymer matrices[180]. The treatment of metal substrates with hydrophobic silane without paint coating also shows an improvement in metal corrosion prevention [181]. Thus, it is logical to expect that the incorporation of hydrophobic silane grafted CNC, which is highly crystalline, can reduce the diffusion of corrosive agents through the coating resulting in an enhanced corrosion inhibition performance of the organic coatings. The grafting of various silane coupling agents on CNC surfaces, such as 3-aminopropyltriethoxysilane (APTES) [182], N-(β-aminoethyl)-γ-aminopropyl- trimethoxysilane (AEAPTMS) [178], 3-glycidoxypropyltrimethoxysilane (GPTMS) [165] and 3-methacryloxy-propyltrimethoxysilane

(MPS) [183] have been reported in the literature with various degrees of success. The goals of modifications in these studies were typically to enhance mechanical properties of composites. In this study, we selected a novel silane coupling agent, 2-(3,4-epoxycyclohexyl) ethyltrimethoxysilane (ES), as a hydrophobic modifying agent for CNC to enhance the corrosion resistance of PU nanocomposite coatings. ES has advantages over other silane compounds because it would not only improve the dispersion of CNC in the PU but also introduce epoxide end group, which can be chemically crosslinked with the isocyanate in the PU formulation to form strong adhesion in the PU matrix.

Thus, the aim of this study was to synthesize hydrophobic modified CNC (ES-CNC) via silanization in aqueous solution for corrosion resistant PU coating applications. Through various characterizations, an optimal modified CNC sample was chosen, and this was then used to formulate and fabricate PU/ES-CNC nanocomposite coatings at various concentrations. A film applicator was used to apply a uniform and even layer of the PU nanocomposite formulations onto mild steel. Thus, we report herein the ES grafting on CNC, which resulted in highly dispersible nanoparticles in PU, for the fabrication of PU nanocomposite coating that exhibited excellent corrosion protection while at the same time being a stiff coating structure that potentially is dent and abrasion-resistant.

4.2 Experimental

4.2.1 Materials

Dried CNC powder was provided by CelluForce Inc (Montreal, Canada). The dried CNC contains about 0.87% sulfur content, originating from the acid hydrolysis process. Epoxide functionalized silane agent (2-(3,4-epoxycyclohexyl) ethyltrimethoxysilane, ES) was purchased from Gelest (Pennsylvania, USA). Acetic acid and ethanol (EtOH) were purchased from Sigma

Aldrich (Oakville, Canada). Methylenediphenylenediisocyanate (MDI; Suprasec 2496) was obtained from Huntsman Polyurethanes (Michigan, USA) and Albodur 912 VP (castor oil polyol) was acquired from Alberberdingk Boley Co (North Carolina, USA). All the chemicals were used as received.

4.2.2 Modification of CNC with epoxide-functionalized silane

The modification of CNC with epoxide functionalized silane agent was carried out in an aqueous medium. First, a calculated quantity of ES was added into 100 mL solution of ethanol/water (80/20 V/V). The solutions were adjusted to pH 5 using concentrated acetic acid under magnetic stirring. The ES solution was allowed to hydrolyze while stirring at room temperature for 30 min. A CNC aqueous dispersion (4 wt. %) was prepared by dispersing dried CNC in deionized (DI) water via homogenization (25,000 rpm, PowerGen 700 Homogenizer) for 5 min and then sonication (CPX 2800 ultrasonic, Fisherbrand) for 30 min. The CNC dispersion was introduced slowly into the ES solution under stirring at room temperature. Once the reaction time was completed, the reaction mixture was distilled using rotary evaporated at 85 ^{o}C to remove ethanol solution, and the product was dried in an oven at 50 ^{o}C for three consecutive days. The dried products were crushed using a mortar and pestle to obtain fine powder and washed with ethanol at least three times to remove any unreacted ES. Finally, the samples were dried in a vacuum oven at 80 ^{o}C to remove trace EtOH solvent. Three different silane treated cellulose nanocrystals (ES-CNC) were prepared by varying the ratio of ES to CNC and the reaction time using the aforementioned procedure. These are ES- CNC1 (1:1 molar ratio of ES:CNC, 3 h reaction time), ES-CNC2 (1:1 ratio of ES:CNC, 12 h reaction time) and ES- CNC3 (5:1 ratio of ES:CNC, 12 h reaction time).

4.2.3 Characterizations of modified CNC

4.2.3.1 Fourier transform infrared spectroscopy (FTIR)

Native CNC and ES-CNC samples were analyzed using FTIR (ATR-FTIR Nicolet 6700, Thermo Scientific Inc) to obtained IR Spectra. The dried pellets for analysis were prepared by grinding approximately 200 mg of dried potassium bromide with 5 mg of the samples and pressed into pellets using pellet die sets. The spectrum was scanned between 500 and 4000 cm^{-1} using transmittance mode with 32 scans. Dried potassium bromide pellet was used as a background for the FTIR measurements.

4.2.3.2 Elemental analysis (EA)

The elemental compositions (carbon, oxygen) of native CNC and modified CNC (ES-CNC1, ES-CNC2 and ES-CNC3) were obtained using a 4010 Elemental Analyzer (Costech Instrument, Italy). Triplicates for each sample was run and the average results reported along with their standard deviation.

4.2.3.3 X-ray Photoelectron Spectroscopy (XPS)

The analysis of the XPS spectrum was performed to determine functional group changes and surface chemical compositions of the samples. XPS (Thermo-VG Scientific ESCA Lab 250 microprobe, Thermo Fisher Scientific) with Al-Kα radiation was performed on both native CNC and three modified CNC. Casa XPS software was used to analyze and fit peaks from XPS data.

4.2.3.4 Thermogravimetric analysis (TGA)

The thermal stability of the silane treated CNC and the native CNC were compared using Thermogravimetric analysis (TGA 500, TA Instrument). The measurements were conducted with a heating rate of 5 ℃/min from 100 to 600 ℃ under nitrogen flow mode. The degradation

temperature and weight loss of the samples during the analysis were used to evaluate the stability of the modified CNC.

4.2.3.5 X-ray diffraction (XRD)

To investigate the crystallinity profiles, native CNC and modified CNC were analyzed using X-ray diffractometer D8 Discover (Bruker, Kaelsruhe, Germany) with a Cu-Kα as the radiation source. The scanning angle (2θ) were recorded from 5 to 45 ^{o} with parameter setting of 40 kV, 40 mA, and 0.02 step size.

4.2.3.6 Morphology studies

Transmission electron microscopy, TEM, (Philips, CM 10) were employed to obtain the morphology of CNC and ES-CNC samples. The samples were prepared by dispersing the native and modified CNC (ES-CNC3, 0.3 wt.%) powder in toluene solution and stained with uranyl acetate before casting on TEM carbon-coated copper grid for analysis.

4.2.3.7 Water contact angle (WCA) and dispersibility studies

The wettability of samples was quantitatively evaluated using water contact angle (WCA) measurement. For this, the native and modified CNC were dispersed in toluene (1 wt. %), cast onto the glass slides, and allowed to dry in the fume hood at room temperature. The solution casting was performed 10 times to guarantee the glass surfaces were fully covered by the samples. About 3 µL of DI water was then dropped onto the film, and a custom-built optical sessile drop system was used to obtain a photograph of a water droplet on the sample films. The images of the droplet-surface interaction were captured with a digital camera, and the contact angles were analyzed and quantified using ImageJ software.

The change in polarity of the CNC as a result of the modification was also examined by dispersing the nanoparticles in five solvents with varying polarity: water, EtOH, tetrahydrofuran

(THF), toluene and castor oil polyol. For this, 1 wt.% of the native and highly modified CNC (ES-CNC3) were dispersed in the solvents with the aid of homogenization (2 min), followed by sonication (5 min). A digital camera was then employed to record of the variation in the dispersive behaviors of the native and ES-CNC3 in the selected solvents.

4.2.4 Nanocomposite coating

4.2.4.1 Fabrication of polyurethane/ES-CNC nanocomposite coatings

To fabricate PU/ES-CNC nanocomposites, a pre-dispersed ES-CNC (1, 3, 5 wt. %) was first added into caster oil polyol and sonicated using bath sonicator for 30 min. The dispersion was degassed in a vacuum oven at 50 ℃ until no bubbles were observed. Isocyanate crosslinking (0.25 ratio of castor oil polyol) was slowly added into the mixture, stirred continuously for 5 min, and degassed again for 10 min. Samples prepared as such were then coated onto mild steel plates (Q panel R46, Q-Lab Corporation) using a blade film applicator (Yuchengtech, China) that provides a consistent 200 μm thick layer. The same samples were also cast in a silicone mould to prepare test specimens for dynamic mechanical analysis, water absorption, and morphology evaluation. The samples were then allowed to cure at room temperature overnight before post-curing at 50 ^{o}C for 3 h in an oven. For comparison, PU/CNC composites with native CNC loading of 1, 3, 5 wt. % were also prepared using the same procedures.

4.2.4.2 Morphology of nanocomposite coating

The morphology of the nanocomposites was evaluated using Scanning Electron Microscopy (SEM) instrument (Zeiss Leo, 1530). Specimens for SEM studies were gold-coated (~3 to 4 nm) using a gold sputter coater to enhance contrast for image collection. The SEM images of cross-section of the nanocomposites were collected and analyzed.

4.2.4.3 Dynamic mechanical analysis (DMA)

The dynamic mechanical analysis was carried out on the PU, PU/CNC and PU/ES-CNC nanocomposite samples using TA instrument (DMA Q800). The analysis was carried out on specimens with dimension (60 × 12.7 × 3.2 mm) in dual cantilever mode with a temperature ranges from -100 to 100 ^{o}C and a frequency of 1 Hz. The storage modulus and tan delta of all samples were collected and analyzed.

4.2.4.4 Water absorption test

Water absorption test was performed according to D570-98 ASTM standard with minor modifications. The sample specimens were prepared as rectangular bars with a dimension of 30 x 20 x 2 mm. The samples were dried in an oven for 24 h before the test and the initial constant weight was recorded right after drying. These samples were then immersed in DI water and the weight of samples was recorded every hour for the first 8 h and then once every 24 h for 7 days. After the first week of measurement, the weights were recorded once every week for two weeks. The water absorption was determined using the following formula

$$\%\, water\ absorbance = \frac{W_2 - W_1}{W_1} \times 100 \qquad (4)$$

where w_1, w_2 represent the initial weight of the dried sample and weight of immersed samples at the different time intervals, respectively.

4.2.4.5 Salt spray test

Salt spray test was used to qualitative evaluate the corrosion performance of organic nanocomposite coating on metal substrates. The coated metal plates were scratched with an “x” pattern using sharp blades. The salt spray test was then conducted in accordance with ASTM B117 standard with minor modifications. Sodium chloride (NaCl, 5 wt. %) at neutral pH was used to

induce the corrosion and it was performed by spraying the salt solutions on the scratched metal plates once a day for 25 consecutive days. A digital camera was used to record the corrosion progress and overall quality of the coating along the scratched "x" marks on the steel panels.

4.2.4.6 Electrochemical impedance spectroscopy (EIS)

A three-electrode electrochemical cell was used to examine electrochemistry and EIS of various PU composite coatings. The coated or uncoated panels were used as working electrode while graphite and standard silver/silver chloride (Ag/AgCl) were used as a counter and a reference electrode, respectively. The studies were performed in neutral aqueous solution of 3.5 wt.% NaCl in an open-air system at two immersion times (1 h and 3 h). Bio-Logic EIS/Potentiostat (VSP, Bio-Logic Science Instruments, France) was used to measured the electrochemical responses over a broad frequency range (100 kHz to 10 MHz) using a 50mV sinusoidal voltage amplitude. The EIS responses were analyzed using EC-Lab software (EC-Lab®, BioLogic Science Instruments, France).

4.2.5 Statistical analysis

The statistical standard deviation was obtained by analyzing experimental data using the statistical software package Minitab (Version 18). Single factor analysis of variance (ANOVA) was performed with a 95% confidence level ($P < 0.05$).

4.3 Results and discussion

4.3.1 Modification of CNC with an epoxide functionalized silane

To synthesize hydrophobic materials, low surface energy reagents are typically required. Silanes are among the prominent low surface compounds that are extensively used due to the ease of the reaction chemistry and the low toxicity of the process. Silanization reactions have been well

understood on diverse substrates such as silicon oxide, titanium dioxide, and a range of polysaccharides[38,184–186]. In this study, CNC was surface modified with ES using mild reaction conditions that could maintain its high crystallinity, while providing hydrophobic nanoparticles. The goal of the modification is to enhance the dispersion of CNC in PU matrices, and more importantly to reduce the water affinity of CNC that otherwise are hydrophilic in the coating application. Based on previous investigations of the silanization of –OH functionalized particles (e.g. silica, TiO_2), a plausible reaction mechanism is proposed for the surface modification of CNC with ES (**Figure 4.1**). In the proposed scheme, an aqueous solution containing ES was first hydrolyzed with acetic acid (CH_3COOH). The -CH_3 of the methoxy group on ES is replaced by -OH groups to form silanol (Si-OH) compounds. A condensation reaction occurs to form Si-O-Si bonds by removing additional water from the reaction [184]. Finally, the intermediate silanol compounds are allowed to react with the -OH group (silanization reactive sites) of CNC to form ES-CNC. In this reaction, the R functional group of silane compound will not be hydrolyzed [38], and this moiety might be favourable in tailoring the adhesion toward polymers in polymer nanocomposites. The hydrophobicity of modified CNC could emanate from the replacement of -OH polar group with the inorganic-organic (Si-O-Si) networks shielding the CNC nanoparticles. Furthermore, the R chain might also contribute to the hydrophobicity due to the epoxide and extension of alkyl chains.

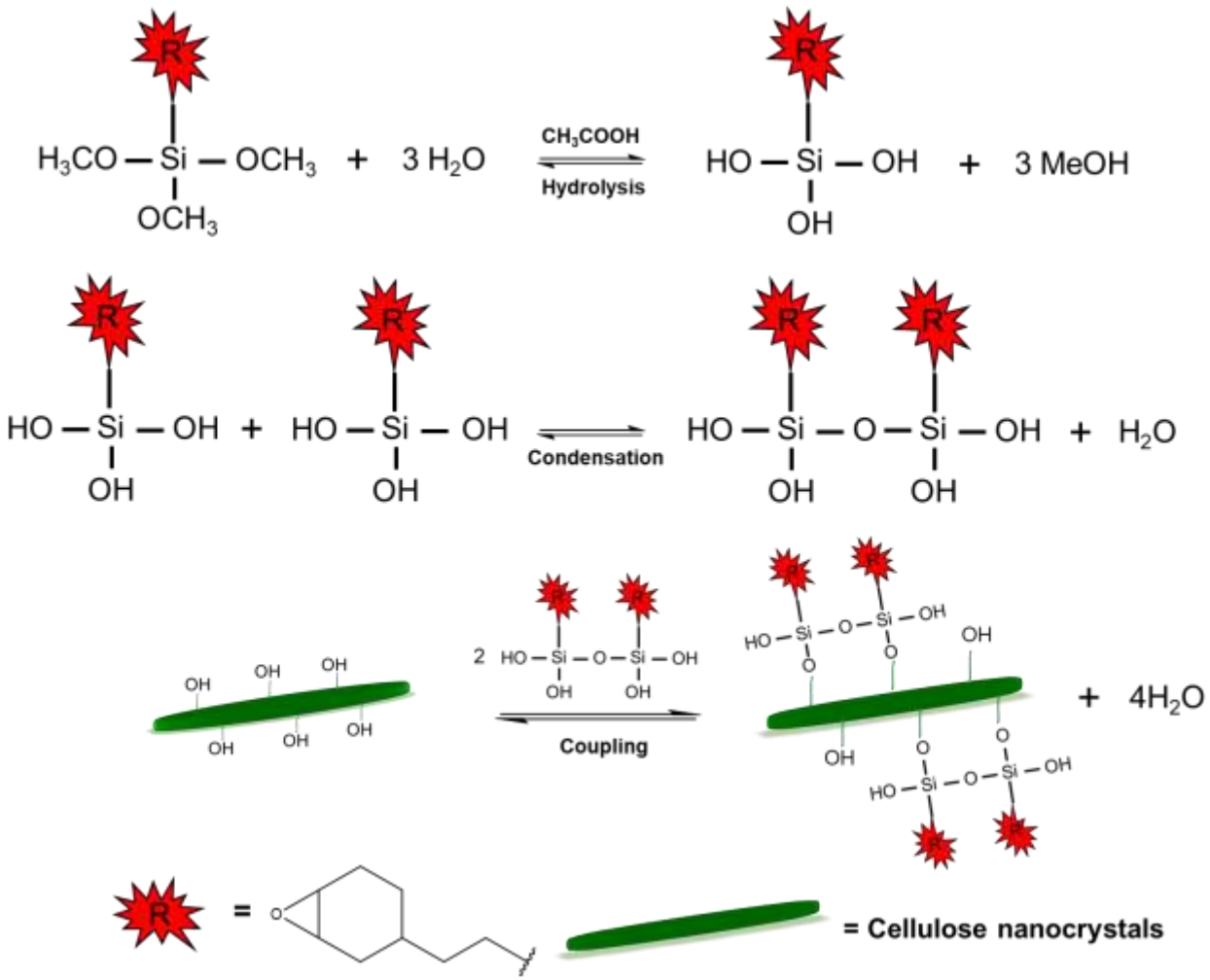

Figure 4.1. Illustration of epoxide functionalized silane modification of CNC through a three-step process: hydrolysis, condensation and coupling of the intermediate silanol to the cellulose nanocrystals.

4.3.2 Characterization of epoxide functionalized silane treated CNC

4.3.2.1 Fourier transform infrared spectroscopy (FTIR)

The surface chemical change of CNC through silane modification can be investigated using FTIR. **Figure 4.2a** displays the FTIR spectrum of the native and modified CNC. The characteristic peaks of the native CNC are at 3450 and 2920 cm^{-1} , which correspond to the stretching vibration of -OH hydroxyl bonds and of C-H bonds, respectively [106,143–145,187]. CNC is well known for their high hydrophilicity and tend to adsorb water easily. As such, the additional peak at 1640

cm^{-1} of the CNC spectra is associated with the OH bending of the adsorbed water [106,145,148]. In the modified CNC (ES-CNC1, ES-CNC2 and ES-CNC3), new peaks were observed (2940 and 2870 cm^{-1}), which can be attributed to the asymmetric and symmetric stretching of CH_2 group of ES agent, respectively [188]. The surface modification of CNC was evident from the significant reduction in the transmittance signal of O-H stretching at 3450 cm^{-1}. The conversion of O-H functional groups on the CNC to O-Si-O bonds in the modified CNC reduced the amount of O-H stretching vibration and hence, lowered the transmittance signal. Similarly, the adsorbed water peak at 1640 cm^{-1} is not detected as the modified CNC are relatively hydrophobic compared to that of the unmodified CNC, which reduces its tendency to adsorb water molecules. It should be noted that the new signals of Si-O-C and Si-O-Si bond formations (1050-1170 cm^{-1}) in modified CNC are difficult to detect as they tend to overlap with the C-O-C of the native CNC. This experimental observation is in agreement with the results from the studies of CNC modification with 3-aminopropyltriethoxysilane (APTES) and 3- aminopropyltrimethoxysilane (APTMS) [165,187]. All the studied range of ES concentration provided similar modification based on the IR observation. However, samples modified with the highest levels of ES concentration (ES-CNC3) appeared to be more modified than the other two, based on the residual –OH spectra.

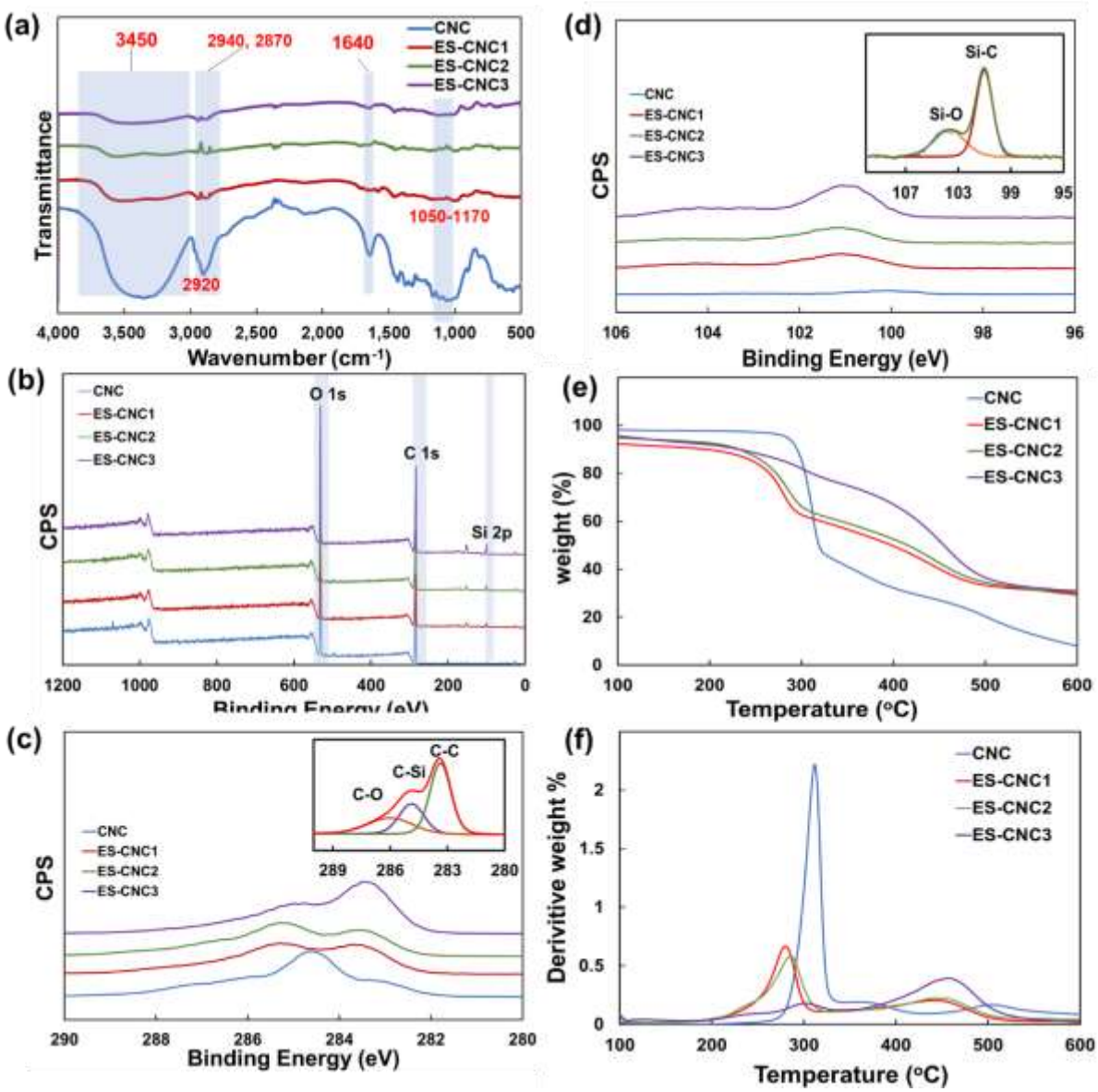

Figure 4.2. (a) FTIR spectrum of native CNC, ES-CNC1, ES-CNC2 and ES-CNC3, (b) low-resolution XPS survey of CNC and all three different ES-CNC samples, and (c and d) high resolution of C 1s and Si 2p core levels of CNC and all three different ES-CNC samples, respectively. Picture insets are the deconvoluted peak spectra of ES-CNC3 fitting using Casa XPS application. (e and f) thermal stability of unmodified and modified CNC showing weight loss and derivative weight loss from TGA analysis, respectively,

4.3.2.2 Elemental Analysis (EA)

EA was employed to determine the amount of ES grafted onto the CNC surfaces, with the results presented in **Table 4.1**. The carbon and oxygen contents of the unmodified CNC are approximately 41.28 and 46.54 %, respectively. In all modified samples (ES-CNC1, ES-CNC2

and ES-CNC3), the amount of carbon increased by about 1.7- 6 %. The increase in carbon content could be attributed to the contribution of carbon atoms from ES. On the other hand, the oxygen content of the native CNCs decreased from 46.54 to 26.72-38.25 % in the modified samples, and this was attributed to hydrolysis and condensation of silanization reaction, which removed water molecules and reduced the oxygen contents in the modified CNC. Ángel Hidalgo-Salazar and et. al studied the fibers of sugarcane bagasse and its modification with hexadecyltrimethoxysilane and obtained similar results as observed with the reduction in oxygen component in modified sample in this study [189]. It was hypothesized that reaction time and the molar ratio of ES/CNC during modification can affect the amount of grafting onto CNC. A longer reaction time could allow a higher degree of hydrolysis and condensation to occur on the surface of CNC. ES-CNC2 was observed to have higher carbon content than ES-CNC1. Similarly, the carbon percentage of ES-CNC3 is the highest among all samples and can be suggested that it has the highest level of modification. Overall, the EA results corroborated the FTIR results that CNC was successfully modified with ES.

Table 4.1. Carbon and oxygen elemental compositions of CNC and modified CNC from EA.

Sample	**Total carbon (%)**	**Total Oxygen (%)**
CNC	41.28 ± 0.39^{a}	46.54 ± 0.89^{c}
ES-CNC1	42.95 ± 0.38^{a}	38.25 ± 0.01^{a}
ES-CNC2	44.85 ± 0.46^{b}	33.31 ± 0.52^{c}
ES-CNC3	47.20 ± 0.52^{c}	26.72 ± 0.17^{b}

Value – mean ± standard deviation (n = 3), means with the same superscript letters within a column are not significantly different at the $P < 0.05$ level.

4.3.2.3 X-ray photoelectron microscopy (XPS)

To further confirm the modification of CNC, XPS was used to determine chemical states, electronic state changes and chemical composition of the surface of the modified CNC. **Figure 4.2b** presents the low resolution of XPS spectra of CNC before and after modification with ES. The XPS spectrum of CNC show binding energies of two critical peaks, C 1s (285 eV) and O 1s (532 eV) for carbon and oxygen atoms of CNC, respectively [182,190]. In all three modified samples, an additional peak (Si 2p) at 101 eV was discovered, and this peak was attributed to the silicon (Si) atoms from ES. Hossein et al. modified CNC with 3-aminopropyltriethoxysilane (APTES)[182] and achieved similar results as found with the presence of Si 2p used as confirmation of surface modification of CNC here.

To further understand the changes to the surface chemical environment of the CNC after modification, high-resolution XPS spectra of C 1s and Si 2p were investigated. **Figure 4.2c** compares C 1s electronic states transformation of CNC before and after modification. From previous studies, the C 1s peak is the overall chemical states of carbon atoms in CNC, which can be resolved to two different types of bonding: C-C, C-O or O-C-O bonds [190,191]. After modification, the C 1s signal at 285 eV can be deconvoluted to three different bonds: C-C, C-Si and C-O as shown in the insert. **Figure 4.2d** show**s** the Si 2p core-level spectra of all CNC samples. A small single peak of Si 2p was observed in CNC, which is plausibly due to impurities. A significant Si 2p peak was observed for all modified samples and can be resolved to Si-O (104 eV) and Si-C (101 eV) bonds of modified CNC. The percentage of the atomic composition of the surface of samples can be obtained from XPS analysis.

Table 4.2 presents a summary of percent atomic composition of unmodified and modified CNC from the XPS measurements. Overall, the carbon content increased in the modified samples

while their oxygen content decreased, and these evidences coincide with EA results previously discussed. Moreover, Si element was detected in all the ES-CNC samples with ES-CNC3 having the highest Si content of 9.48 %, confirming the highest level of modification. It is important to highlight here that XPS analysis provides composition of the surface, typically 50 – 70 Å as opposed to elemental analysis which analyzes the entire sample. Thus, the percentage compositions presented in **Table 4.1** and **Table 4.2** are expected to be slightly different.

Table 4.2. The surface atomic composition of unmodified and modified CNC from XPS analysis

Sample	**O 1s (%)**	**C 1s (%)**	**Si 2p (%)**
CNC	41.83	57.85	0.32
ES-CNC1	33.03	62.62	4.35
ES-CNC2	30.80	64.20	5.00
ES-CNC3	**24.71**	**65.81**	**9.48**

4.3.2.4 Thermogravimetric Analysis (TGA)

One of applications of CNC is as a reinforcing agent of polymer composites. Most thermosetting polymers, such as epoxy and polyurethane or thermoplastics are typically processed at high temperature. Thus, it is crucial that the nanoparticles used as a filler to fabricate the composites withstands the high-processing temperature. The modification of CNC with ES was expected to improve the thermal stability of CNC due to formation of Si-O-Si networks surrounding the nanorods. TGA was used to evaluate the thermal stability of the modified CNC compared to that of the native CNC, and the results are illustrated in **Figure 4.2**(**e and f**). All samples show weight loss around 100 ^{o}C, which was from the evaporation of adsorbed water on the samples [187,192,193]. The native CNC thermograph indicated a one-step decomposition with

a maximum weight loss peak at 312 ^{o}C, which was from the oxidation of anhydro-glucose units of CNC [106,143,192]. In contrast, all the modified samples displayed two weight loss peaks. The first degradation peak around 285-310 ^{o}C was suspected to be from the degradation of surface siloxane functional group surrounding the CNC, while the second decomposition at 440-460 ^{o}C was from the disassembling of CNC chain itself. The evidence shows that the CNC are successfully modified with ES agent, and the thermal stability of all modified CNC were improved due to the introduction of high molecular weight ES molecules and intermolecular crosslinking of siloxane bonds on CNC surfaces [192]. Furthermore, it was noted that ES-CNC3 has the highest thermal stability of all modified samples with its first weight loss peak at 310 ^{o}C and second peak at 460 ^{o}C. The greatest enhancement in its thermal stability was likely from the highest density of ES intermolecular crosslinking on the CNC due to the relatively higher ES grafted onto the CNC surface during the modification. All modified CNC exhibited higher residual mass at 600 ^{o}C as compared to the native CNC, which was attributed to the grafted siloxy moieties [182,193]. Overall, the TGA results indicated that the modification employed in this study enhanced the thermal stability of CNC. Also, the results are in agreement with the results observed from FTIR, EA, XPS studies that successful modification of CNC with silane agent was achieved.

4.3.2.5 X-ray diffraction (XRD)

XRD was used to examine change in crystallinity of CNC before and after modification with ES and the result is shown in **Figure 4.3**. For native CNC, the crystalline peaks are resolved into four different diffraction peaks at 15º, 16.6º, 22.6º and 34º which corresponds to $\overline{1}10$, 110, 200 and 004 planes of CNC, respectively [106]. The $\overline{1}10$ and 110 diffraction peaks are still observed in ES-CNC while 200 and 004 peaks are slightly reduced in their intensity, suggesting that the ES coupling agent was introduced to the surface of CNC. It should be noticed there was a

high intensity and broader diffracted peak at 26.22º, which is suspected to originated from the silica of the ES modifying agent [194].

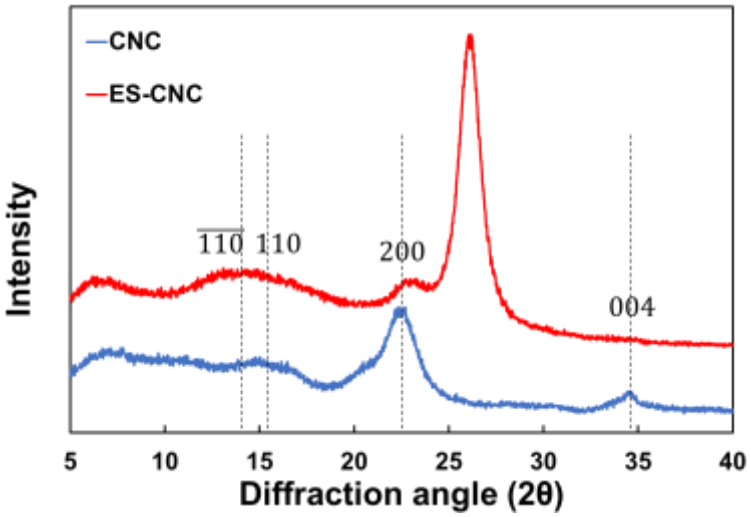

Figure 4.3. X-ray diffraction of CNC and ES modified CNC.

4.3.2.6 Morphology of modified CNC

Figure 4.4 illustrates the morphology of pristine CNC and modified CNC with ES. The native CNC displayed a rod-like structure as observed in **Figure 4.4a** and the morphology is very similar to others reported in the literature [195,196]. After the modification, the rod-like shape of the CNC changes. **Figure 4.4b** shows the distribution of the black dots along microfibrillar-like structures of ES-CNC. These dark spots are indicative of the presence of the high atomic mass silicon atoms, which are suspected to inhibit transmitted electron of TEM to pass through the carbon grid and give rise to the black dot contrast on TEM photograph. It should be noticed that the ES-CNC web-like structure are not obviously observed (low atomic number of carbon atom), which is suspected to be from the contrast interfering with high density siloxane networks surrounding CNC. One other significant observation is the CNC agglomeration in toluene as opposed to ES-CNC that exhibited good dispersibility in toluene due to the hydrophobic nanoparticle/solvent compatibility.

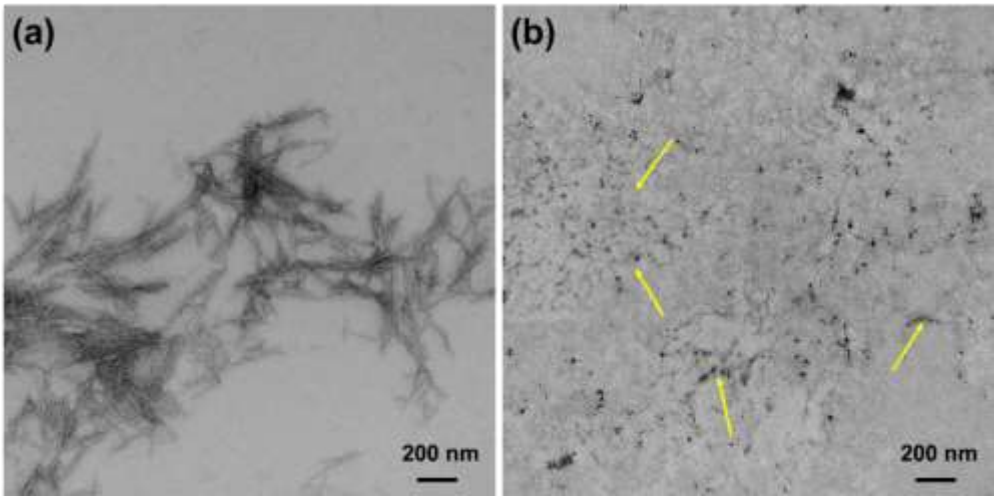

Figure 4.4. TEM morphology of (a) CNC and (b) ES-CNC.

4.3.2.7 Hydrophobicity of the surface modified CNC

Material wettability such as hydrophobicity and superhydrophobicity can be quantified using water contact angle (WCA) [6,14]. **Figure 4.5a** presents the digital photographs of WCA on the surface of native and modified CNC. Native CNC are inherently hydrophilic materials due to the abundant surface -OH group, and such hydrophilicity is substantiated by the low WCA of about 25.6° [106,143]. The modification of CNC with ES agent have significantly increased the WCA of the CNC due to the conversion of -OH group to web-like network of O-Si-O on the CNC surfaces. Furthermore, epoxide functional group on siloxy moieties has likely contributed to the hydrophobicity of modified CNC. ES-CNC1 has a WCA of 55.1° as compared to 25.6° for that of the native CNC. On the other hand, ES-CNC2 has higher WCA (58.1°); slightly higher than that of ES-CNC1, which could be from the higher grafting degree of ES on the CNC. ES-CNC3, which was the most modified sample, exhibited the highest WCA (72.5°). Abdelmouleh and et al modified cellulose with γ-Aminoproyltriethoxysilane (APS) and achieved a maximum WCA of 75° [197]. Similarly, Lu and et al. successfully prepared 3-glycidoxypropyltrimethoxysilane (GPS)

treated micro-fibrillated cellulose with a WCA of 64° [198]. APS, GPS and ES have similar chemical structures and lengths, which could be attributed to the similarity in WCA when grafted to cellulose/CNC. Based on this result, it can be concluded that the modified CNC is remarkably more hydrophobic as compared to the native CNC.

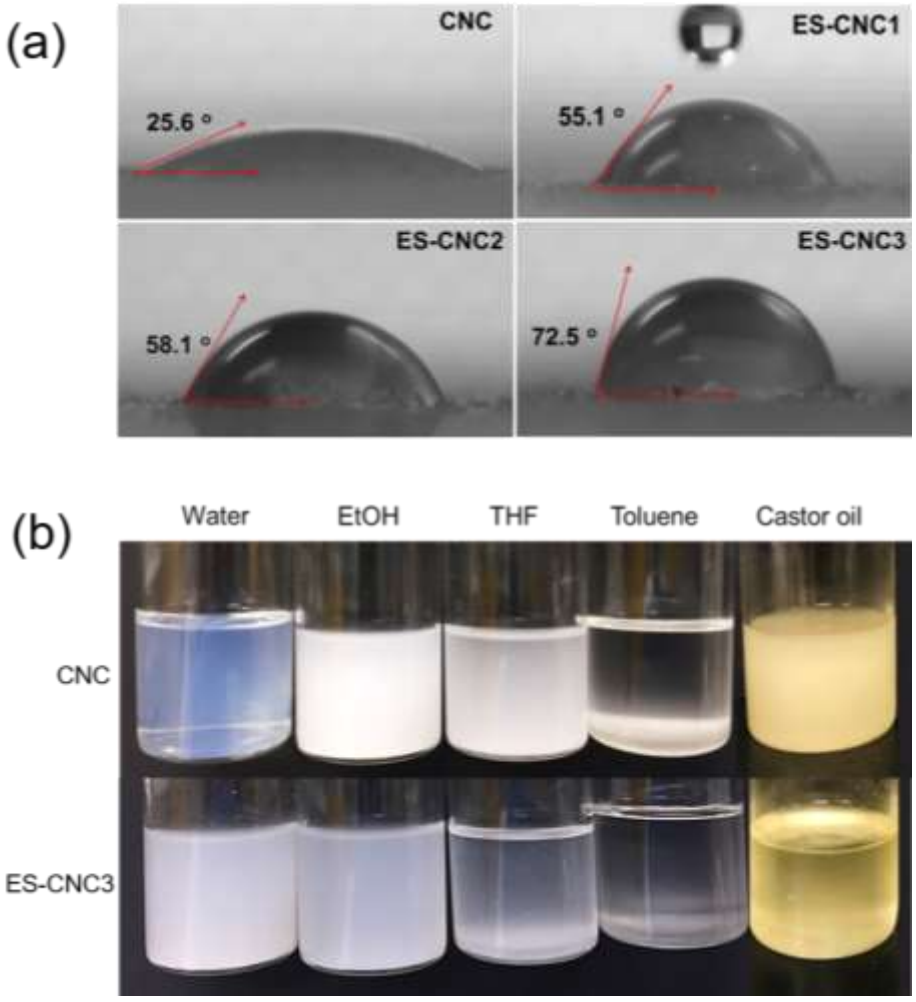

Figure 4.5. (a) Water contact angle (WCA) of CNC, ES-CNC1, ES-CNC-2 and ES-CNC3, and (b) Photographs showing dispersibility CNC and the highest modified CNC (ES-CNC3) in water, EtOH, THF, toluene and caster oil polyol.

The polarity conversion of samples can be evaluated using a dispersibility test. Typically, hydrophilic molecules disperse well in water and other polar agents such as carboxylic acid while hydrophobic molecules are better dispersed in hydrophobic solvent such as THF,

tetrachloromethane, toluene and benzene. **Figure 4.5b** illustrates a comparison between of the dispersion of CNC and ES-CNC3 in water, ethanol, THF and toluene. Since native CNC are hydrophilic nanoparticles, they disperse well in water, demonstrated by the clear and stable aqueous suspension. As the relative polarity decreases across the solvents from ethanol to toluene, CNC begins to aggregate and form large particles and finally falls to bottom of the solvents and forms sediments as shown in the toluene dispersibility result. Contrarily, ES-CNC3 in water showed cloudiness, indicating poor dispersibility. A progressive reduction in turbidity with the reduction polarity across the solvents was observed for the ES-CNC3 sample dispersions. This modified samples disperse well in the least non-polar solvent (toluene), indicating good nanoparticle/solvent compatibility. This result is in agreement with the WCA study, indicating that the modified CNC could have good dispersibility in non-polar polymers such as PU. **Figure 4.5b** also compared the dispersibility of native CNC and ES-CNC3 in castor oil polyol, which was part A of the polyurethane coating formulation. The results showed that the modified CNC forms excellent dispersion in castor oil, and as such their composites in PU could produce appealing properties as the dispersion of nanoparticles in composite materials is critical to obtain good physical and other functional properties.

4.3.3 Nanocomposite coating

4.3.3.1 Morphology

It has been proved that the modification of CNC with ES reduces the polarity that results to improved dispersibility in non-polar mediums such as castor oil polyol. Therefore, it is expected that the modified CNC will disperse well in the PU matrix. **Figure 4.6** shows the SEM images of cross-sectional fractured surfaces of PU, PU/3% CNC and PU/ES-CNC3. The neat PU (**Figure 4.6a**) exhibits a smooth and homogeneous surface similar to that found in previous studies

[199,200]. The incorporation of hydrophilic CNC in non-polar PU matrix (**Figure 4.6b**) led to the aggregation and formation of microparticles (white dots) due to matrix/nanofiller incompatibility. Furthermore, it was observed that the addition of CNC caused the creation of substantial amounts of voids and air pockets along the PU/CNC interfaces. Contrarily, SEM images of PU/ES-CNC3 nanocomposite (**Figure 4.6c and 5c-1**) revealed less aggregates and more homogenous distribution of the modified CNC nanoparticles across the PU matrix. Typically, nanofillers such as carbon nanotubes, carbon fibres and graphite nanoplatelet are functionalized in order to obtain good dispersions and strong interfacial interactions with polymers [201,202]. In this research, the good distribution of modified CNC in PU polymer matrix can be attributed to the functionalization of CNC surface leading to improved interaction between the filler and polymer, and hence strong interfacial adhesion. The good dispersion and uniform distribution of epoxide functionalized silane treated CNC has the potential to improve the overall mechanical and barrier properties of PU coating as presented in the subsequent sections.

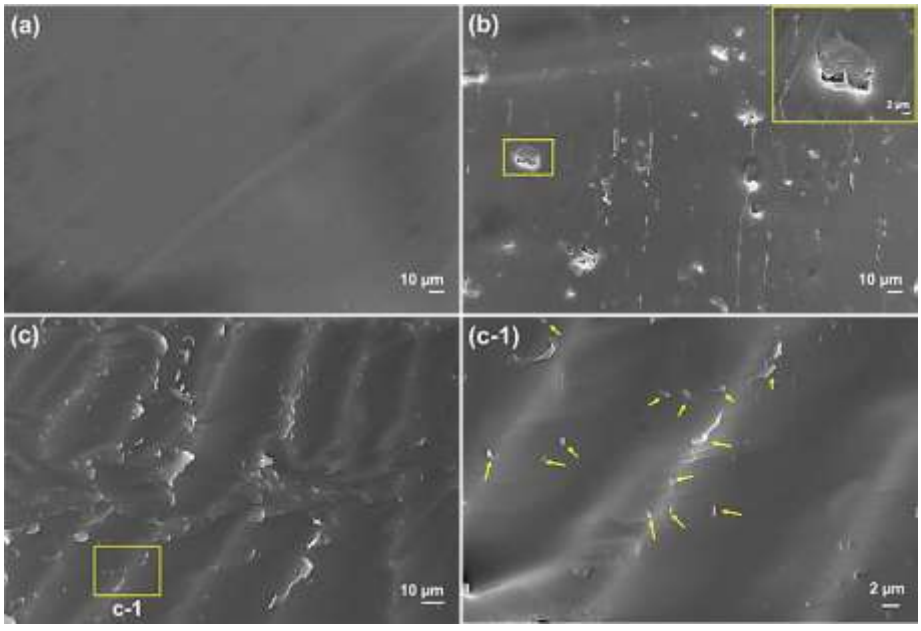

Figure 4.6. SEM images of (a) PU (b) PU/3% CNC and (c) PU/3% ES-CNC3. The insert in (b) is its high resolution and (c-1) is the high resolution of (c).

4.3.3.2 Dynamic Mechanical Analysis (DMA)

DMA was used to evaluate the effect of CNC and modified CNC on thermo-mechanical properties of the PU nanocomposites. **Figure 4.7** shows the storage modulus and tan delta curves acquired from DMA of PU, PU/CNC and PU/ES-CNC3 composites at various concentrations of CNC and modified CNC. For composites containing 1 and 3 wt. % of CNC (**Figure 4.7a**), the storage modulus was higher in comparison to that of PU polymer. At 5 wt. % loading of CNC, there was a decrease in storage modulus, which was attributed to the aggregation of CNC at higher loading leading to poor interfacial interaction with the PU matrices and thus decreasing in its modulus. However, the modulus was observed to increase for PU/ES-CNC3 nanocomposites for all wt. % loading, as compared to PU/CNC (**Figure 4.7b**). The enhancement in moduli can be ascribed to the restriction of chain mobility of the PU due to the presence of hard nanofillers [143,203]. Moreover, the dispersion and interfacial interaction of ES-CNC within the PU matrix led to the increase in dynamic modulus of the PU nanocomposites [204]. It should be noted that there was a decrease in the modulus of nanocomposite at 5 wt. % loading of modified CNC (**Figure 4.7c**) at 55 ^{o}C; however, the modulus was still over 1000 MPa higher that that of PU/5% CNC. This result facilitates that the better dispersion of CNC from the functionalization of its surfaces can enhance its reinforcing properties in PU matrices. The high modulus of the ES-CNC3 based PU nanocomposite coating is an indirect indicator that the nanocomposite coating has good physical properties such as scratch, marring, abrasion, and dent resistance as compared to the unfilled PU coating.

The addition of low loading (1 and 3 wt. %) of both CNC and ES-CNC3 into PU matrix did not affect the glass transition temperature (T_g) of the nanocomposite as demonstrated by the similar tan delta peaks (**Figure 4.7d-e**). A shift in the T_g of the PU nanocomposites towards a

higher temperature with the incorporation of higher loadings (5 wt. %) of both native CNC and modified CNC was observed in **Figure 4.7f**. However, an 18 ºC tan delta peak shift of the PU/ES-CNC nanocomposite is observed as compared to that of PU and by 8 ºC as compared to PU/CNC at the same filler loading concentration. Based on the TGA studies, native and ES-CNCs have very high decomposition temperatures and are expected to largely preserve their crystallinity near the PU's T_g (37 ºC). Thus, it is logical that their incorporation in the PU nanocomposite increases the T_g as compared to the neat PU matrix.

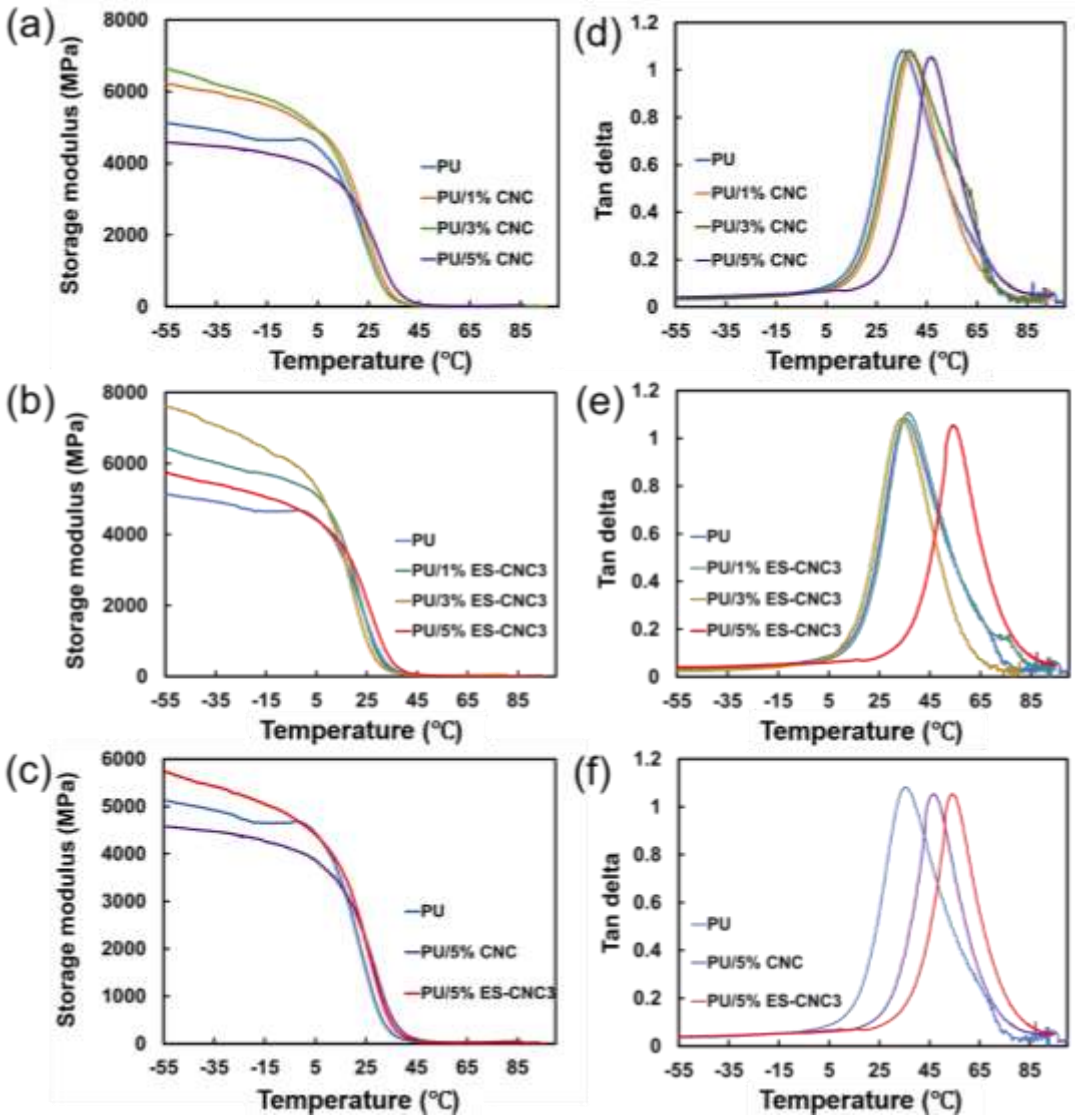

Figure 4.7. Storage modulus of (a) PU and PU/CNC composites (b) PU/ES-CNC3 composites at different nanofiller content. (c) is the comparison of the storage modulus of PU and PU composites containing 5% CNC and 5% ES-CNC3. (d-e) are tan delta of PU and various PU/CNC and PU/ES-CNC composites. (f) shows the comparison of the tan delta of PU and PU composites containing 5% CNC and 5% ES-CNC3.

4.3.3.3 Water absorption test

PU is an engineering polymer that is extensively utilized in many industrial applications ranging from coatings, composites, leather to adhesives [205]. However, PU suffers from poor moisture barrier properties because the residual polar groups on the crosslinked structure such as secondary amine, carbonyl and urethanes. These functional groups allow for the association with water molecules and the water is able to penetrate through the matrix that eventually leads to deterioration of its properties [112]. **Figure 7a** shows the water absorption for neat PU, PU/CNC composite and PU/ES-CNC3 nanocomposite at various filler loadings for 14 days (336 h). For PU/CNC composites, the water absorbance increases with an increase in CNC loading level. On the other hand, the results showed that nanocomposite of PU containing ES-CNC3 reduced the water absorbance substantially as compared to that of the neat PU and PU/CNC. The 5% wt. ES-CNC3-based nanocomposite exhibited the lowest water uptake.

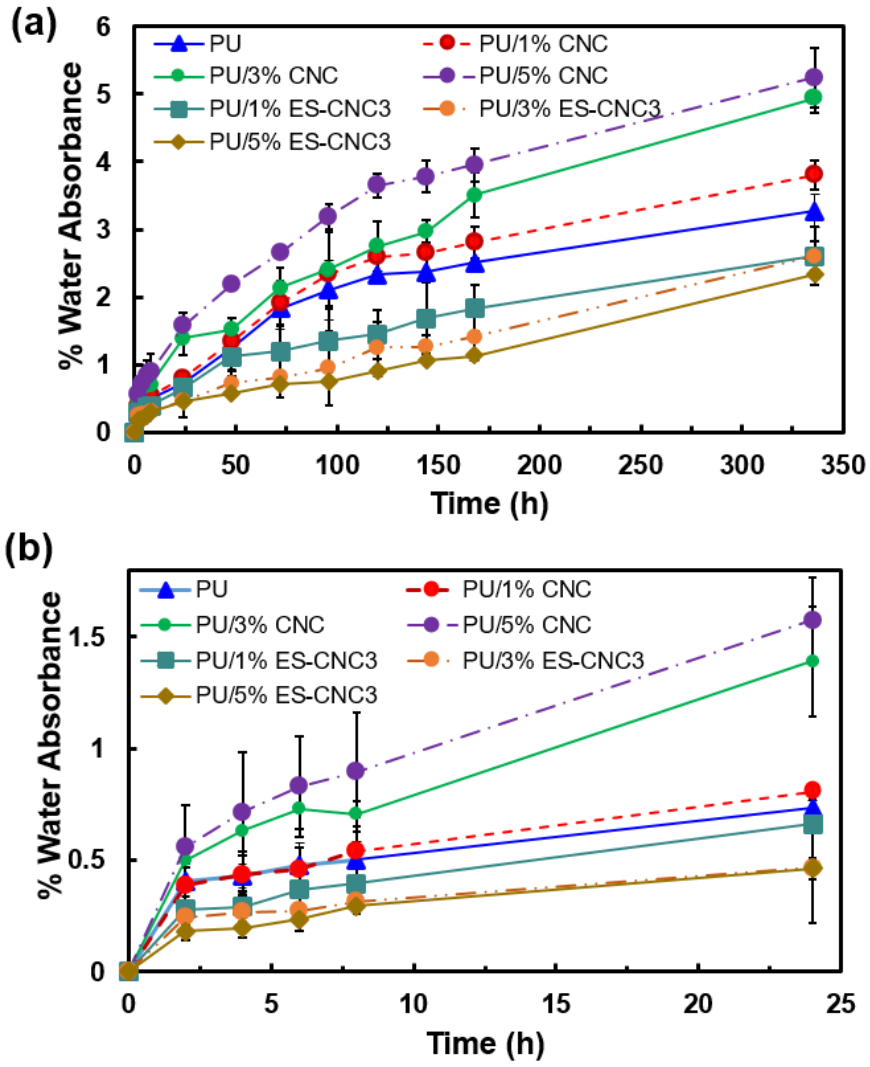

Figure 4.8. Water absorbance of PU and PU composites as a function of time for (a) 336 h and (b) 24 h.

Figure 7b illustrates the result for the first 24 h of the water absorption test. In this small-time window, PU/ES-CNC3 composite was already observed to have lower water absorbance compared to PU and PU/CNC. Two factors could be contributed to the reduction in water absorption of the PU/ES-CNC3 nanocomposites; free volume in the nanocomposites and the amount of polar functional groups in polymer matrix [206]. First, the hydrophobic modifications of CNC have converted the abundant hydrophilic -OH group on the surface of CNC to O-Si-O bonds. Such reduction in the polar functional group of CNC contributed to the scaling down of PU

nanocomposites from trapping water molecules and permeation into the polymer matrix. Secondly, the free volume in the PU matrix is reduced due to the volume occupied by the well-dispersed modified CNC in the PU matrix.

4.3.3.4 Salt spray test

One of the main applications of polyurethane is coatings for metal substrates protection from corrosion. Nanofillers are widely used to improve water and corrosive molecules impermeability in polymeric coatings [207]. Salt spray tests are typically employed to evaluate the preliminary anticorrosion performance of organic coatings. In this study, salt spray test was carried out on steel panels coated with PU and PU composites with CNC and ES-CNC3 at different nanofiller loading concentration using neutral 5% NaCl solution with an "x" pattern scratched on the surface. The corrosion progress on the scratched area of the metal as a result of the salt spraying over 25 days of observation is presented in **Figure 4.9**. The images reveal some rusting occurring on all steel panels after 5 days of salt spraying, with no significant difference in the degree of rusting between PU, PU/CNC, and PU/ES-CNC3 nanocomposites.

However, PU (**Figure 4.9a**) and PU/CNC (**Figure 4.9 b-d**) started to display increased degree of corrosion as compared to PU/ES-CNC3 (**Figure 4.9 e-g**) after 10 days. Moreover, an increasing degree of rusting with an increase in the loading concentration of native CNC was observed. By day 25, clear results indicating that the PU/ES-CNC provide better anticorrosive resistance for metals substrates as compared to PU and PU/CNC was observed. While PU and PU/CNC coating progressively blistered and peeled off from the metal substrate as rusting began (day 5), the PU/ES-CNC3 coatings remained intact over the 25 days spraying and observation period. The peeling was indicative of the loss of interfacial adhesion between coatings and the

metal substrates as a result of moisture and corrosive salt molecules penetration through the coatings resulting in flaky iron oxide formation.

The excellent anticorrosion of the PU nanocomposites could be emanating from the enhancement in the adhesion of the PU/ES-CNC3 coating to the metal substrate and good dispersion and distribution of the hydrophobically modified CNC (ES-CNC3) in the PU coating. The well-dispersed and highly crystalline modified CNC are impenetrable by either moisture or corrosion molecules, which substantially increases the tortuous path and delays the mobility of corrosive molecules through the coating to reach to the metal substrate and cause corrosion. Furthermore, the possible reaction between the epoxide functional groups of ES on the surface of CNC and the isocyanates, which was used here as the curing agent of the polyol, could form a stable heterocycle linkages within the PU matrix [208]. Such bonding of the CNC filler with the PU enhances the stability and barrier properties of the coating.

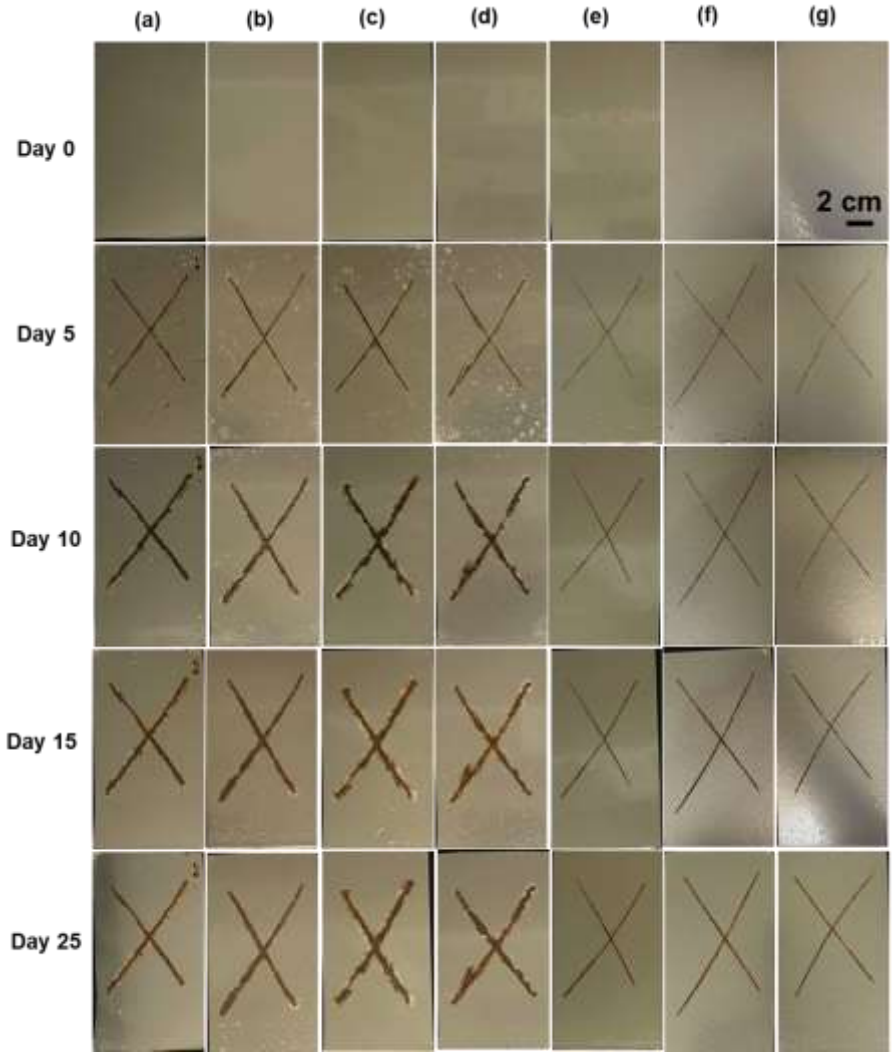

Figure 4.9. Photographic images of salt spray tests of steel panels coated with (a) PU (b-d) PU/1% CNC, PU/3% CNC and PU/5% CNC. (e-g) are 1, 3, 5% of ES-CNC3 incorporated into PU coating.

4.3.3.5 Electrochemical impendence spectroscopy (EIS)

From the salt spray test analysis, it was observed that PU/ES-CNC3 nanocomposite coatings provided corrosion prevention to the steel substrates. Electrochemical impendence spectroscopy (EIS) was used here to evaluate the anticorrosion behaviour of the nanocomposites quantitatively. It should be noted here that a lower loading of the modified CNC (3 wt. % ES-CNC3 over the 5 wt. %) was selected for the EIS study partly because the salt spray test did not

show major difference between the two coating formulations and also to avoid cost-prohibition from the cost of CNC for industrial applications. **Figure 4.10 (a and b)** present the Nyquist plots of 1 h and 3 h immersion times from the EIS in 3.5 wt. % NaCl aqueous solution of: the control (bare metal), PU and PU/1% ES-CNC3 and PU/3% ES-CNC3 nanocomposite samples. It was observed that the capacitive loop of all samples decreased with an increase in the immersion time from 1 to 3 h. The decrease in impendence (-Z") at 3 h was associated with the initiation of corrosion activity on metal surfaces from the corrosive medium [209]. The large magnitude loops, associated with PU/ES-CNC3 nanocomposites, indicated the excellent barrier property of the coating that prevented progressive corrosion on the steel surface as compared to the other coatings [210]. PU coatings that contained 3% ES-CNC3 produced the largest capacitive loop from EIS, indicating that it provides the best corrosion resistance among the studied coating samples. **Figure 4.10 (a-1, b-1)** showed that PU/1% ESCNC loop magnitude is approximately three orders of magnitude greater than the PU coating in both 1 and 3 h immersion times in NaCl solution.

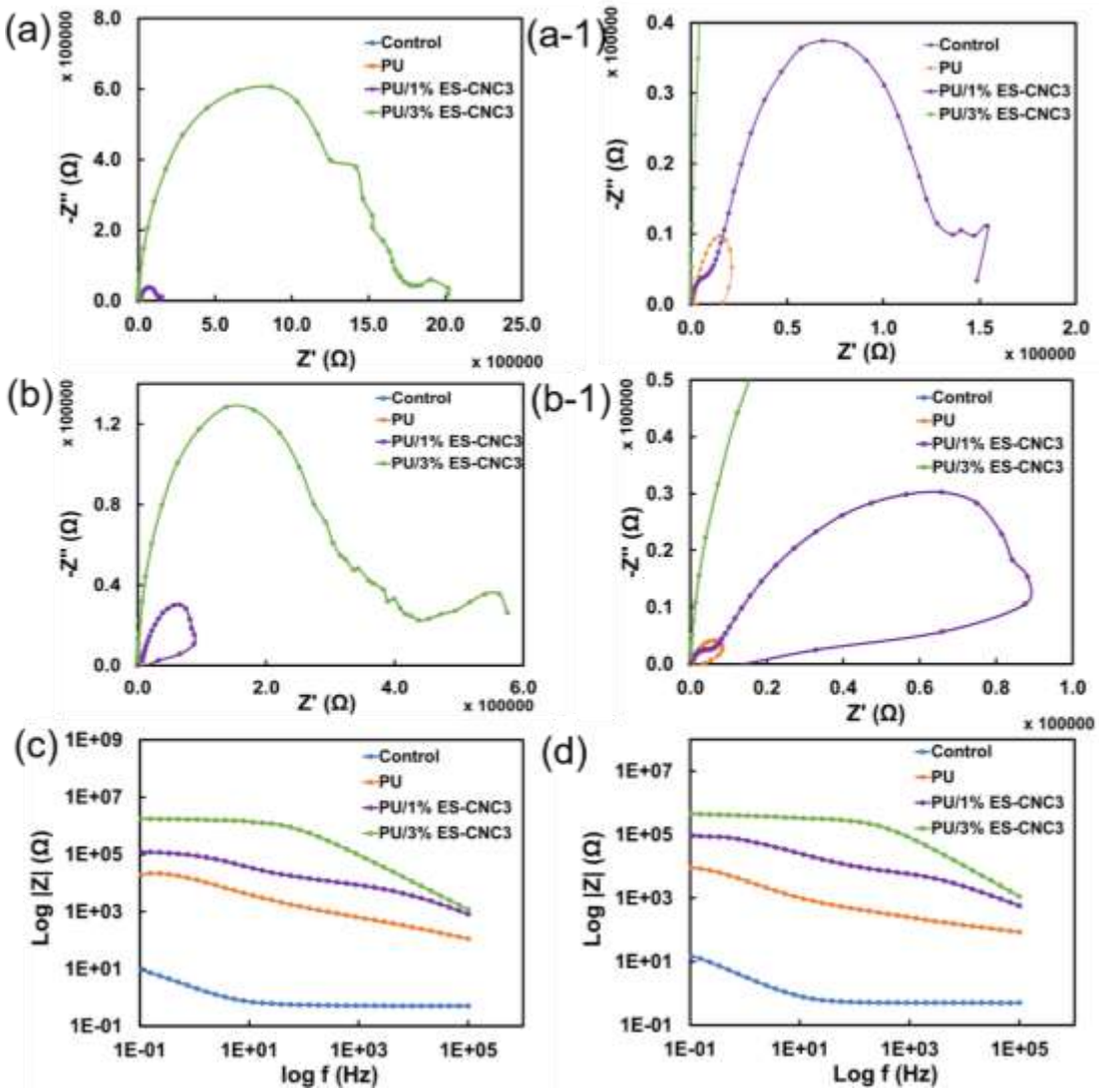

Figure 4.10. Nyquist of various PU and PU nanocomposites at immersion times of (a) 1 h and (b) 3 h. (a-1) and (b-1) are the zoomed-in sections of (a) and (b), respectively, (c and d) are Bode plots of various coatings at immersion times of 1 and 3 h, respectively.

The Bode diagrams shown in **Figure 4.10 (c, d)** provided an insight of the impendence module of EIS for 1 and 3 h immersion times. At lower frequencies, the impendence of PU/1% ES-CNC3 and PU/3% ES-CNC3 in 1 h and 3 h immersion times remained stable, which indicated that these coatings have barrier properties and did not allow penetration of the electrolyte molecules. As the frequency increased further, the impendence started to decrease, indicating the

penetration of electrolytes through the coatings. The PU coating without a filler displayed a uniform reduction in Log |Z| even at lower frequencies while that of the bare steel decreased rapidly and reached the saturation points the fastest. As expected, the fast saturation of the bare metal substrate was because of the fast diffusion of the electrolytes to the metal surface due to the lack of protective coating that led to delamination of the metal layers[109]. The 3 h immersion time **(Figure 4.10d**)showed similar results to the 1 h immersion time with the PU/3% ES-CNC3 coated substrates providing the best protection of the steel plates against corrosion. Furthermore, the impendence values from Bode plots coincide well with the Nyquist plot that prolonging the immersion time in NaCl solution could deteriorate the protective performance of coatings as observed by the decrease in the magnitude of Log |Z| of all samples.

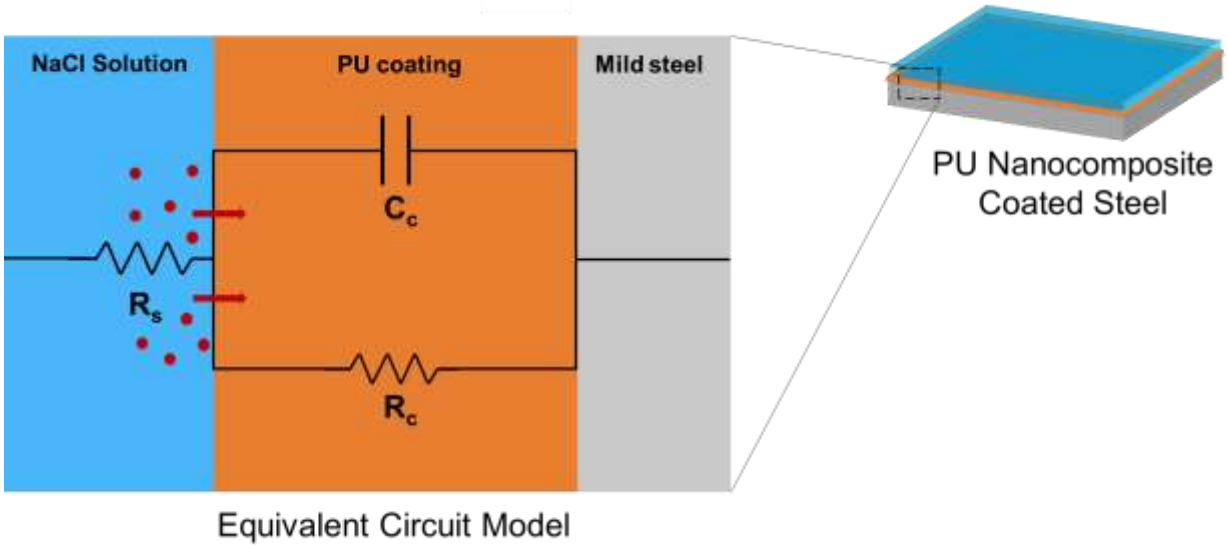

Figure 4.11. Equivalent circuit model used for fitting EIS data of organic coatings. ($R_{s,}$-solution resistance R_c-coating resistance and C_c-coating capacitance)

Equivalent circuit models were fitted with EIS data to obtain coating resistance (R_c) and coating capacitance (Cc) parameters of the organic coatings. Typically, a high magnitude of R_c in coatings indicates high anticorrosion performance, and the R_c generally decreases with an increase in immersion time due to the penetration of corrosive ion and water molecules [109,211].

Contrarily, C_c values provide an insight into the relative ion uptake rate into coating systems [109]. From the Nyquist plots, one capacitive loop is observed, which indicated that the one-time constant equivalent circuit model (**Figure 4.11)** can plausibly describe the corrosion of metal surfaces in short immersion times (1 and 3 h). In this model, the barrier coatings used in this study remained intact without any delamination occurrence [112]. **Table 4.3** lists the parameters fitted using EC-lab software and model in **Figure 4.11**. The comparison shows that PU/3% ES-CNC3 has the highest R_c (5.99E+04 $k\Omega \cdot cm^2$) and lowest C_c (4.37E-05 $\mu F \cdot cm^{-2}$) values as compared to those of the other coatings. These results validate that this nanocomposite coating is the best protective organic coating with the lowest rate of ion uptake through the coatings of the all coatings studied. Furthermore, R_c decreased in all tested samples when the immersion time was prolonged to 3 h. However, there was no significant change in the rate of ion uptake between 1 and 3 h as the time increment was not substantially large. Using the fitting model, the outcomes coincided with Nyquist and Bode plot that PU containing 3% of ES-CNC3 performed the best in protecting steel from corrosion.

Table 4.3. Electrochemical parameters of the equivalent circuit for uncoated (control) and different organic coated carbon steel specimens immersed at different times in 3.5% NaCl solution.

Sample	Immersion time (h)	R_c ($k\Omega \cdot cm^2$)	C_c ($\mu F \cdot cm^{-2}$)
Control	1	2.71E-01	2.10E+03
	3	2.97E-01	1.20E+03
	1	1.48E+02	3.12E-02

PU	3	1.12E+02	2.39E-04
PU/1% ES-CNC3	1	4.71E+02	1.35E-04
	3	1.42E+02	1.34E-04
PU/3% ES-CNC3	1	5.99E+04	4.37E-05
	3	1.37E+04	4.46E-05

4.4 Conclusions

In this work, CNC was hydrophobically modified with ES to improve its dispersion in PU polymer and enhance the corrosion inhibition performance. Through optimization of the reaction time and molar ratio of ES to CNC, the most-modified sample was determined to be ES-CNC3 (12 h and 5:1 ratio). The ES-CNC3 sample exhibited good thermal stability with a peak degradation temperature of 460º as compared to 312º for the native CNCs. Likewise, the ES-CNC3 sample displayed high-water contact angle and good dispersibility in non-polar solvents such as THF and toluene as well as castor oil polyol. The hydrophobicity of the modified CNC translated well into good dispersibility in PU coatings as noted from SEM imaging. Salt spray and EIS tests provided clear evidence that PU nanocomposite fabricated with the modified CNC provided significantly improved corrosion protection to steel. This shows great potential for use on other corrosion sensitive materials as well. The corrosion protection of the coatings was more pronounced at higher ES-CNC3 loading (3 wt. %). This is because the highly dispersed ES-CNC3 in PU creates a tortuous path against the diffusion of moisture and ions, which in effect provides corrosion protection. Beyond the specific results demonstrated here, CNC silanization provides a

facile and green process, which could easily be extended towards the development of other CNC based thermoplastic and thermosetting polymer composites. Furthermore, our approach is generic enough that other hydrophobic modifications can be implemented for a wide range of nanomaterials for corrosion protective coatings or other structural and functional nanocomposites.

Chapter 5. Concluding remarks and recommendations

Polymer coatings are widely used in many applications including construction, marine and manufacturing products. CNCs, which are biodegradable and sustainable, are exceptional fillers for the fabrication of polymer nanocomposite due to their low density, high aspect ratio, high mechanical strength, good thermal stability and its extensive availability in nature. However, the addition of CNCs into polymer coatings present a challenge because CNC contain -OH hydroxyl on its surface, making them susceptible to moisture absorption and aggregation in non-polar matrices such as epoxy and polyurethane. Here in this thesis, CNCs have been successfully modified without a major crystallinity change and incorporated into epoxy and polyurethane matrices for coating and multifunctional applications. Two distinguished routes of chemical modification of surface CNC were investigated.

In the first part of this work, CNC was modified with three different kinds of ammonium cationic surfactants (CTAB, DDAB, DHAB) through a three-step process. This involved oxidizing the CNC with a TEMPO catalyst, followed by deprotonation of the oxidized CNCs, and finally the adsorptions of the surfactants onto the deprotonated CNCs through electrostatic interaction. All three different surfactant modified CNC were shown to be more hydrophobic and dispersible than unmodified CNC in non-polar solvents, such as THF. However, the WCA of modified CNC, with optimization, could only be maximized up to 56.6º. This suggested that using surfactant as a modifying agent was not the best option for synthesizing highly hydrophobic CNC. The three types of surfactant-modified CNCs were also incorporated into epoxy to form nanocomposite coating on mild steel substrates together with native CNC and unfilled epoxy-based control coating formulations. Salt spray test and electrochemistry showed that the epoxy nanocomposite that contained DDAB modified CNC provide the best corrosion protection as compared to the other

two surfactant-modified CNCs (DDAB-oCNC, DHAB-oCNC) as well as the control formulations. A conclusion was drawn that DDAB has medium alkyl chain length that was hydrophobic enough to surrender CNC from self-association, but their chain length was not extremely long to cause self-entanglement and disruption in the epoxy matrices. Overall, the surfactant modification improved the dispersibility of CNC in epoxy, due to the increase in the hydrophobicity that resulted in an enhanced dispersibility of the nanoparticle in the epoxy. However, the choice of surfactant (chain length) used for CNC modification should be taken into account when utilizing these modified fillers in polymer nanocomposites.

In the second work, CNC was hydrophobically modified with ES to improve dispersion in PU polymer. Through optimization of the reaction time and molar ratio of ES: CNC, the best-modified sample was determined to be ES-CNC3 (12 h and 5:1 ratio). The ES-CNC3 sample have good thermal stability with a peak degradation temperature of 460º compared to 312º of unmodified CNC. Likewise, the ES-CNC3 sample displayed a relatively high hydrophobicity with high water contact angle and good dispersibility in non-polar solvents such as THF and toluene. Salt spray test and EIS testing provided clear evidence that PU nanocomposite composites fabricated with the modified CNC provided great corrosion protection to steel and potentially other metals. The corrosion protection of the coatings was more pronounced at higher ES-CNC3 loading (3 vs. 1 wt. %) for both 1 and 3 h immersion time in NaCl solution. Future work could focus on a long-term EIS study of these PU nanocomposites coating in more harsh conditions such as high temperature, high acidity and basicity for a better understanding of the anticorrosion performances of these coating. Beyond the specific results demonstrated here, CNC silanization in this study provides a facile and green process, which could easily be extended to develop other CNC based thermoplastic and thermosetting polymer composites.

References

[1] S. Sharma,, P. Nagar,, I.S. Sodhi, Governometrics and technological innovation for public policy design and precision, IGI Global, 2014.

[2] P. Panchal,, E. Ogunsona,, T. Mekonnen, Processes 7(1) (2018) 10. 10.3390/pr7010010.

[3] X. Xu,, F. Liu,, L. Jiang,, J.Y. Zhu,, D. Haagenson,, D.P. Wiesenborn, ACS Appl. Mater. Interfaces 5(8) (2013) 2999–3009. 10.1021/am302624t.

[4] S. Zhou,, T. You,, X. Zhang,, F. Xu, ACS Appl. Nano Mater. 1(5) (2018) 2095–103. 10.1021/acsanm.8b00079.

[5] Y. He,, Y. Boluk,, J. Pan,, A. Ahniyaz,, T. Deltin,, P.M. Claesson, J. Dispers. Sci. Technol. 0(0) (2019) 1–11. 10.1080/01932691.2019.1647229.

[6] C. Dorrer,, J. Rühe, Soft Matter 5(1) (2009) 51–61. 10.1039/B811945G.

[7] H. Yang,, P. Jiang, Langmuir 26(15) (2010) 12598–604. 10.1021/la1021643.

[8] L. Cao,, A.K. Jones,, V.K. Sikka,, J. Wu,, D. Gao, Langmuir 25(21) (2009) 12444–8. 10.1021/la902882b.

[9] A. Marmur*, (2004). 10.1021/LA036369U.

[10] X.-M. Li,, D. Reinhoudt,, M. Crego-Calama, (2007). 10.1039/b602486f.

[11] J. Song,, O.J. Rojas, Nord. Pulp Pap. Res. J. 28(2) (2013) 216–38. 10.3183/npprj-2013-28-02-p216-238.

[12] A. Solga,, Z. Cerman,, B.F. Striffler,, M. Spaeth,, W. Barthlott, Bioinspir. Biomim. 2(4) (2007) S126–34. 10.1088/1748-3182/2/4/S02.

[13] Y. Lee,, Y. Yoo,, J. Kim,, S. Widhiarini,, B. Park,, H.C. Park,, K.J. Yoon,, D. Byun, J. Bionic Eng. 6(4) (2009) 365–70. 10.1016/S1672-6529(08)60130-4.

[14] and T.R.L. Yuan, Y., Contact angle and wetting properties, Vol. 1, 2015.

[15] † Taolei Sun,, ‡ Lin Feng,, § and Xuefeng Gao,, †,§ Lei Jiang*, (2005). 10.1021/AR040224C.

[16] V.A. Ganesh,, H.K. Raut,, A.S. Nair,, S. Ramakrishna, (n.d.). 10.1039/c1jm12523k.

[17] S. Xie,, X. Zhang,, M.P. Walcott,, H. Lin, Eng. Sci. (2018) 4–16. 10.30919/es.1803302.

[18] H. Kargarzadeh,, M. Mariano,, J. Huang,, N. Lin,, I. Ahmad,, A. Dufresne,, S. Thomas, Polymer (Guildf). 132 (2017) 368–93. 10.1016/j.polymer.2017.09.043.

[19] D.Y. Kwok,, A.W. Neumann, Adv. Colloid Interface Sci. 81(3) (1999) 167–249. 10.1016/S0001-8686(98)00087-6.

[20] J. Genzer,, K. Efimenko, (2007). 10.1080/08927010600980223.

[21] T. Nishino,, M. Meguro,, K. Nakamae,, M. Matsushita,, Y. Ueda, Langmuir 15(13) (1999) 4321–3. 10.1021/la981727s.

[22] W.M. Sigmund,, S. Hsu, Encycl. Membr. (1936) (2015) 1–2. 10.1007/978-3-642-40872-4.

[23] N. Dalali,, P. Separation, Encyclopedia of Membranes, 2016.

[24] M. Nosonovsky,, R. Ramachandran, Entropy 17(7) (2015) 4684–700. 10.3390/e17074684.

[25] N.J. Shirtcliffe,, G. McHale,, S. Atherton,, M.I. Newton, Adv. Colloid Interface Sci. 161(1–2) (2010) 124–38. 10.1016/J.CIS.2009.11.001.

[26] T.A. Dankovich,, D.G. Gray, J. Adhes. Sci. Technol. 25(6–7) (2010) 699–708. 10.1163/016942410X525885.

[27] A. Nakajima,, K. Abe,, K. Hashimoto,, T. Watanabe, Thin Solid Films 376(1–2) (2000) 140–3. 10.1016/S0040-6090(00)01417-6.

[28] Y.-T. Cheng,, D.E. Rodak, Appl. Phys. Lett. 86(14) (2005) 144101. 10.1063/1.1895487.

[29] T. Sun,, L. Feng,, X. Gao,, L. Jiang, Acc. Chem. Res. 38(8) (2005) 644–52. 10.1021/ar040224c.

[30] K. Liu,, M. Zhang,, J. Zhai,, J. Wang,, L. Jiang, Appl. Phys. Lett. 92(18) (2008) 183103. 10.1063/1.2917463.

[31] Z. Guo,, W. Liu, Plant Sci. 172(6) (2007) 1103–12. 10.1016/j.plantsci.2007.03.005.

[32] X.Q. Feng,, X. Gao,, Z. Wu,, L. Jiang,, Q.S. Zheng, Langmuir 23(9) (2007) 4892–6. 10.1021/la063039b.

[33] V.F. Cardoso,, D.M. Correia,, C. Ribeiro,, M.M. Fernandes,, S. Lanceros-Méndez, Polymers (Basel). 10(2) (2018) 1–26. 10.3390/polym10020161.

[34] M. Ma,, R.M. Hill, Curr. Opin. Colloid Interface Sci. 11(4) (2006) 193–202. 10.1016/j.cocis.2006.06.002.

[35] S.G. Lee,, D.S. Ham,, D.Y. Lee,, H. Bong,, K. Cho, (2013). 10.1021/la404005b.

[36] J. Lin,, C. Zheng,, W. Ye,, H. Wang,, D. Feng,, Q. Li,, B. Huan, J. Appl. Polym. Sci. 132(1) (2015). 10.1002/app.41458.

[37] Z.J. Wei,, W.L. Liu,, D. Tian,, C.L. Xiao,, X.Q. Wang, Appl. Surf. Sci. 256(12) (2010) 3972–6. 10.1016/j.apsusc.2010.01.059.

[38] M. Ramezani,, M.R. Vaezi,, A. Kazemzadeh, Appl. Surf. Sci. 317 (2014) 147–53. 10.1016/j.apsusc.2014.08.095.

[39] S. Yuan,, S.O. Pehkonen,, B. Liang,, Y.P. Ting,, K.G. Neoh,, E.T. Kang, Corros. Sci. 53(9) (2011) 2738–47. 10.1016/j.corsci.2011.05.008.

[40] U. Eduok,, O. Faye,, J. Szpunar, Prog. Org. Coatings 111(June) (2017) 124–63.

10.1016/j.porgcoat.2017.05.012.

[41] L. Li,, B. Li,, J. Dong,, J. Zhang, J. Mater. Chem. A (2016) 13677–725. 10.1039/c6ta05441b.

[42] S. Jia,, M. Liu,, Y. Wu,, S. Luo,, Y. Qing,, H. Chen, Appl. Surf. Sci. 386 (2016) 115–24. 10.1016/j.apsusc.2016.06.004.

[43] Z. Yang,, L. Wang,, W. Sun,, S. Li,, T. Zhu,, W. Liu,, G. Liu, Appl. Surf. Sci. 401 (2017) 146–55. 10.1016/j.apsusc.2017.01.009.

[44] F. De Nicola,, P. Castrucci,, M. Scarselli,, F. Nanni,, I. Cacciotti,, M. De Crescenzi, Nanotechnology 26(14) (2015). 10.1088/0957-4484/26/14/145701.

[45] D. Ebert,, B. Bhushan, (2012). 10.1021/la301479c.

[46] S. Nishimoto,, H. Sekine,, X. Zhang,, Z. Liu,, K. Nakata,, T. Murakami,, Y. Koide,, A. Fujishima, Langmuir 25(13) (2009) 7226–8. 10.1021/la9011372.

[47] Y. Lu,, S. Sathasivam,, J. Song,, F. Chen,, W. Xu,, C.J. Carmalt,, I.P. Parkin, J. Mater. Chem. A 2(30) (2014) 11628–34. 10.1039/c4ta02181a.

[48] D. Choi,, J. Yoo,, S.M. Park,, D.S. Kim, Appl. Surf. Sci. 393 (2017) 449–56. 10.1016/j.apsusc.2016.10.057.

[49] B. Qian,, Z. Shen, Langmuir 21(20) (2005) 9007–9. 10.1021/la051308c.

[50] S. Zhang,, X. Zeng,, D.T.A. Matthews,, A. Igartua,, E. Rodriguez-Vidal,, J. Contreras Fortes,, V. Saenz de Viteri,, F. Pagano,, B. Wadman,, E.D. Wiklund,, E. van der Heide, Friction 4(2) (2016) 89–104. 10.1007/s40544-016-0115-9.

[51] T. Rezayi,, M.H. Entezari, J. Colloid Interface Sci. 463 (2016) 37–45. 10.1016/J.JCIS.2015.10.029.

[52] Y. Huang,, D.K. Sarkar,, X. Grant Chen, Appl. Surf. Sci. 356 (2015) 1012–24. 10.1016/J.APSUSC.2015.08.166.

[53] P. Nguyen-Tri,, F. Altiparmak,, N. Nguyen,, L. Tuduri,, C.M. Ouellet-Plamondon,, R.E. Prud'Homme, ACS Omega 4(4) (2019) 7829–37. 10.1021/acsomega.9b00688.

[54] J. Tam,, G. Palumbo,, U. Erb, Materials (Basel). 9(3) (2016) 151. 10.3390/ma9030151.

[55] Q. Zhang,, Q. Wang,, S. Zhang,, X. Lu,, X. Zhang, ChemPhysChem 17(3) (2016) 335–51. 10.1002/cphc.201500713.

[56] Q. Liu,, D. Chen,, Z. Kang, ACS Appl. Mater. Interfaces 7(3) (2015) 1859–67. 10.1021/am507586u.

[57] Y. Xia,, G.M. Whitesides, Annu. Rev. Mater. Sci. 28(1) (1998) 153–84. 10.1146/annurev.matsci.28.1.153.

[58] D. Zhang,, H. Qian,, L. Wang,, X. Li, Corros. Sci. 103 (2016) 230–41. 10.1016/J.CORSCI.2015.11.023.

[59] F. Wang,, S. Li,, L. Wang, Colloids Surfaces A Physicochem. Eng. Asp. 513 (2017) 389–95. 10.1016/j.colsurfa.2016.11.001.

[60] C.J. Weng,, C.H. Chang,, C.W. Peng,, S.W. Chen,, J.M. Yeh,, C.L. Hsu,, Y. Wei, Chem. Mater. 23(8) (2011) 2075–83. 10.1021/cm1030377.

[61] S.Y. Chou,, P.R. Krauss,, P.J. Renstrom, J. Vac. Sci. Technol. B Microelectron. Nanom. Struct. 14(6) (1996) 4129. 10.1116/1.588605.

[62] B. Brady,, P.H. Wang,, V. Steenhoff,, A.G. Brolo, Metal Nanostructures for Photonics, Elsevier, 2019, pp. 197–221.

[63] Y.H. Sung,, Y.D. Kim,, H.J. Choi,, R. Shin,, S. Kang,, H. Lee, Appl. Surf. Sci. 349 (2015) 169–73. 10.1016/j.apsusc.2015.04.141.

[64] M. Ma,, Y. Mao,, M. Gupta,, K.K. Gleason,, G.C. Rutledge, (2005). 10.1021/ma0511189.

[65] N. Nuraje,, W.S. Khan,, Y. Lei,, M. Ceylan,, R. Asmatulu, (n.d.). 10.1039/c2ta00189f.

[66] L. Jiang,, Y. Zhao,, J. Zhai, Angew. Chemie - Int. Ed. 43(33) (2004) 4338–41. 10.1002/anie.200460333.

[67] K. Acatay,, E. Simsek,, C. Ow-Yang,, Y.Z. Menceloglu, Angew. Chemie - Int. Ed. 43(39) (2004) 5210–3. 10.1002/anie.200461092.

[68] Z. Liu,, H. Wang,, E. Wang,, X. Zhang,, R. Yuan,, Y. Zhu, Polymer (Guildf). 82 (2016) 105–13. 10.1016/j.polymer.2015.11.045.

[69] X. Wang,, B. Ding,, J. Yu,, M. Wang, Nano Today 6 (2011) 510–30. 10.1016/j.nantod.2011.08.004.

[70] Ameer,, PR,, Kasoju, J. Funct. Biomater. 10(3) (2019) 30. 10.3390/jfb10030030.

[71] A.B. Radwan,, A.M.A. Mohamed,, A.M. Abdullah,, M.A. Al-Maadeed, Surf. Coatings Technol. 289 (2016) 136–43. 10.1016/J.SURFCOAT.2015.12.087.

[72] R.K. Singh,, F. Foroutan,, M. Alqaysi,, C.-M. Han, J. Prog. Mater. Sci. 77 (2016) 1–79. 10.1016/j.pmatsci.2015.12.001.

[73] S. Thiagarajan,, A. Sanmugam,, D. Vikraman, Recent Applications in Sol-Gel Synthesis, InTech, 2017, p. .

[74] Y. Tang,, Q. Zhang,, X. Zhan,, F. Chen, Soft Matter 11(22) (2015) 4540–50. 10.1039/c5sm00674k.

[75] C. Sanchez,, P. Belleville,, M. Popall,, L. Nicole, Chem. Soc. Rev. 40(2) (2011) 696. 10.1039/c0cs00136h.

[76] S. Liu,, X. Liu,, S.S. Latthe,, L. Gao,, S. An,, S.S. Yoon,, B. Liu,, R. Xing, Appl. Surf. Sci. 351 (2015) 897–903. 10.1016/j.apsusc.2015.06.016.

[77] A.C. Jones,, M.L. Hitchman, R. Soc. Chem. (2009) 1–36. 10.1039/9781847558794.

[78] Q. Zhang,, D. Sando,, V. Nagarajan, J. Mater. Chem. C 4(19) (2016) 4092–124. 10.1039/c6tc00243a.

[79] Q. Shang,, Y. Zhou, Ceram. Int. 42(7) (2016) 8706–12. 10.1016/j.ceramint.2016.02.105.

[80] A. Zhuang,, R. Liao,, S.C. Dixon,, Y. Lu,, S. Sathasivam,, I.P. Parkin,, C.J. Carmalt, RSC Adv. 7(47) (2017) 29275–83. 10.1039/c7ra04116k.

[81] A. Zhuang,, R. Liao,, Y. Lu,, S.C. Dixon,, A. Jiamprasertboon,, F. Chen,, S. Sathasivam,, I.P. Parkin,, C.J. Carmalt, ACS Appl. Mater. Interfaces 9(48) (2017) 42327–35. 10.1021/acsami.7b13182.

[82] H. Liu,, J. Huang,, Z. Chen,, G. Chen,, K.Q. Zhang,, S.S. Al-Deyab,, Y. Lai, Chem. Eng. J. 330 (2017) 26–35. 10.1016/j.cej.2017.07.114.

[83] K. Feng,, G.Y. Hung,, J. Liu,, M. Li,, C. Zhou,, M. Liu, Chem. Eng. J. 331 (2018) 744–54. 10.1016/j.cej.2017.09.023.

[84] H. Ogihara,, J. Xie,, J. Okagaki,, T. Saji, (2012). 10.1021/la204492q.

[85] Y. Li,, X. Men,, X. Zhu,, B. Ge,, F. Chu,, Z. Zhang, J. Mater. Sci. 51(5) (2016) 2411–9. 10.1007/s10853-015-9552-5.

[86] Y. Qing,, C. Yang,, N. Yu,, Y. Shang,, Y. Sun,, L. Wang,, C. Liu, Chem. Eng. J. 290 (2016) 37–44. 10.1016/j.cej.2016.01.013.

[87] H. Wang,, Z. Liu,, E. Wang,, R. Yuan,, D. Gao,, X. Zhang,, Y. Zhu, Appl. Surf. Sci. 332 (2015) 518–24. 10.1016/j.apsusc.2015.01.213.

[88] J. Tang,, J. Sisler,, N. Grishkewich,, K.C. Tam, J. Colloid Interface Sci. 494 (2017) 397–409. 10.1016/j.jcis.2017.01.077.

[89] E.O. Ogunsona,, P. Panchal,, T.H. Mekonnen, Compos. Sci. Technol. 184 (2019) 107884. 10.1016/j.compscitech.2019.107884.

[90] Z. Hu,, R.M. Berry,, R. Pelton,, E.D. Cranston, ACS Sustain. Chem. Eng. 5(6) (2017) 5018–26. 10.1021/acssuschemeng.7b00415.

[91] A. Salam,, L.A. Lucia,, H. Jameel, Cellulose 22(1) (2015) 397–406. 10.1007/s10570-014-0507-9.

[92] Q.-Y. Cheng,, C.-S. Guan,, M. Wang,, Y.-D. Li,, J.-B. Zeng, Carbohydr. Polym. 199 (2018) 390–6. 10.1016/J.CARBPOL.2018.07.046.

[93] J. Huang,, S. Lyu,, Z. Chen,, S. Wang,, F. Fu, J. Colloid Interface Sci. 536 (2019) 349–62. 10.1016/J.JCIS.2018.10.045.

[94] J. Guo,, W. Fang,, A. Welle,, W. Feng,, I. Filpponen,, O.J. Rojas,, P.A. Levkin, (2016). 10.1021/acsami.6b11741.

[95] H. Mertaniemi,, A. Laukkanen,, J.E. Teirfolk,, O. Ikkala,, R.H.A. Ras, RSC Adv. 2(7) (2012) 2882–6. 10.1039/c2ra00020b.

[96] G. Hayase,, K. Kanamori,, K. Abe,, H. Yano,, A. Maeno,, H. Kaji,, K. Nakanishi, ACS Appl. Mater. Interfaces 6(12) (2014) 9466–71. 10.1021/am501822y.

[97] J. Huang,, S. Wang,, S. Lyu,, F. Fu, Ind. Crops Prod. 122 (2018) 438–47. 10.1016/j.indcrop.2018.06.015.

[98] J. Huang,, S. Wang,, S. Lyu,, J. Huang,, S. Wang,, S. Lyu, Materials (Basel). 10(9) (2017) 1080. 10.3390/ma10091080.

[99] Z. Zhu,, S. Fu,, L.A. Lucia, ACS Sustain. Chem. Eng. 7(5) (2019) 5376–84. 10.1021/acssuschemeng.8b06399.

[100] P. Khanjani,, A.W.T. King,, G.J. Partl,, L.-S. Johansson,, M.A. Kostiainen,, R.H.A. Ras, (2018). 10.1021/acsami.7b19310.

[101] J. Huang,, S. Lyu,, F. Fu,, Y. Wu,, S. Wang, RSC Adv. 7(33) (2017) 20152–9. 10.1039/C6RA27663F.

[102] W. Shang,, J. Huang,, H. Luo,, P.R. Chang,, J. Feng,, G. Xie, Cellulose 20(1) (2013) 179–90. 10.1007/s10570-012-9795-0.

[103] B. Poaty,, V. Vardanyan,, L. Wilczak,, G. Chauve,, B. Riedl, Prog. Org. Coatings 77(4) (2014) 813–20. 10.1016/j.porgcoat.2014.01.009.

[104] C. Reverdy,, N. Belgacem,, M.S. Moghaddam,, M. Sundin,, A. Swerin,, J. Bras, Colloids Surfaces A Physicochem. Eng. Asp. 544 (2018) 152–8. 10.1016/j.colsurfa.2017.12.059.

[105] T. Arbatan,, L. Zhang,, X.Y. Fang,, W. Shen, Chem. Eng. J. 210 (2012) 74–9. 10.1016/j.cej.2012.08.074.

[106] M. Ly,, T. Mekonnen, J. Ind. Eng. Chem. (2019). 10.1016/j.jiec.2019.12.014.

[107] G. Barati Darband,, M. Aliofkhazraei,, S. Khorsand,, S. Sokhanvar,, A. Kaboli, Arab. J. Chem. 13(1) (2020) 1763–802. 10.1016/j.arabjc.2018.01.013.

[108] T. Liu,, S. Chen,, S. Cheng,, J. Tian,, X. Chang,, Y. Yin, Electrochim. Acta 52(28) (2007) 8003–7. 10.1016/j.electacta.2007.06.072.

[109] J.M. McIntyre,, H.Q. Pham, Prog. Org. Coatings 27(1–4) (1996) 201–7. 10.1016/0300-9440(95)00532-3.

[110] S. Liu,, L. Gu,, H. Zhao,, J. Chen,, H. Yu, J. Mater. Sci. Technol. 32(5) (2016) 425–31. 10.1016/J.JMST.2015.12.017.

[111] R. Cardeña,, B. Cercado,, G. Buitrón, Biohydrogen, Elsevier, 2019, pp. 159–85.

[112] M. Heidarian,, M.R. Shishesaz,, S.M. Kassiriha,, M. Nematollahi, Prog. Org. Coatings 68(3) (2010) 180–8. 10.1016/j.porgcoat.2010.02.006.

[113] L. Ejenstam,, L. Ovaskainen,, I. Rodriguez-Meizoso,, L. Wågberg,, J. Pan,, A. Swerin,, P.M. Claesson, J. Colloid Interface Sci. 412 (2013) 56–64. 10.1016/j.jcis.2013.09.006.

[114] M. Behzadnasab,, S.M. Mirabedini,, K. Kabiri,, S. Jamali, Corros. Sci. 53(1) (2011) 89–98. 10.1016/J.CORSCI.2010.09.026.

[115] H. Leidheiser, CORROSION 38(7) (1982) 374–83. 10.5006/1.3581899.

[116] C.-H. Chang,, T.-C. Huang,, C.-W. Peng,, T.-C. Yeh,, H.-I. Lu,, W.-I. Hung,, C.-J. Weng,, T.-I. Yang,, J.-M. Yeh, Carbon N. Y. 50 (2012) 5044–51. 10.1016/j.carbon.2012.06.043.

[117] H. Zhang,, J. Wang,, X. Liu,, Z. Wang,, S. Wang, Ind. Eng. Chem. Res. 52(30) (2013) 10172–80. 10.1021/ie400666a.

[118] J.-M. Yeh,, S.-J. Liou,, C.-Y. Lin,, C.-Y. Cheng,, Y.-W. Chang,, K.-R. Lee, Chem. Mater. 14(1) (2002) 154–61. 10.1021/cm010337f.

[119] D. Dutta,, A.N.F. Ganda,, J.-K. Chih,, C.-C. Huang,, C.-J. Tseng,, C.-Y. Su, Nanoscale 10(26) (2018) 12612–24. 10.1039/C8NR03261K.

[120] Y.W. Chen-Yang,, H.C. Yang,, G.J. Li,, Y.K. Li, J. Polym. Res. 11(4) (2005) 275–83. 10.1007/s10965-005-3982-8.

[121] M.F. Montemor, Surf. Coatings Technol. 258 (2014) 17–37. 10.1016/j.surfcoat.2014.06.031.

[122] H. Nazari,, X. Shi, Industrial Applications for Intelligent Polymers and Coatings, Springer International Publishing, Cham, 2016.

[123] R.J. Moon,, A. Martini,, J. Nairn,, J. Simonsen,, J. Youngblood, Chem. Soc. Rev. 40(7) (2011) 3941. 10.1039/c0cs00108b.

[124] Z. Zhang, Surface Modification of Cellulose Nanocrystal for Advanced Applications. University of Waterloo, 2017.

[125] A. Dufresne, Mater. Today 16(6) (2013) 220–7. 10.1016/j.mattod.2013.06.004.

[126] T.H. Mekonnen,, T. Ah-Leung,, S. Hojabr,, R. Berry, Colloids Surfaces A Physicochem. Eng. Asp. 583 (2019) 123949. 10.1016/j.colsurfa.2019.123949.

[127] D. Klemm,, E.D. Cranston,, D. Fischer,, M. Gama,, S.A. Kedzior,, D. Kralisch,, F. Kramer,, T. Kondo,, T. Lindström,, S. Nietzsche,, K. Petzold-Welcke,, F. Rauchfuß, Mater. Today 21(7) (2018) 720–48. 10.1016/j.mattod.2018.02.001.

[128] J. Tang,, J. Sisler,, N. Grishkewich,, K.C. Tam, J. Colloid Interface Sci. 494 (2017) 397–409. 10.1016/j.jcis.2017.01.077.

[129] P. Panchal,, T.H. Mekonnen, Nanoscale Adv. 1(7) (2019). 10.1039/c9na00265k.

[130] S. Eyley,, W. Thielemans, Nanoscale 6(14) (2014) 7764–79. 10.1039/C4NR01756K.

[131] K.H.M. Kan,, J. Li,, K. Wijesekera,, E.D. Cranston, Biomacromolecules 14(9) (2013) 3130–9. 10.1021/bm400752k.

[132] J. Arredondo,, P.G. Jessop,, P. Champagne,, J. Bouchard,, M.F. Cunningham, Green Chem. 19(17) (2017) 4141–52. 10.1039/C7GC01798G.

[133] D. Wu,, W. Li,, Y. Zhao,, Y. Deng,, H. Zhang,, H. Zhang,, L. Dong, Chinese J. Polym. Sci. 33(3) (2015) 444–55. 10.1007/s10118-015-1597-z.

[134] F. Sun,, W. Liu,, Z. Dong,, Y. Deng, Chem. Eng. J. 330 (2017) 774–82. 10.1016/j.cej.2017.07.142.

[135] Y. Habibi,, L.A. Lucia,, O.J. Rojas, Chem. Rev. 110(6) (2010) 3479–500. 10.1021/cr900339w.

[136] A. Kaboorani,, B. Riedl, Ind. Crops Prod. 65 (2015) 45–55. 10.1016/j.indcrop.2014.11.027.

[137] B.L. Tardy,, S. Yokota,, M. Ago,, W. Xiang,, T. Kondo,, R. Bordes,, O.J. Rojas, Curr. Opin. Colloid Interface Sci. 29 (2017) 57–67. 10.1016/j.cocis.2017.02.004.

[138] T. Saito,, Y. Nishiyama,, J.-L. Putaux,, M. Vignon,, A. Isogai, Biomacromolecules 7(6) (2006) 1687–91. 10.1021/bm060154s.

[139] D. Li,, M.B. Müller,, S. Gilje,, R.B. Kaner,, G.G. Wallace, Nat. Nanotechnol. 3(2) (2008) 101–5. 10.1038/nnano.2007.451.

[140] K. Xhanari,, K. Syverud,, G. Chinga-Carrasco,, K. Paso,, P. Stenius, Cellulose 18(2) (2011) 257–70. 10.1007/s10570-010-9482-y.

[141] M. Kaushik,, C. Fraschini,, G. Chauve,, J.-L. Putaux,, A. Moores, The Transmission Electron Microscope - Theory and Applications, InTech, 2015, p. .

[142] L. Chen,, Q. Wang,, K. Hirth,, C. Baez,, U.P. Agarwal,, J.Y. Zhu, Cellulose 22(3) (2015) 1753–62. 10.1007/s10570-015-0615-1.

[143] B.M. Trinh,, T. Mekonnen, Polymer (Guildf). 155 (2018) 64–74. 10.1016/j.polymer.2018.08.076.

[144] S. Huang,, L. Zhou,, M.-C. Li,, Q. Wu,, D. Zhou, Materials (Basel). 10(1) (2017) 80. 10.3390/ma10010080.

[145] A. Kumar,, Y.S. Negi,, V. Choudhary,, N.K. Bhardwaj, J. Mater. Phys. Chem. 2(1) (2014) 1–8. 10.12691/JMPC-2-1-1.

[146] Z. Tang,, W. Li,, X. Lin,, H. Xiao,, Q. Miao,, L. Huang,, L. Chen,, H. Wu,, Z. Tang,, W. Li,, X. Lin,, H. Xiao,, Q. Miao,, L. Huang,, L. Chen,, H. Wu, Polymers (Basel). 9(12) (2017) 421. 10.3390/polym9090421.

[147] M. Salajková,, L.A. Berglund,, Q. Zhou, J. Mater. Chem. 22(37) (2012) 19798. 10.1039/c2jm34355j.

[148] N. Lin,, C. Bruzzese,, A. Dufresne, ACS Appl. Mater. Interfaces 4(9) (2012) 4948–59. 10.1021/am301325r.

[149] R.K. Johnson,, A. Zink-Sharp,, W.G. Glasser,, S.H. Renneckar,, C.E. Frazier,, A.R. Esker,, M. Roman, TEMPO-OXIDIZED NANOCELLULOSES: SURFACE MODIFICATION AND USE AS ADDITIVES IN CELLULOSIC NANOCOMPOSITES, 2010.

[150] W. Wang,, Q. Bai,, T. Liang,, H. Bai,, X. Liu, Polymers (Basel). 9(12) (2017) 455. 10.3390/polym9090455.

[151] M.-C. Li,, Q. Wu,, K. Song,, S. Lee,, Y. Qing,, Y. Wu, ACS Sustain. Chem. Eng. 3(5) (2015) 821–32. 10.1021/acssuschemeng.5b00144.

[152] Y. Su,, C. Burger,, H. Ma,, B. Chu,, B.S. Hsiao, Biomacromolecules 16(4) (2015) 1201–9. 10.1021/bm501897z.

[153] A.C. O'sullivan, Cellulose 4 (1997) 173–207. 10.1023/A:1018431705579.

[154] F. Boissou,, A. Mühlbauer,, K. De Oliveira Vigier,, L. Leclercq,, W. Kunz,, S. Marinkovic,, B. Estrine,, V. Nardello-Rataj,, F. Jérôme, Green Chem 16 (2014) 2463. 10.1039/c3gc42396d.

[155] L. Kumari,, W.Z. Li,, S. Kulkarni,, K.H. Wu,, W. Chen,, C. Wang,, C.H. Vannoy,, R.M. Leblanc, Nanoscale Res. Lett. 5(1) (2010) 149–57. 10.1007/s11671-009-9457-9.

[156] G. Sui,, Y. Zhao,, Q. Zhang,, Q. Fu, RSC Adv. 6(60) (2016) 54785–92. 10.1039/C6RA11451B.

[157] S. Chaudhary,, D. Rohilla,, S.K. Mehta, Mater. Res. Express 1 (2014) 15011. 10.1088/2053-1591/1/1/015011.

[158] F. Hoeng,, A. Denneulin,, C. Neuman,, J. Bras, J. Nanoparticle Res. 17(6) (2015) 244. 10.1007/s11051-015-3044-z.

[159] Riddick,, T.M. (Thomas Moore), Control of colloid stability through zeta potential : with a closing chapter on its relationship to cardiovascular disease, Zeta-Meter, Inc., by Livingston Pub. Co, Wynnewood, Pa, 1968.

[160] R.J. Hunter, Zeta Potential in Colloid Science, Elsevier, London ; Toronto; London ; Toronto : Academic Press, 1981, 1981.

[161] D. Cheng,, Y. Wen,, X. An,, X. Zhu,, X. Cheng,, L. Zheng,, J.E. Nasrallah, J. Bioresour. Bioprod. 1(3) (2016) 114–9. 10.21967/jbb.v1i3.6.

[162] S.P. Akhlaghi,, M. Zaman,, N. Mohammed,, C. Brinatti,, R. Batmaz,, R. Berry,, W. Loh,, K.C. Tam, Carbohydr. Res. 409 (2015) 48–55. 10.1016/j.carres.2015.03.009.

[163] Letchford,, Jackson,, B. Wasserman,, Ye,, W. Hamad,, H. Burt, Int. J. Nanomedicine 6 (2011) 321. 10.2147/IJN.S16749.

[164] S. Pourhashem,, M.R. Vaezi,, A. Rashidi,, M. Reza Bagherzadeh, Eval. Program Plann. 115 (2017) 78–92. 10.1016/j.corsci.2016.11.008.

[165] L. Yue,, A. Maiorana,, F. Khelifa,, A. Patel,, J.M. Raquez,, L. Bonnaud,, R. Gross,, P. Dubois,, I. Manas-Zloczower, Polymer (Guildf). 134 (2018) 155–62. 10.1016/j.polymer.2017.11.051.

[166] B. Tan,, N.L. Thomas, J. Memb. Sci. 514 (2016) 595–612. 10.1016/j.memsci.2016.05.026.

[167] T.T.X. Hang,, N.T. Dung,, T.A. Truc,, N.T. Duong,, B. Van Truoc,, P.G. Vu,, T. Hoang,, D.T.M. Thanh,, M.-G. Olivier, Prog. Org. Coatings 79 (2015) 68–74. 10.1016/j.porgcoat.2014.11.008.

[168] B. Pilch-Pitera,, D. Czachor,, K. Kowalczyk,, E. Pavlova,, J. Wojturski,, Ł. Florczak,, Ł. Byczyński, Prog. Org. Coatings 137(March) (2019). 10.1016/j.porgcoat.2019.105367.

[169] Z. Yu,, H. Di,, Y. Ma,, Y. He,, L. Liang,, L. Lv,, X. Ran,, Y. Pan,, Z. Luo, Surf. Coatings Technol. 276 (2015) 471–8. 10.1016/j.surfcoat.2015.06.027.

[170] G.X. Shen,, Y.C. Chen,, C.J. Lin, Thin Solid Films 489(1–2) (2005) 130–6. 10.1016/j.tsf.2005.05.016.

[171] R. Zandi-zand,, A. Ershad-langroudi,, A. Rahimi, Prog. Org. Coatings 53(4) (2005) 286–91. 10.1016/j.porgcoat.2005.03.009.

[172] X. Chen,, J. Yuan,, J. Huang,, K. Ren,, Y. Liu,, S. Lu,, H. Li, Appl. Surf. Sci. 311 (2014) 864–9. 10.1016/j.apsusc.2014.05.186.

[173] M.M. De Souza Lima,, R. Borsali, Macromol. Rapid Commun. 25(7) (2004) 771–87. 10.1002/marc.200300268.

[174] N. Dhar,, D. Au,, R.C. Berry,, K.C. Tam, Colloids Surfaces A Physicochem. Eng. Asp. 415 (2012) 310–9. 10.1016/j.colsurfa.2012.09.010.

[175] A. Pei,, J.-M. Malho,, J. Ruokolainen,, Q. Zhou,, L.A. Berglund, Macromolecules 44(11) (2011) 4422–7. 10.1021/ma200318k.

[176] S.P. Akhlaghi,, R.C. Berry,, K.C. Tam, Cellulose 20(4) (2013) 1747–64. 10.1007/s10570-013-9954-y.

[177] S. Xu,, N. Girouard,, G. Schueneman,, M.L. Shofner,, J.C. Meredith, Polymer (Guildf). 54(24) (2013) 6589–98. 10.1016/J.POLYMER.2013.10.011.

[178] R.M. Sheltami,, H. Kargarzadeh,, I. Abdullah, Sains Malaysiana 44(6) (2015) 801–10. 10.17576/jsm-2015-4406-05.

[179] B. Ly,, M.N. Belgacem,, J. Bras,, M.C. Brochier Salon, Mater. Sci. Eng. C 30(3) (2010)

343–7. 10.1016/j.msec.2009.11.009.

[180] E.P. Plueddemann, Silane Coupling Agents, Springer US, Boston, MA, 1991.

[181] T. Child,, W. van Ooij, Trans. IMF 77(2) (1999) 64–70. 10.1080/00202967.1999.11871249.

[182] H. Khanjanzadeh,, R. Behrooz,, N. Bahramifar,, W. Gindl-Altmutter,, M. Bacher,, M. Edler,, T. Griesser, Int. J. Biol. Macromol. 106 (2018) 1288–96. 10.1016/j.ijbiomac.2017.08.136.

[183] M. Abdelmouleh,, S. Boufi,, M.N. Belgacem,, A. Dufresne,, A. Gandini, J. Appl. Polym. Sci. 98(3) (2005) 974–84. 10.1002/app.22133.

[184] S.C. Chowdhury,, J.W. Gillespie, J. Mater. Sci. 52(22) (2017) 12981–98. 10.1007/s10853-017-1412-z.

[185] C. Wang,, H. Mao,, C. Wang,, S. Fu, Ind. Eng. Chem. Res 50 (2011) 11930–4. 10.1021/ie200887x.

[186] M.-J. Oh,, S.-Y. Lee,, K.-H. Paik, J. Ind. Eng. Chem. 17 (2011) 149–53. 10.1016/j.jiec.2010.12.014.

[187] H. Khanjanzadeh,, R. Behrooz,, N. Bahramifar,, W. Gindl-Altmutter,, M. Bacher,, M. Edler,, T. Griesser, Int. J. Biol. Macromol. 106 (2018) 1288–96. 10.1016/J.IJBIOMAC.2017.08.136.

[188] J. Lin,, J.A. Siddiqui,, R.M. Ottenbrite, Polym. Adv. Technol. 12(5) (2001) 285–92. 10.1002/pat.64.

[189] M. Ángel Hidalgo-Salazar,, F. Luna-Vera,, J. Pablo Correa-Aguirre, Characterizations of Some Composite Materials, Vol. i, IntechOpen, 2019, p. 13.

[190] X. Cao,, Y. Habibi,, L.A. Lucia, J. Mater. Chem. 19(38) (2009) 7137. 10.1039/b910517d.

[191] A. Alanis,, J.H. Valdés,, N.V. María Guadalupe,, R. Lopez,, R. Mendoza,, A.P. Mathew,, R. Díaz De León,, L. Valencia, RSC Adv. 9(30) (2019) 17417–24. 10.1039/c9ra02451d.

[192] H. Es-haghi,, S.M. Mirabedini,, M. Imani,, R.R. Farnood, Colloids Surfaces A Physicochem. Eng. Asp. 447 (2014) 71–80. 10.1016/j.colsurfa.2014.01.021.

[193] H. Hettegger,, I. Sumerskii,, S. Sortino,, A. Potthast,, T. Rosenau, ChemSusChem 8(4) (2015) 680–7. 10.1002/cssc.201402991.

[194] K. Chitra,, G. Annadurai, J. Nanotechnol. 2013 (2013). 10.1155/2013/509628.

[195] N.H. Mohd,, N.F.H. Ismail,, J.I. Zahari,, W.F. bt Wan Fathilah,, H. Kargarzadeh,, S. Ramli,, I. Ahmad,, M.A. Yarmo,, R. Othaman, J. Nanomater. 2016 (2016) 1–8. 10.1155/2016/4804271.

[196] J. Dai,, M. Chae,, D. Beyene,, C. Danumah,, F. Tosto,, D. Bressler, Materials (Basel).

11(9) (2018) 1645. 10.3390/ma11091645.

[197] M. Abdelmouleh,, S. Boufi,, M.N. Belgacem,, A.P. Duarte,, A. Ben Salah,, A. Gandini, Int. J. Adhes. Adhes. 24(1) (2004) 43–54. 10.1016/S0143-7496(03)00099-X.

[198] J. Lu,, P. Askeland,, L.T. Drzal, Polymer (Guildf). 49(5) (2008) 1285–96. 10.1016/j.polymer.2008.01.028.

[199] N. Yousefi,, M.M. Gudarzi,, Q. Zheng,, X. Lin,, X. Shen,, J. Jia,, F. Sharif,, J.-K. Kim, (2013). 10.1016/j.compositesa.2013.02.005.

[200] M. Sabzi,, S.M. Mirabedini,, J. Zohuriaan-Mehr,, M. Atai, Prog. Org. Coatings 65(2) (2009) 222–8. 10.1016/j.porgcoat.2008.11.006.

[201] P.C. Ma,, N.A. Siddiqui,, G. Marom,, J.K. Kim, Compos. Part A Appl. Sci. Manuf. 41(10) (2010) 1345–67. 10.1016/j.compositesa.2010.07.003.

[202] J. Li,, P.C. Ma,, W.S. Chow,, C.K. To,, B.Z. Tang,, J.K. Kim, Adv. Funct. Mater. 17(16) (2007) 3207–15. 10.1002/adfm.200700065.

[203] A. Kiziltas,, B. Nazari,, D.J. Gardner,, D.W. Bousfield, Polym. Eng. Sci. 54(4) (2014) 739–46. 10.1002/pen.23603.

[204] B. Shen,, W. Zhai,, M. Tao,, D. Lu,, W. Zheng, Compos. Sci. Technol. 77 (2013) 87–94. 10.1016/j.compscitech.2013.01.014.

[205] N. Salahuddin,, S.A. Abo-El-Enein,, A. Selim,, O. Salah El-Dien, Appl. Clay Sci. 47(3–4) (2010) 242–8. 10.1016/j.clay.2009.10.017.

[206] O. Becker,, R.J. Varley,, G.P. Simon, Eur. Polym. J. 40(1) (2004) 187–95. 10.1016/j.eurpolymj.2003.09.008.

[207] O. ur Rahman,, M. Kashif,, S. Ahmad, Prog. Org. Coatings 80 (2015) 77–86. 10.1016/J.PORGCOAT.2014.11.023.

[208] T.I. Kadurina,, V.A. Prokopenko,, S.I. Omelchenko, Polymer (Guildf). 33(18) (1992) 3858–64. 10.1016/0032-3861(92)90373-5.

[209] H.E. Jamil,, A. Shriri,, R. Boulif,, M.F. Montemor,, M.G.S. Ferreira, Cem. Concr. Compos. 27(6) (2005) 671–8. 10.1016/j.cemconcomp.2004.09.019.

[210] D. Yu,, J. Tian,, J. Dai,, X. Wang, Electrochim. Acta (2013) 409–19. 10.1016/j.electacta.2013.03.071.

[211] Y. Zhu,, J. Xiong,, Y. Tang,, Y. Zuo, Prog. Org. Coatings 69(1) (2010) 7–11. 10.1016/j.porgcoat.2010.04.017.